Project no. TIP5-CT-2006-031415O

# INNOTRACK

Integrated Project (IP)

Thematic Priority 6: Sustainable Development, Global Change and Ecosystems

# D4.3.5
# Simulation of material deformation and RCF

Due date of deliverable: 2009-05-31

Actual submission date: 2009-11-27

Start date of project: 1 September 2006 Duration: 36 months

Organisation name of lead contractor for this deliverable: Chalmers

Revision: Final

| **Project co-funded by the European Commission within the Sixth Framework Programme (2002-2006)** | | |
|---|---|---|
| **Dissemination Level** | | |
| **PU** | Public | PU |
| **PP** | Restricted to other programme participants (including the Commission Services) | |
| **RE** | Restricted to a group specified by the consortium (including the Commission Services) | |
| **CO** | Confidential, only for members of the consortium (including the Commission Services) | |

# Table of Contents

**Glossary** .......... 4

**1. Executive Summary** .......... 5

**2. Introduction** .......... 6

**3. Evaluated test cases** .......... 8

3.1 Twin disc tests .......... 8
3.2 VAS – Full scale tests .......... 8
3.3 DB – Full scale tests .......... 9
*Measured test conditions* .......... *9*
*Presumed test conditions* .......... *9*

**4. A note on the evaluation of fatigue criteria** .......... 10

4.1 Background .......... 10
4.2 Fatigue life prediction criteria .......... 10

**5. Engineering criteria for RCF life prediction** .......... 11

5.1 Peak elastic shear stress magnitude .......... 11
5.2 The shakedown diagram and the fatigue index $FI_{\text{surf}}$ .......... 11

**6. Evaluation of tests using engineering RCF criteria** .......... 14

6.1 Approach .......... 14
6.2 Evaluation of twin-disc tests .......... 15
*6.2.1 Peak elastic shear stress* .......... *15*
*6.2.2 Fatigue index* $FI_{surf}$ .......... *15*
6.3 Evaluation of voestalpine full scale tests .......... 15
*6.3.1 Peak elastic shear stress* .......... *15*
*6.3.2 Fatigue index* $FI_{surf}$ .......... *16*
6.4 Evaluation of DB — full-scale tests .......... 19
*6.4.1 Peak elastic shear stress* .......... *19*
*6.4.2 Fatigue index* $FI_{surf}$ .......... *19*
6.5 Summary of RCF life predictions using engineering criteria .......... 20

**7. Finite element simulations of material deterioration** .......... 23

7.1 Finite element models .......... 23
*7.1.1 Finite element model of the voestalpine test rig* .......... *23*
*7.1.2 Finite element model of the DB test stand C* .......... *25*
7.2 Constitutive model for the rail steel .......... 27
7.3 Results from FE-simulations of plastic deformation of the rail .......... 29
*7.3.1 Results from the voestalpine test stand* .......... *30*
*7.3.2 Results from the DB test stand C* .......... *31*

**8. Rolling contact fatigue analysis** .......... 34

8.1 Low cycle fatigue analysis .......... 34
8.2 Ratcheting analysis .......... 37

**9. Concluding remarks** .......... 39

9.1 RCF prediction using engineering models .......... 39
9.2 Finite element simulations .......... 40
9.3 Recommendations .......... 41
*9.3.1 Engineering model* .......... *41*
*9.3.2 RCF life predictions based on FE-simulations* .......... *41*

*9.3.3 Final conclusions ........ 42*

**10. References ........ 43**

**11. Appendix I Results from FE simulations of the voestalpine test rig ........ 44**

11.1 Animations ........ 44
11.2 Contour plots ........ 44
11.3 Evolution of the von Mises effective stress ........ 44
11.4 Evolution of the contact pressure ........ 49
11.5 Evolution of the vertical stress component ........ 54
11.6 Evolution of equivalent plastic strain ........ 59

**12. Appendix II Results from FE simulations of the DB test rig C with no lateral load ........ 64**

12.1 Animations ........ 64
12.2 Contour plots ........ 64
12.3 Evolution of the von Mises effective stress ........ 64
12.4 Evolution of the contact pressure ........ 69
12.5 Evolution of equivalent plastic strain ........ 75

# Glossary

| | |
|---|---|
| WP | Work Package |
| Chalmers | Chalmers University of Technology |
| CPU | Central Processing Unit |
| DB | Deutsche Bahn Technik/Beschaffung |
| FE | Finite element |
| KMS | Knowledge Managemement System |
| LCF | Low Cycle Fatigue |
| RCF | Rolling Contact Fatigue |
| SUROS Machine | Sheffield University ROlling Sliding [Twin-Disc Machine] |
| TUD | Technical University Delft |
| UoN | University of Newcastle |
| VAS | voestalpine Schienen GmbH |

# 1. Executive Summary

Testing of rail steels has a long tradition in the railway industry both in the form of full-scale and scaled tests. However test results from different test stands have largely been self-standing, which have made quantitative comparison between different test rigs and towards operational scenarios difficult.

The main purpose of this deliverable is to investigate the possibility of bridging this gap by numerical simulation aimed at predicting rolling contact fatigue (RCF) initiation. Two modelling approaches are employed: Methods that aim at relating the evaluated contact stress distribution directly to the RCF initiation life are denoted “engineering approaches”. In contrast “finite element (FE) based approaches” evaluate the (elasto-plastic) material response owing to the acting contact stresses and relates the fatigue life to the resulting stresses/strains in the material.

To obtain reliable RCF life predictions is found to currently be on the brink of what is possible. The report takes the approaches outlined above as far as possible and reports intermediate results, complications etc.

In the report prediction based on engineering approaches sets out from previously derived contact stress distributions [5]. These are complemented by simulations of dynamic wheel–rail interaction in order to evaluate possible additional longitudinal tractive stresses due to the rolling on the wheel on the rail. For the case studied, these were found to be comparable to the lateral tractive stresses. It should here be noted that an evaluation of wheel–rail dynamics based on Hertzian contact theory is not sufficient for high-resolution evaluation of the contact stress distribution for the case studied. Further such an analysis is extremely sensitive to the geometry of the contacting surfaces.

Supported by these simulations it was presumed that the contact conditions corresponded to full slip for all the three test rigs simulated. Based on this a shakedown map based fatigue index was evaluated and a plot of the fatigue index versus the fatigue life in a log-log diagram was shown to give a reasonable match to a straight line, which would indicate a Wöhler-like fatigue life relationship. If this relationship holds for further scrutinization it would be a major step forward for fatigue life prediction and comparisons between test rigs and towards operational scenarios. However the current analysis contains major uncertainties most notably in estimated wheel–rail friction.

The FE based approaches sets out by calibrating an elasto-plastic material model of the rail steel towards experimental stress–strain data. FE-models of the two full-scale test rigs are then developed and load cycles featuring the loaded wheel rolling over an representative rail section are carried out. The stress–strain response in highly loaded material points on the rail surface are then evaluated and quantified. Methods to predict resulting fatigue life are then described both based on the presumption that the dominating fatigue mechanism is low-cycle-fatigue (in the sense that fatigue life is governed by the strain range) or ratcheting (in the sense that fatigue life is governed by accumulated plastic strain).

The simulations highlighted the fact that the studied combination of very local high deformations, large displacements, high contact pressures and interfacial shear stresses, conformal contact and need for sophisticated constitutive models is currently extremely cumbersome to simulate. Reliable results for one test rig for two load conditions have been obtained after tedious work of tuning analysis parameters. These results show a high sensitivity also for rather low variations in applied lateral load magnitudes. Further the results show that plastic deformations in the FE-simulations introduce a level of “smoothing”, which levels out very high stress concentrations. On the other hand this also makes a priori identifications of critical material points difficult. The results finally show that the use of non-linear hardening seems crucial and that the proposed methods of fatigue assessment seem credible.

In addition simulations of the second rig stumbled upon a bug in the commercial code, which resulted in an erroneous evaluation of the contact stresses. Although this rendered these results useless it highlighted the sensitivity and complexity of the problem at hand. Measures are currently taken to find a work-around for the identified bug.

In summary, the current report is in our opinion a major step forward in comparing different bench tests to each other and to operational conditions by numerical simulation. Based on the results this should indeed be feasible although very complicated. However the main benefit of the report lies perhaps in the identification of the limitations of today’s top-notch approaches and simulation toolboxes.

Finally a word of caution is needed: As the simulations here and in [5] clearly show, the problem at hand is inherently sensitive. Consequently the accuracy of predictions (be it numerical, empirical, experimentally-based etc) will always be limited.

# 2. Introduction

The aim of this study is to compare the outcome of different numerical RCF predictive models towards test results. In addition the numerical simulations will make it possible to compare different test scenarios towards each other and eventually towards operational conditions. It should here be noted that we are only concerned with surface initiated RCF, and only with crack initiation life, not longer crack propagation behaviour.

In general surface initiated RCF depends on a number of inter-dependent parameters. The main driving mechanism is the interfacial wheel–rail shear. It is generally considered that surface initiated RCF is related to the (uni-directional) accumulation of plastic strains, e.g. ratcheting, which is a special kind of low-cycle-fatigue (LCF). In general, the state of stress and strain in rolling contact is multiaxial with non-proportional components, which calls for special care in fatigue predictions. If the interfacial shear is acting in both directions with (more or less) equal magnitudes, a case of more traditional LCF (where fatigue life is related to the stress range) would be obtained. Here also the relation between stick and slip is important since a high proportion of slip will shift the deterioration towards mainly wear[1]. In this context also the contact pressure is important partly because a higher contact pressure will allow a higher interfacial friction before slip (and thus wear) dominates. Wheel and rail geometries, and in particular their interaction, are of main importance since a (local) mismatch can give very high (local) stress concentrations both in the normal and shear stresses. Conformal contact (i.e. a good profile match) has the benefit of distributing the pressure and thus decreasing pressure levels. However it creates a high sensitivity to profile mismatch: a small lateral displacement of one profile will cause very high stress concentrations. Further, it may decrease the steering ability of the train, which induces high additional shear stresses to allow for the steering. Finally there are a number of parameters that are of importance, but whose effects are very hard to include in more general modelling. These factors include residual stresses, material microstructure and anisotropy. Regarding the loading the analyses are normally so demanding that a quasi-static loading is presumed. Dynamic load factors are then (usually) included in the applied load. This would correspond to fixed load magnitude during a material point's passage through the contact patch.

Two modelling approaches are employed: Methods that aim at relating the evaluated contact stress distribution directly to the RCF initiation life are denoted "engineering approaches". In contrast "finite element (FE) based approaches" evaluate the (elasto-plastic) material response owing to the acting contact stresses and relates the fatigue life to the resulting stresses/strains in the material.

There are several practical complications in predicting RCF initiation for the tests. Some of these complications are:

- Coefficient of friction in the wheel–rail interface is not evaluated for the full-scale tests and thus has to be guessed based on tests where it has been measured.
- The relative lateral position between wheel and rail are not evaluated in the full-scale tests. In the current study the positions evaluated in reference [6] have been adopted if nothing else is stated.
- The contacting profiles evolve throughout the tests. Measured profiles have been adopted, but some averaging is needed for practical purposes. It should however be noted that the elastic-plastic simulations decreases the influence of the local contact geometry.
- Water (or other forms of lubrication) is necessary to make initiated cracks grow in the tests. This influence is only possible to model by considering fluid penetration in the initiated cracks and pressurization or internal lubrication of the cracks at subsequent loading. It is not possible to go in to such detail in the current study since this is a major research area in itself. Instead we focus on the identification of test conditions that cause crack initiation, rather than propagation.
- The tests in the DB test rig does not feature constant loading conditions. Due to the extensive computational demands this requires an approach where RCF prediction is based on some selected load conditions that are evaluated.

---

[1] Interestingly, this is to an extent in conflict with the usual approximation in numerical prediction of surface initiated RCF that a condition of full slip exists.

The report first outlines the test conditions at the three tests considered. This is followed by an introduction to the characteristics of fatigue prediction criteria and how the predictions can be evaluated towards experimentally found fatigue lives.

After this introduction two engineering models are employed. It is found that there is a need to complement the input data with some preliminary simulations of dynamic wheel–rail interaction. The results of these are presented and discussed. The engineering criteria are evaluated towards test rig experiments and the results discussed.

To capture the material deformation in detail, FE-simulations are carried out. Methods for fatigue prediction post processing using LCF (in the sense that fatigue life is governed by the strain range) and/or ratcheting (in the sense that fatigue life is governed by accumulated plastic strain) criteria are outlined and demonstrated for the LCF-based criterion. FE-models and results are discussed.

Finally obtained results are discussed along with challenges and complications discovered. Procedures for operationally feasible fatigue life predictions are outlined along with the hurdles that need to be overcome for operational implementations.

# 3. Evaluated test cases

Test cases within the work package 4.3 of INNOTRACK so far are described in report D4.3.1 – “Initial definition of conditions for testing matrix of rail steels and welds” [1] and in report D4.3.3 – “Results of first test rig measurements” [2]. For details on evaluating contact stresses, please consult references [5, 6 and 7].

## 3.1 Twin disc tests

The tests were carried out by University of Newcastle using the SUROS twin-disc machine in Sheffield, UK.

The tests consisted of 5000 dry cycles followed by 5000 wet cycles.

Wear was detected during both phases, multiple cracks detected by 4000 wet cycles, i.e. at 9000 total cycles

- Wheel steel R7
- Rail steel Corus 400
- Line contact between two cylindrical discs
    - Diameter 47 mm
    - Width 10 mm (running band)
- Maximum Hertzian contact pressure $p_0$ = 1500 MPa
- Coefficient of friction
    - Initial dry phase $\mu \approx 0.4$ to 0.45
    - Subsequent lubricated phase $\mu \approx 0.15$ to 0.2
    - Full slip is presumed.

## 3.2 VAS – Full scale tests

The tests were carried out by voestalpine in the VAS test rig in Leoben, Austria.

The test consisted of 100,000 passes with intermediate water supply every 10 passes.

RCF in the form of head checks at a location 3 – 11 mm from the gauge corner of the rail was detected after 20 000 – 50 000 passes

### Measured test conditions (adopted from [6])

- Wheel steel R7
- Rail steel R260
- Angle of attack $\Psi = 0$
- Vertical load $F_y = -196$ kN (20t)
- Lateral load $F_x = 39.2$ kN (4t)
- Longitudinal load $F_z = 0$
- Lubrication: Water applied every 10 passes
- Wheel diameter = 920 mm
- Profiles as measured at 20,000 passes

### Presumed test conditions

Presumptions based on the analyses in [6]

- Young’s modulus $E = 210$ GPa
- Poisson’s ration $\nu = 0.28$
- Rail inclination = 0

- Relative lateral position between wheel and rail, $\Delta Y = 9.9$ mm
- $\mu = 0.4$–$0.45$

## 3.3 DB – Full scale tests

The tests were carried out by DB in the test rig in Kirchmöser, Germany.

The test consisted of 1.2 million load cycles with constant water supply.

In this test no head checks were found, but embryonic cracks were later revealed in microscopy investigations.

### Measured test conditions

- Wheel steel R7
- Rail steel R260
- Angle of attack $\Psi = 0.25°$
- Vertical load $F_y = -147$ kN (15t)
  (The load was increased after 1 million cycles, see [2]).
- Applied lateral load $F_x = 5$ to 15 kN
  (Alternated sinusoidally in a direction off the gauge corner with a frequency of 0.5 Hz)
- Longitudinal load $F_z = 0$
- Lubrication: Water constantly applied
- Wheel diameter = 908 mm
- Profiles as measured at the end of the test
- Roller diameter = 2076 mm

### Presumed test conditions

Presumptions based on the analyses in [7]

- Young´s modulus $E = 210$ GPa
- Poisson´s ration $\nu = 0.28$
- Rail inclination = 1/100–1/40
- $\Delta Y = 11.9$ mm
- $\mu = 0.15$–$0.2$

# 4. A note on the evaluation of fatigue criteria

## 4.1 Background

In INNOTRACK varying test bench tests have been performed, see [1, 2]. The test conditions have been defined by component geometry and applied load, but also by factors such as applied lubrication (water spray), which will alter the coefficient of friction between wheel and rail.

The operational conditions were considered in a subsequent derivation of wheel–rail contact stresses [5]. It was, among other things, found that for the full-scale rigs, the conformal contact made contact stress evaluation very sensitive to the relative lateral position of the wheel and rail.

In this report an attempt is made to identify suitable fatigue life prediction criteria based on the test results and by making use of the previous work on identifying contact stresses. This raises the question: What is a good fatigue life prediction criterion?

## 4.2 Fatigue life prediction criteria

For steel alloys subjected to alternating uni-axial tension–compression there is a more or less linear relationship between the logarithm of a stress amplitude $\sigma_a$ versus the logarithm of the total number of cycles to failure *N*

$$N(\sigma_{\mathrm{a}})^{c_1} = C_2 \qquad (1)$$

where $c_1$ and $C_2$ are material parameters.

This relationship is normally referred to as the Wöhler or S–N-curve[2].

In the case of excessive global plasticity there is a more or less linear relationship between the logarithm of the fatigue life and the logarithm of the plastic strain amplitude.

$$N\left(\varepsilon_{\mathrm{a}}^{\mathrm{p}}\right)^{c_3} = C_4 \qquad (2)$$

where $c_3$ and $C_4$ are material parameters.

If the loading is more complex (pulsating tension, multi-axial etc), the common approach is to compensate by introducing an equivalent stress (or strain). In the following such an approach will be adopted. Different candidate equivalent measures will be employed and their suitability will be judged by whether a more or less linear relationship between the logarithm of the fatigue life and the logarithm of the considered equivalent stress/strain measure.

---

[2] A lin-log relationship between stress amplitude and fatigue life is often presumed instead of the log-log relationship considered here.

# 5. Engineering criteria for RCF life prediction

In the following is a description of the two engineering criteria that will be adopted for the RCF life prediction. It should be noted that there are other criteria that can be considered. One example is the $T\gamma$ (wear number) approach that relates the RCF loading to the total creep force ($T$) and the creepage ($\tilde{\gamma}$) A local approach is to instead relate the RCF life to a damage parameter described by the tangential stress ($\tau$) and the slip velocity ($v_{\text{slip}}$). In the current study this has not been possible. Since there have been no simulation of wheel–rail dynamics the creepage and the slip velocity are unknown. Further, as a preliminary study presented in section 6.3.2 shows, it is not straightforward to evaluate these even if wheel–rail dynamics simulations are carried out.

## 5.1 Peak elastic shear stress magnitude

A straightforward approach to evaluate fatigue life is to relate the risk of RCF initiation to the peak magnitude of the elastic interfacial shear stress $\tau_{\text{max}}$. These are usually evaluated by Hertzian theory. However in INNOTRACK it has previously been shown that under the conditions with conformal contact that prevail in the full-scale test rigs this is not a suitable approach. Instead interfacial shear stresses were derived using non-Hertzian methods, see [2, 5].

## 5.2 The shakedown diagram and the fatigue index $FI_{\text{surf}}$

The shakedown diagram [3] represents the operational conditions by two parameters:

- the Hertzian peak contact pressure, $p_0$ normalised by the cyclic yield limit in shear, $k$
- the traction coefficient $f = F_{\text{lat}} / F_{\text{n}}$

Here $F_{\text{n}}$ denotes the magnitude of the normal contact load (basically vertical load) and $F_{\text{lat}}$ the total lateral load magnitude ( $F_{\text{lat}} = \sqrt{F_x^2 + F_y^2}$ )

The peak contact pressure under Hertzian conditions is

$$p_0 = \frac{3F_{\text{n}}}{2\pi ab} \tag{3}$$

Where $a$ and $b$ are semi-axes of elliptical Hertzian contact patch.

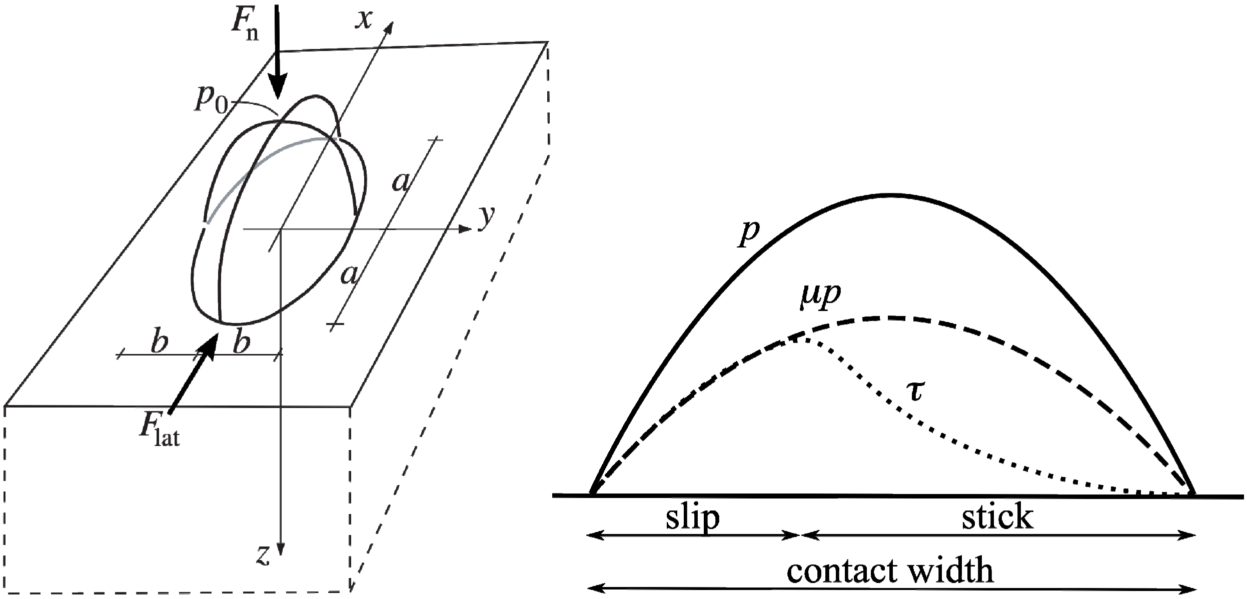

Figure 1 Left: Definition of vertical load, lateral load and semi-axes of the Hertzian contact patch.
Right: Definition of Hertzian contact pressure p and interfacial shear under full slip (dashed) and partial slip conditions (dotted).

The shakedown analysis presumes Hertzian contact conditions (elastic material response, smooth contact geometry, semi-infinite contacting bodies, [8]) and full slip. This means that the (local) interfacial friction stress $\tau$ is proportional to the contact pressure $p$, i.e. $\tau = \mu \cdot p$. The peak interfacial friction stress will thus be predicted to occur in the centre of the contact and have a magnitude of $\tau_0 = \mu \cdot p_0$ with $\tau_{\max}$ as defined in section 5.1. Note that with the exception for the case of full slip and a Hertzian contact stress distribution $\tau_0 \neq \tau_{\max}$.

A criterion for surface plasticity may now be expressed as

$$\tau_0 = k \tag{4}$$

As mentioned above $k$ is the yield limit in cyclic shear of the material in contact, which may vary with strain hardening of the material etc, but is here taken as the bulk material value.

Using equation (3) and the presumption of full slip, the criterion in equation (4) may be expressed as

$$\mu p_0 = \mu \frac{3F_n}{2\pi ab} = k \tag{5}$$

which may be rewritten as

$$\frac{3F_n}{2\pi abk} = \frac{1}{\mu} \tag{6}$$

This is the equation employed in the shakedown map, visualized as a bold line in Figure 2.

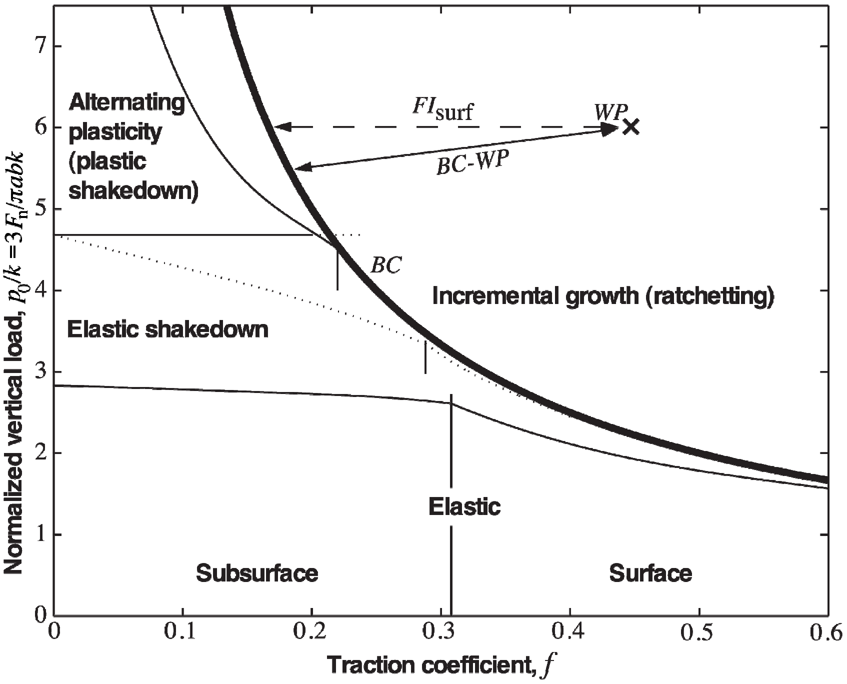

Figure 2 Shakedown map. *FI*<sub></sub>$_{\text{surf}}$ is defined as the horizontal projection of the distance from the yield limit. Note the different scale on the axes that makes the magnitude of $FI_{\text{surf}}$ close to the distance between the working point and the yield limit (line marked *BC*–*WP* in the figure).

The yield criterion implicitly invoked in the shakedown map and expressed in equation (6) can instead be expressed by the dimensionless fatigue index [4]

$$FI_{\text{surf}} = f - \frac{2\pi abk}{3F_n} > 0 \qquad (7)$$

For line contact (as in twin-disc tests) equation (7) will lose its validity since $a \to \infty$. Instead we express it on the form

$$FI_{\text{surf}} = f - \frac{k}{p_0} > 0 \qquad (8)$$

where for line contact

$$p_0 = \frac{F'_n}{\pi b} \qquad (9)$$

where $F'_n$ is the contact load per unit length.

In the following the fatigue index $FI_{\text{surf}}$ will be employed as a measure of the rolling contact fatigue loading.

# 6. Evaluation of tests using engineering RCF criteria

## 6.1 Approach

As mentioned above, the two candidate measures for RCF life predictions to be adopted in the current study are

- Peak elastic shear stress magnitude
- The fatigue index $FI_{\mathrm{surf}}$

The elastic shear stress magnitude has been evaluated in a previous INNOTRACK report [5] and therefore poses no problem.

To evaluate the fatigue index $FI_{\mathrm{surf}}$ the following parameters need to be evaluated or known:

- The normal load $F_{\mathrm{n}}$
- The traction coefficient $f$
- The contact patch size as given by the Hertzian semi-axes $ab$ (or the semi-axis $b$ in the case of line contact)
- The yield limit in cyclic shear, $k$

The **normal load** is in the current study taken as equal to the applied vertical load. This ignores any influence of the rail head curvature and also neglects any vertical load taken by flange contact.

The **traction coefficient** corresponds to the applied traction. In the case of full slip the traction coefficient will equal the maximum coefficient of friction in the wheel–rail interface, i.e. $f = \mu$.

For the VAS and DB test stands the resulting lateral force could be evaluated from the simulations in [6] and [7] by integration over the contact area, i.e.

$$F_{\mathrm{lat}} = \int_A \tau \mathrm{d}A \qquad (10)$$

The traction coefficient can then be derived as[3]

$$f = F_{\mathrm{lat}} / F_{\mathrm{n}} \qquad (11)$$

In the evaluations below this has not been done. Instead full slip conditions have been presumed. Motivations for this presumption is given below.

The **contact patch size** is evaluated by Hertzian theory in the twin-disc test. In the full-scale test rigs, the evaluation is more cumbersome due to the conformal contact, which makes the Hertzian presumptions doubtful. Instead the size of the non-Hertzian contact area evaluated in [5] is approximated by an “equivalent Hertzian contact patch” and defined by two “equivalent Hertzian semi-axes”, $a$ and $b$. Another approach (likely to yield very similar results) is to replace $\pi ab$ by the actual area of the non-Hertzian contact patch.

The **yield limit in cyclic shear** is in the current study presumed to be 300 MPa. Variation of $k$ due to strain hardening/softening and/or the influence of local residual stresses could be considered by relating shear yield to tensile yield, and in turn, relating tensile yield to material hardness (hardness in SI units, rather than Vickers number).

$$k \approx \frac{\sigma_{\mathrm{yield}}}{\sqrt{3}} \approx \frac{H_{\mathrm{V}}}{3\sqrt{3}} \qquad (12)$$

This refinement in modelling has not been pursued in the current work. Two reasons for this are the uncertainties in input data in particular for the full-scale tests and also the need for a very high resolution in the hardness measurements to capture the high gradients below the contact surface.

---

[3] Note that $F_{\mathrm{lat}}$ is generally not equal to the applied lateral load ($F_{\mathrm{y}}$ with the coordinate system of Figure 1) due to the influence of the curved wheel and rail profiles and possible flange contact.

## 6.2 Evaluation of twin-disc tests

The tested twin discs were made of R7 wheel steel and Corus 400 rail steel, respectively.

The twin-disc tests feature line contact between two cylindrical discs. In the studied test the maximum Hertzian contact pressure is $p_0$ = 1500 MPa [5]. The test features an initially dry phase with $\mu \approx 0.4$ to 0.45 followed by a lubricated phase with $\mu \approx 0.15$ to 0.2. Full slip is presumed.

### 6.2.1 Peak elastic shear stress

Presuming full slip results in a peak elastic shear stress $\tau_{\max} = \mu p_0$. For the case of dry contact this corresponds to magnitudes of 600 to 675 MPa. For the lubricated cycles, the corresponding magnitudes are 225 to 300 MPa.

### 6.2.2 Fatigue index $FI_{\text{surf}}$

Presuming the cyclic yield limit in shear is $k$ = 300 MPa, the load cases above can be introduced in a shakedown diagram as in Figure 8, with $p_0/k$ =5.

Employing the measured coefficients of friction, the fatigue index according to equation (8) will for the dry test stage be

$$0.4-\frac{300}{1500}=0.20\le FI_{\text{surf}}\le 0.45-\frac{300}{1500}=0.25 \tag{13}$$

That is a fatigue index $FI_{\text{surf}}$ in the range 0.2 to 0.25

For the lubricated test stage we obtain

$$0.15-\frac{300}{1500}=-0.05\le FI_{\text{surf}}\le 0.2-\frac{300}{1500}=0.00 \tag{14}$$

That is a fatigue index $FI_{\text{surf}}$ in the range –0.05 to 0.

Thus, for the presumption $k$ = 300 MPa no RCF initiation is predicted if only the lubricated test stage was employed. On the other hand RCF initiation is predicted under purely dry conditions. Previous tests on the SUROS machine have shown that under dry conditions many surface flakes develop of stable depth, even though the surface is wearing, i.e. there is an equilibrium reached between wear rate and the rate of crack tip advance into the material under dry conditions, see [9]. It is likely that the shift between RCF and wear as dominating damage mechanisms are at a lower magnitude of interfacial shear for twin-disc tests than for full-scale tests since the former feature very steep stress gradients at the surfaces. Consequently initiated surface cracks grow out of the highly stressed zone at an earlier stage and are therefore more likely to reach a constant growth rate in equilibrium with the surface wear rate.

For the current test conditions it is presumed that cracks are initiated at the dry test stage after which the lubrication propagated the initiated cracks. Operational conditions for dry and lubricated conditions are indicated in the shakedown map of Figure 8.

## 6.3 Evaluation of voestalpine full scale tests

For this test head checks evolved at a location 3 – 11 mm from the gauge corner of the rail after 20,000 to 50,000 cycles.

### 6.3.1 Peak elastic shear stress

In reference [6] the peak elastic shear stress was evaluated to $\tau_{\max}$ = 590 MPa using non-Hertzian contact mechanics analysis.

## 6.3.2 Fatigue index $FI_{\text{surf}}$

### Contact patch size

Figure 3 shows the contact patch as evaluated in reference [6] by a non-Hertzian analysis. An equivalent Hertzian contact patch" (blue ellipsis) has been matched to this contact patch. The "equivalent Hertzian semi-axes" of this ellipsis were found to be

- $a \approx 13$ mm
- $b \approx 7.5$ mm

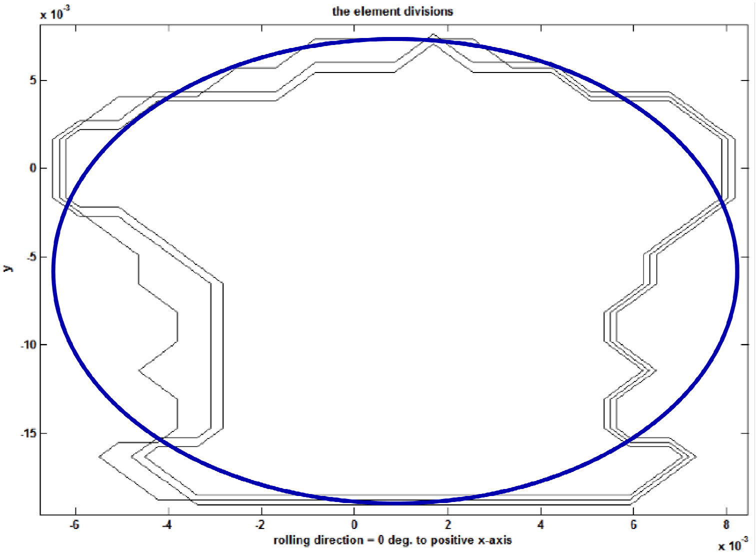

Figure 3  Contact area and "equivalent Hertzian contact area" for the VAS test sample.

### Traction coefficient

To evaluate the fatigue index $FI_{\text{surf}}$ we further need the traction coefficient $f$. To this end we need to evaluate the lateral forces (creep forces) at the wheel–rail interface.

If we first presume that the resulting lateral force is equal to the applied lateral load, we get $f = 39.2/196 \approx 0.2$. If we instead presume a condition of full slip, we get $f = \mu = 0.45$.

Judging from the elastic simulations in reference [6] the conditions should not be too far from full slip considering the ratio between maximum interfacial shear and maximum contact pressure being (according to) $\mu/p_0 \approx 0.59/1.3 \approx 0.45$. However in order to further investigate this a simulation of dynamic wheel–rail interaction was performed using the commercial code Gensys [10].

The Gensys simulation featured multi-point Hertzian contacts. To get an overview of the spread in prediction results and modelling sensitivity simulations featuring all 2 x 3 = 6 wheel and rail profiles measured after 20,000 cycles were carried out.

In Figure 4 lateral contact position on the rail, contact patch area, normal contact force and longitudinal creep forces are given. It is seen that with the exception of profile combination 1 all simulations feature three-point contact.

To set the rail coordinates in context the coordinate system of the rail profile adopted in the simulations is given in Figure 5. It is seen that a lateral contact position on the rail larger than some 30 mm corresponds to flange contact.

Creep forces in longitudinal (rail) direction ($F_x$ with the coordinate system of Figure 1) and in the wheel-axle direction ($F_y$ with the coordinate system of Figure 1) are plotted in Figure 8. From the results in Figure 8 it is seen that the simulation results are very sensitive to the chosen wheel and rail profiles. It is also seen that there is a large contribution to the total creep forces from the longitudinal creep. These relate to the inability of the conformal profile to steer solely by conicity, which results in the need for a steering moment that is supplied by the force-couple provided by longitudinal creep forces in two (or three) contact points.

The results in Figure 8 exemplifies the limitations of Hertzian contact analysis for the current load case as already pointed out in a previous INNOTRACK report [5]. Basically, the elongated non-Hertzian contact is split up in two (or three) Hertzian contact patches. This is not a major problem in vehicle dynamics simulations since the guiding forces will be similar. But for the current rolling contact fatigue analysis it is cumbersome since the stress distribution is not fully captured. Nevertheless it can be concluded that the presumption of full slip conditions is further supported. The longitudinal creep forces are not captured in the static simulations of [5] since they are a result of the wheel–rail dynamics. This means that on top of the interfacial shear stresses evaluated in reference [6] there will be a contribution from the longitudinal creep force, $F_x$, of a similar magnitude as the applied $F_y$. It should be noted that the applied shear stress will (presuming elastic conditions) not influence the size of the contact patch.

To derive a more exact magnitude of the total creep forces is likely to require simulations of the dynamic wheel–rail interaction that can consider non-Hertzian contact. For the current study it is presumed that the additional longitudinal creep force motivates a presumption of full slip.

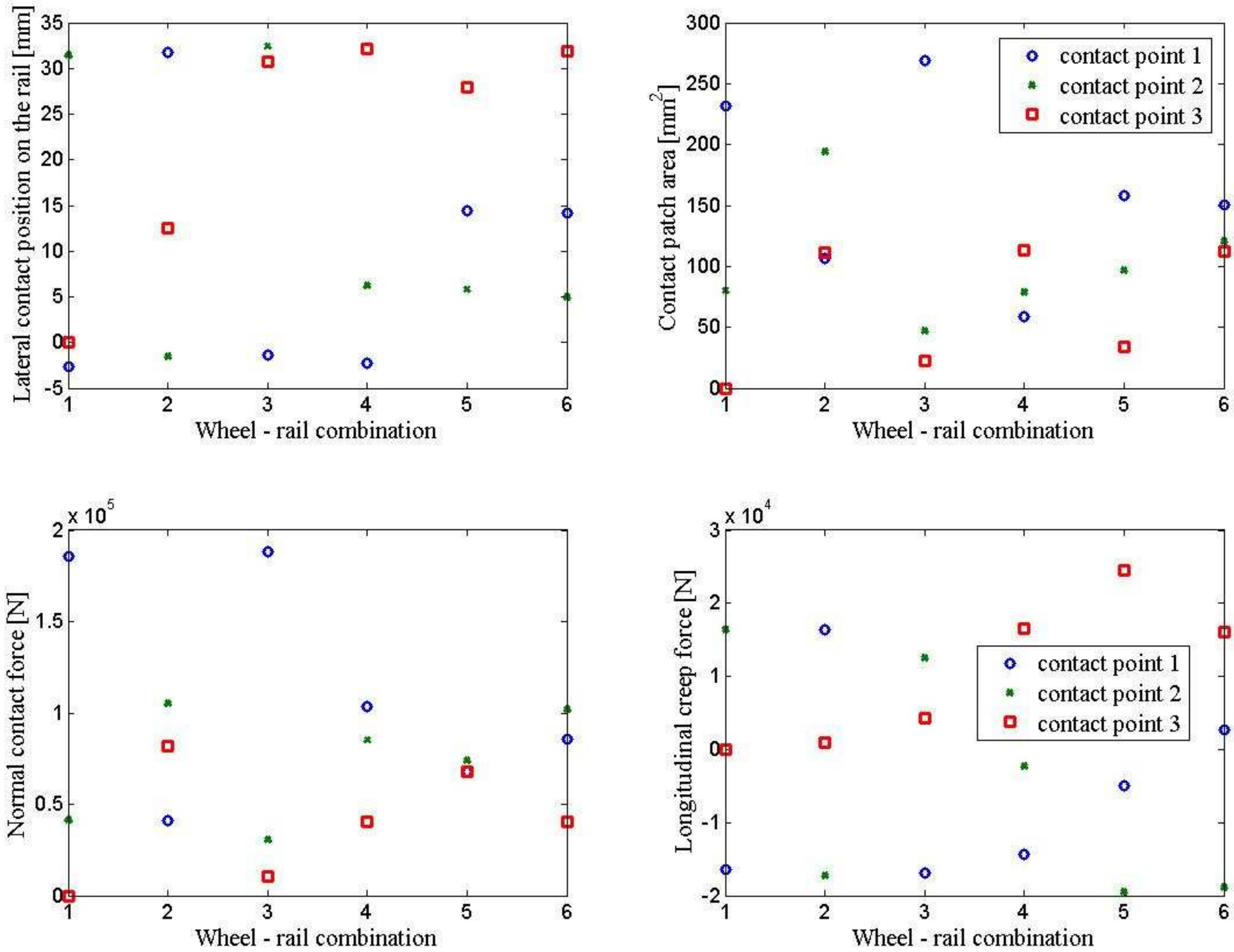

Figure 4 Results from analyses of dynamic wheel–rail interaction in the VAS test rig for 6 combinations of wheel and rail profiles measured after 20,000 cycles.

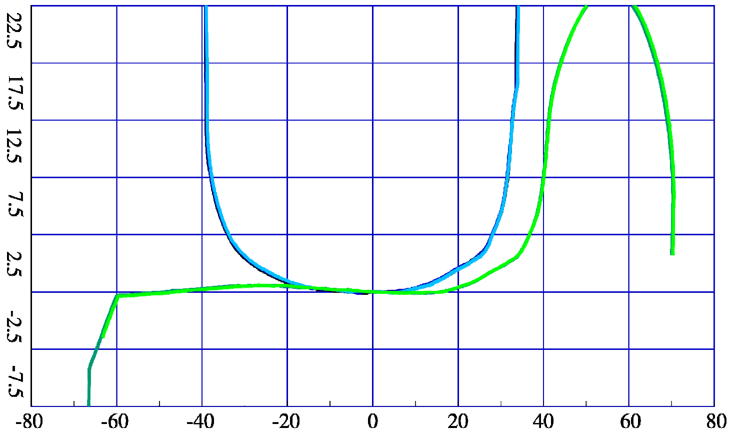

Figure 5 Employed coordinate system of the rail profile in the VAS test rig [mm].

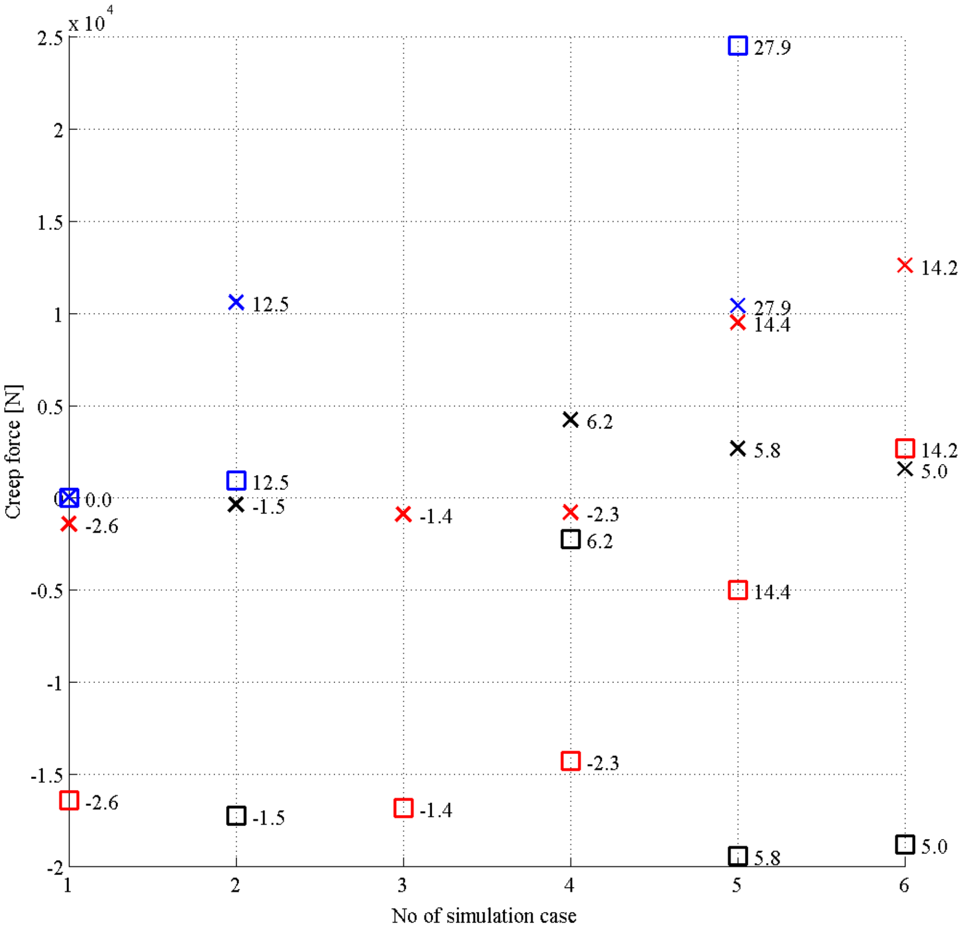

Figure 6 Creep forces evaluated from simulation of dynamic wheel–rail interaction in the VAS test rig [mm]. Squares indicate creep forces in the longitudinal direction (along the rail) and x:es creep forces in the wheel-axles direction. Red, black and blue indicates contact at contact point 1, 2 and 3, respectively. The numbering is equal to that of Figure 4. The number next to the marker indicates the lateral contact position on the rail in millimetres. Data for contact points > 30 mm have been ignored since they are considered to relate to pure flange contact.

### Evaluation of the fatigue index $FI_{\mathrm{sub}}$

From the “equivalent hertzian contact area” the peak hertzian pressure according to equation (3) normalised by the cyclic yield stress in shear is given as

$$\frac{p_0}{k} = \frac{3 \cdot 196 \cdot 10^3}{2\pi \cdot 13 \cdot 10^{-3} \cdot 7.5 \cdot 10^{-3} \cdot k} \tag{15}$$

Taking $k$ = 300 MPa gives $p_0/k \approx 3.2$.

Presuming full slip conditions we obtain for $f$ = 0.45 a fatigue index according to equation (7) as

$$FI_{\mathrm{surf}} = 0.45 - \frac{2\pi \cdot 13 \cdot 7.5 \cdot 300}{3 \cdot 196 \cdot 10^3} = 0.14 \tag{16}$$

For $f$ = 0.4 the corresponding fatigue index according to equation (7) is

$$FI_{\mathrm{surf}} = 0.4 - \frac{2\pi \cdot 13 \cdot 7.5 \cdot 300}{3 \cdot 196 \cdot 10^3} = 0.09 \tag{17}$$

# 6.4 Evaluation of DB full-scale tests

## 6.4.1 Peak elastic shear stress

In reference [6] the peak elastic shear stress was evaluated to $\tau_{\mathrm{max}}$ = 750 MPa using non-Hertzian contact mechanics analysis.

## 6.4.2 Fatigue index $FI_{\mathrm{surf}}$

Figure 7 shows the contact patch as evaluated in reference [6] by a non-Hertzian analysis. An equivalent Hertzian contact patch” (blue ellipsis) has been matched to this contact patch. The “equivalent Hertzian semi-axes” of this ellipsis were evaluated as

- $a \approx 3.2$ mm
- $b \approx 8.9$ mm

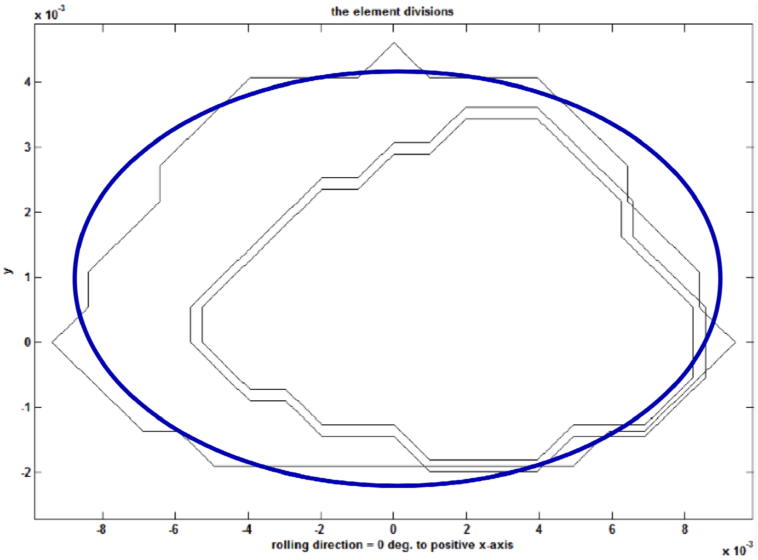

Figure 7 Contact area and “equivalent hertzian contact area” for the DB rig C test sample.

The corresponding normalised vertical load will be

$$\frac{p_0}{k} = \frac{3 \cdot 147 \cdot 10^3}{2\pi \cdot 3.2 \cdot 10^{-3} \cdot 8.9 \cdot 10^{-3} \cdot k} = \frac{2460 \cdot 10^6}{k} \tag{18}$$

Taking $k = 300$ MPa gives $p_0/k \approx 8.2$.

If we presume a condition of full slip, we have $f = \mu$. This should be compared to the evaluated ratio between maximum interfacial shear and maximum contact pressure (according to elastic simulations reported in table 3 of [7]) of $\mu/p_0 \approx 0.75/4.1 \approx 0.18$.

The corresponding fatigue index with $f = 0.2$ according to equation (7) will be

$$FI_{\text{surf}} = 0.2 - \frac{2\pi \cdot 3.2 \cdot 8.9 \cdot 300}{3 \cdot 147 \cdot 10^3} = 0.08 \tag{19}$$

With $f = 0.15$ we obtain

$$FI_{\text{surf}} = 0.15 - \frac{2\pi \cdot 3.2 \cdot 8.9 \cdot 300}{3 \cdot 147 \cdot 10^3} = 0.03 \tag{20}$$

## 6.5 Summary of RCF life predictions using engineering criteria

In Figure 8 the operational conditions of the different tests are summarised in a shakedown map. It is seen that under the assumptions detailed above surface initiated RCF is predicted for all test conditions with the exception of the wet twin-disk tests. Note however that the shakedown map gives no prediction of the number of cycles to initiation.

It can be noted that the test conditions cover a wide span of operational conditions both regarding applied traction and (equivalent) Hertzian contact pressures. This is a good thing if the validity of different RCF prediction models is to be tested.

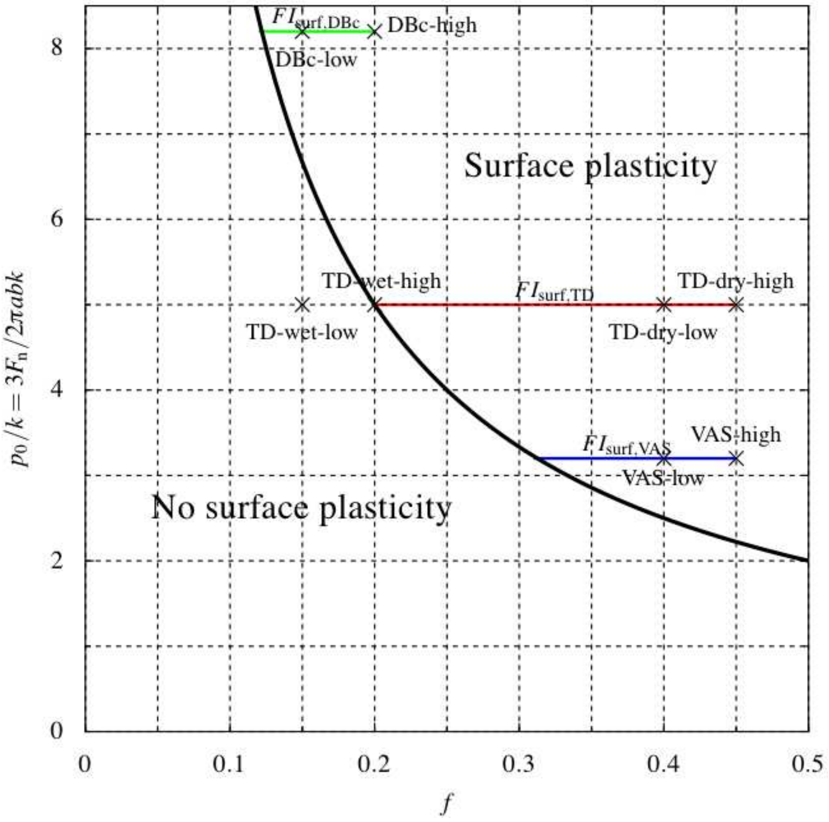

Figure 8 Operational conditions for all tests plotted in a shakedown map. The cyclic yield stress is presumed to be $k = 300$ MPa.

In Table 1 evaluated magnitudes of the two different RCF measures employed in the current study are summarized.

Table 1 Summary of RCF parameters of various criteria for the studied test conditions.

| RCF criterion | Twin-disc, dry | Twin-disc, lubricated | VAS | DB |
|---|---|---|---|---|
| $FI_{\mathrm{surf}}$ ($k$ = 300 MPa) | 0.2 to 0.25 | -0.05 to 0 | 0.09 to 0.14 | 0.03 to 0.08 |
| $\tau_{\mathrm{max}}$ | 600 to 675 MPa | 225 to 300 MPa | 590 MPa | 750 MPa |
| | Initiated cracks and surface flakes before 5 000 cycles. | Surface flaking by 5000 cycles following the dry test stage. | Head check initiation after 20 000 to 50 000 passes. | No head check initiation after about 1.2 million cycles. Embryonic cracks found in microscopy examinations. |

Figure 9 and Figure 10 shows a plot of the RCF measures versus the measured fatigue life. As discussed in section 4, a Wöhler-type of fatigue life relationship corresponds to a straight line in a log–log-diagram of stress (as quantified by a suitable measure) versus fatigue life.

It is seen that the peak interfacial shear stress does not give a good correlation to the RCF life. This is due to the low interfacial shear stress. As discussed in section 6.3 the derivation of $\tau_{\mathrm{max}}$ in reference [6] does not account for the longitudinal creep force that results from the dynamic wheel–rail interaction.

In Figure 10 $Fi_{\mathrm{surf}}$ magnitudes corresponding to low and high estimations of the traction coefficient for the test rigs have been plotted towards the measured RCF life. The fatigue index $Fi_{\mathrm{surf}}$ seems to be a promising measure. There is a clear correlation between a higher $Fi_{\mathrm{surf}}$ magnitude and a shorter fatigue life and there is close to a linear match in the log-log scale.

In this context it must be remembered that the prediction of surface initiated RCF life presented here rests on a number of assumptions. These will be discussed more in section 9 below. Further it should be observed that the analyses in the current report are based on only three tests.

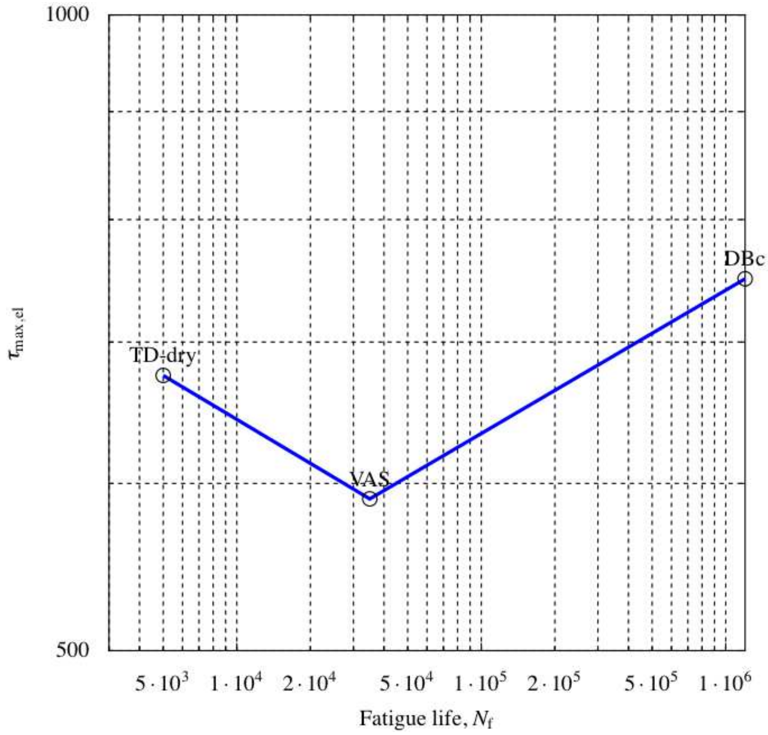

Figure 9 Experimentally found RCF life as a function of $\tau_{max}$ as evaluated in reference [6].

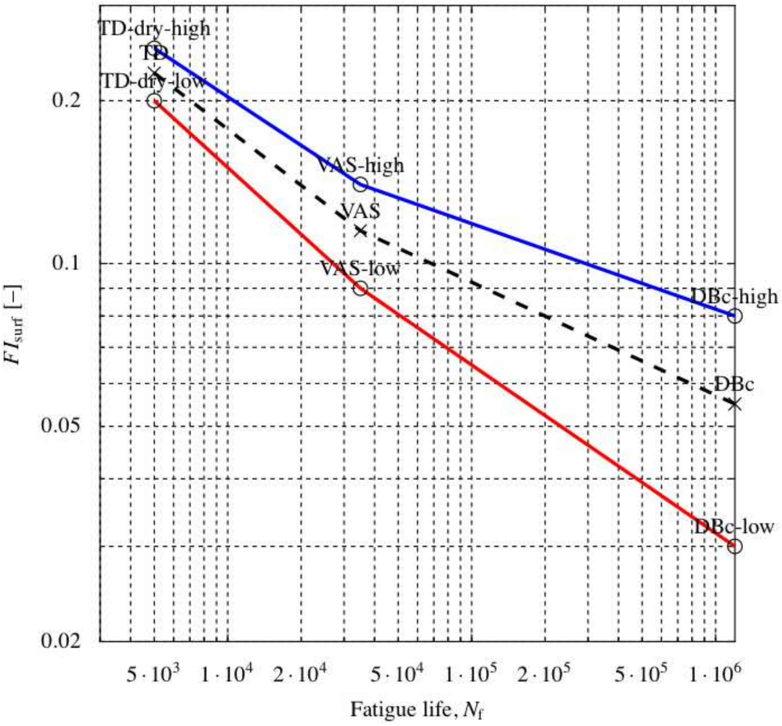

Figure 10 Experimentally found RCF life as a function of $FI_{surf}$. The upper graph corresponds to a high and the lower graph to a low estimation of the traction coefficient. The dashed line corresponds to the mean value.

# 7. Finite element simulations of material deterioration

The fatigue index $FI_{\text{surf}}$ contains a single material parameter, namely the yield limit in cyclic shear. This is a benefit in that the criterion can be employed also with very limited knowledge on the rail material. However it is also a drawback in that the criterion is not good in distinguishing between the RCF characteristics of different materials. Since bench tests are often employed to test new rail materials this is a real issue in the current study.

To obtain a refined analysis of surface initiated RCF there is a need to turn to finite element simulations. To capture the major plastic deformation in the wheel–rail a sophisticated constitutive model of the rail material is needed. The simulations further need to be able to correctly evaluate the high contact stresses (contact pressure and interfacial shear). This requires an advanced contact analysis in the FE-simulations. Due to the sensitivity of the problem studied penetration that always occurs in FE-simulations of contact needs to be confined to very low magnitudes (on the level of some micrometers).

Further, the high stress gradient that occur just below the rail surface need to be captured. To this end a locally very dense mesh is required. Since the simulations feature measured profiles that are not symmetric and also flange contact is accounted for, a full three-dimensional simulation is required. This leads to very computationally demanding simulations.

The current simulations were made using the commercial code Abaqus version 6.8.2 on Linux (Red Hat). The hardware mainly employed was a computational cluster (Svea) featuring 80 nodes with 8 Xeon E5430 (Harpertown) 2.66 GHz cores (dual quad core) and 16GB RAM, 2GB/core (see http://www.c3se.chalmers.se for more details). One simulation (typically featuring five wheel passages required in the order of 40 hours of CPU-time.

## 7.1 Finite element models

### 7.1.1 Finite element model of the voestalpine test rig

Details on the physical test set-up of the rig is given in references [1, 2].

#### Geometry

- Wheel diameter = 920 mm
- Profile geometry as measured at 20,000 passes (at rail position 1 and wheel position 1)
- Relative lateral position between wheel and rail according to estimations by voestalpine from Miniprof measurements for the chosen wheel 1 / rail 1 positions

Geometry and FE-mesh of the model is presented in Figure 11. The model includes a wheel and a rail part. Each part is divided into two sub-parts: In the volume close to the wheel-rail contact a sub-part with a dense FE-mesh is defined. The remaining volume is modelled by a sub-part featuring a coarser mesh. The sub-parts with different element sizes are connected during the analysis using a so-called tied connection. See the Abaqus 6.8.2 manual [16] for further information.

The length of the rail part is 20 cm and the wheel section covers about 30 degrees. Initial wheel-rail position is shown in Figure 12. Three dimensional continuum elements of type C3D8 (8-node linear brick elements) are employed for both the wheel and rail parts. The characteristic element size for the dense mesh of the rail part is 1.3 mm.

A reference point for the wheel part is introduced at the theoretical centre of the wheel, marked X in Figure 12. This reference point is used to apply boundary conditions and loads in a coherent manner. The reference point is rigidly connected to the upper wheel surface.

At the three points marked by square at the upper wheel surface in Figure 12 three soft springs (spring stiffness 10 N/mm) are introduced to prohibit (numerically predicted) rigid body motions. The spring elements are of type Spring1 (spring between a node and ground, acting in a fixed direction) and act in a vertical direction.

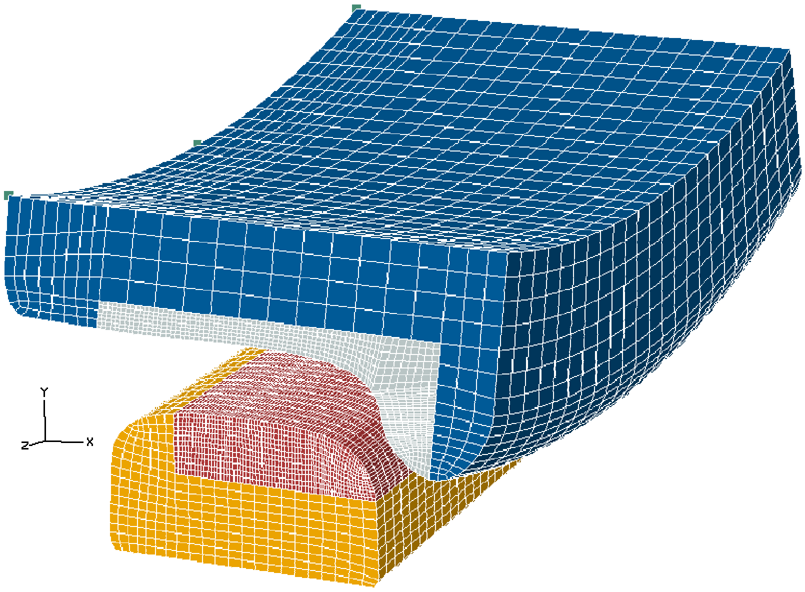

Figure 11 Geometry and FE-mesh for voestalpine test rig

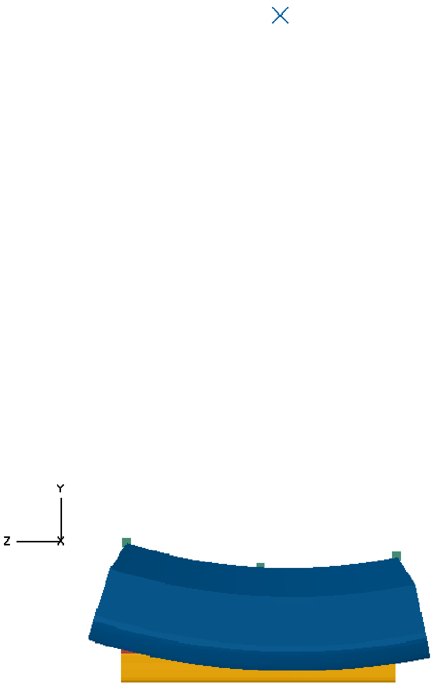

Figure 12 FE-model of the voestalpine test rig. Loads are applied in the reference point (marked X) corresponding to the centre of the wheel. Soft springs are introduced in points marked by squares to prevent rigid body motions.

## Loading

- Vertical load $F_y$ = - 196 kN (20t) (observe the employed coordinate system as defined in Figure 11)
- Lateral load $F_x$ = - 39.2 kN (4t)
- Maximum coefficient of friction $\mu$ = 0.45

### Material

The wheel is modelled as linearly elastic with the following material parameters:

- Young´s modulus $E$ = 210 GPa
- Poisson´s ration $\nu = 0.28$

The rail material is elasto-plastic with nonlinear isotropic and kinematic hardening. Details are given in section 7.2.

### Boundary conditions

- The displacements of the short sides of the rail part are restricted in the longitudinal and lateral directions.
- The bottom side of the rail part is fixed in the vertical direction.
- Rotations of the wheel are initially restricted via restriction on the rotation of the wheel reference point.

### Analysis procedure

A load passage is in the presented analysis divided into 4 numerical steps.

1. Application of vertical load.
2. Application of lateral load.
3. Rolling of the wheel along the rail.
4. Transition of the wheel back to the initial position.

Wheel-rail contact is established before step 1 and keeps under the steps 1-3. The contact is controlled during the analysis by assignment contact control parameters. Wheel part movement is realised via a prescribed displacement (24 mm in longitudinal direction) and rotation (3 degrees) in the wheel reference point. In total 4 load cycles containing steps 1 to 4 are performed.

Some key data regarding the employed FE-model of the voestalpine test rig:

- Number of elements 96175
- Number of nodes 114181
- Total number of variables in the model (degrees of freedom plus additional internal variables, e.g. for contact) 331377.

## 7.1.2 Finite element model of the DB test stand C

Details on the physical test set-up of the rig is given in references [1, 2].

### Geometry

- Wheel diameter = 908 mm
- Roller (rail part) diameter = 2076 mm
- Profile geometry as measured at the end of the test for wheel and rail (adopted from the file 00-2-000_1.xls).
- Relative lateral position between wheel and rail according to estimations by DB, see above
- Rail inclination = 1/40
- Angle of attack 0.25 degree = 4 mrad

Geometry and FE-mesh of the model is presented in Figure 13. The model includes a wheel and a rail part. Each part is divided into two sub-parts: In the volume close to the wheel-rail contact a sub-part with a dense FE-mesh is defined. The remaining volume is modelled by a sub-part featuring a coarser mesh. The sub-parts with different element sizes are connected during the analysis using a so-called tied connection

The rail (roller) sector is about 15 degrees; the wheel sector is about 30 degrees. Initial wheel-rail position is shown in fig FE-model of DB test rig. Three dimensional continuum elements of type C3D8 (8-node linear brick elements) are employed in the model for both wheel and rail parts. The characteristic element size for the dense mesh is 10 mm.

A reference point for the wheel part is introduced at the theoretical centre of the wheel. This reference point is used to apply boundary conditions and loads. The reference point is rigidly connected to the upper wheel surface.

In the same manner as for the numerical model of the voestalpine rig, soft springs (spring stiffness 10 N/mm) are introduced to prohibit rigid body motions.

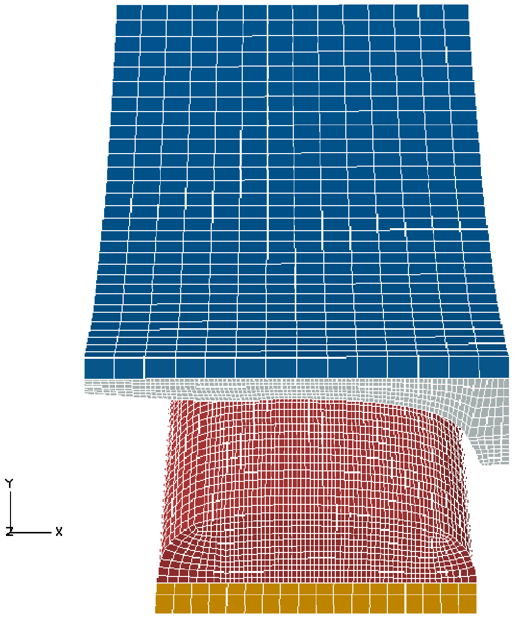

Figure 13 FE-model of DB test rig C.

## Loading

- Vertical load $F_y$ = - 147 kN (15 t) (observe the coordinate system)
- Lateral load $F_x$ = 0 / +15 kN (lateral loading applied in an additional analysis)
- Maximum coefficient of friction $\mu$ = 0.2

## Material

The wheel is modelled as linearly elastic with following material parameters:

- Young´s modulus $E$ = 210 GPa
- Poisson´s ration $\nu$ = 0.28

The rail material is elasto-plastic with nonlinear isotropic and kinematic hardening. Details are given in section 7.2.

## Boundary conditions

- The displacements of the short sides of the rail part are restricted in the longitudinal and lateral directions.
- The bottom side of the rail part is fixed in the vertical direction.
- Rotations of the wheel are initially restricted via restriction on the rotation of the wheel reference point.

## Analysis procedure

A load passage is in the current analysis is composed of 4 numerical steps.

1. Application of vertical load.
2. Rolling of the wheel along the rail.
3. Transition of the wheel back to the initial position.

Wheel-rail contact is established before step 1 and kept under the steps 1 and 2. The contact is controlled during the analysis by the assignment of contact control parameters. Wheel part movement is realised via a prescribed displacement (24 mm in longitudinal direction) and rotation (3 degrees) in the wheel reference point. In total 5 load cycles with steps 1 to 3 are carried out. In the additional analysis lateral load is applied during step 2 and an entire analysis performed in the same manner as for the voestalpine test rig analysis.

Some key data regarding the employed FE-model of the DB test rig:

- Number of elements: 72 100
- Number of nodes: 87 719
- Total number of variables in the model (degrees of freedom plus additional internal variables, e.g. for contact): 250 680.

## 7.2 Constitutive model for the rail steel

As discussed in section 4, the prediction of RCF life is related to evaluated strain (or stress). To obtain reliable results it is therefore vital that the constitutive model that is used to simulate the material response is sophisticated enough to be able to capture the state of stress and strain in the wheel–rail contact zone. Further the material parameters in the constitutive model need to be calibrated towards relevant experimental tests of the considered steel quality.

The constitutive model that has been employed in the current study is ABAQUS' model for cyclic plasticity with nonlinear isotropic/kinematic hardening [16] which is based on the work of Lemaitre and Chaboche [13].

The wheel is modelled as linearly elastic with Young´s modulus *E* = 210 GPa and Poisson´s ration $\nu = 0.3$. The constitutive model for the rail material is elasto-plastic with nonlinear isotropic and kinematic hardening based on the constitutive model of Lemaitre and Chaboche [13]. In the model the total strain rate is composed from the elastic and plastic strain rates

$$\dot{\varepsilon} = \dot{\varepsilon}^{\mathrm{el}} + \dot{\varepsilon}^{\mathrm{pl}} \qquad (21)$$

with the elastic part modeled as linear elastic and the plastic yield surface defined by the function

$$f(\sigma - \alpha) = \sigma^0 \qquad (22)$$

where

$$f(\sigma - \alpha) = \sqrt{\frac{3}{2}\left(\mathbf{S} - \alpha^{\mathrm{dev}}\right):\left(\mathbf{S} - \alpha^{\mathrm{dev}}\right)} \qquad (23)$$

where $\alpha^{\mathrm{dev}}$ is the deviatoric part of the backstress tensor and **S** the deviatoric stress tensor. The evolution of the backstress tensor is defined as

$$\dot{\alpha} = \frac{C_1 \dot{\bar{\varepsilon}}^{\mathrm{pl}}}{\sigma^0}(\sigma - \alpha) - \gamma_1 \alpha \dot{\bar{\varepsilon}}^{\mathrm{pl}} + \frac{\alpha \dot{C}_1}{C_1} \qquad (24)$$

with $C_1$ and $\gamma_1$ being material parameters.

In the current study we consider R260 steels. The stress–strain relationship for the steel under cyclic uni-axial loading has been experimentally evaluated. The material parameters of the constitutive relationship have been calibrated to the uni-axial test results. The testing and optimisation procedure is described in references [14] and [15].

The calibration of material parameters is governed by an optimisation criterion. In the current case it was decided to aim for a "best match" of model–experimental data in the short–medium term response (that is after the first cycles) and to obtain a good match between model–experimental peak stress–strain magnitudes and stress–strain ranges. To this end the first five load cycles in the laboratory testing have been utilised.

The results of the calibration of material data in the form of simulated and experimentally evaluated stress–strain data are shown in Figure 14 and Figure 15.

The following material parameters were obtained from the optimisation routine:

- yield stress at zero plastic strain, 443.0 MPa
- kinematic hardening parameter, $C_1$, 40995.0 MPa
- kinematic hardening parameter, $\gamma_1$, 58.0 [-]

Additional three more sophisticated constitutive models were under investigation for the employed FE-model. They seemed to give similar results as the Chaboche-model, but carried additional requirements. The most demanding of these was probably the need to implement the models as user subroutines. In addition the general rule of thumb is that the more sophisticated the constitutive model, the more cumbersome it becomes to obtain convergence in the contact algorithms. The results of the studies featuring the additional constitutive models were used as comparisons in evaluating the numerical models and are not included in the current report.

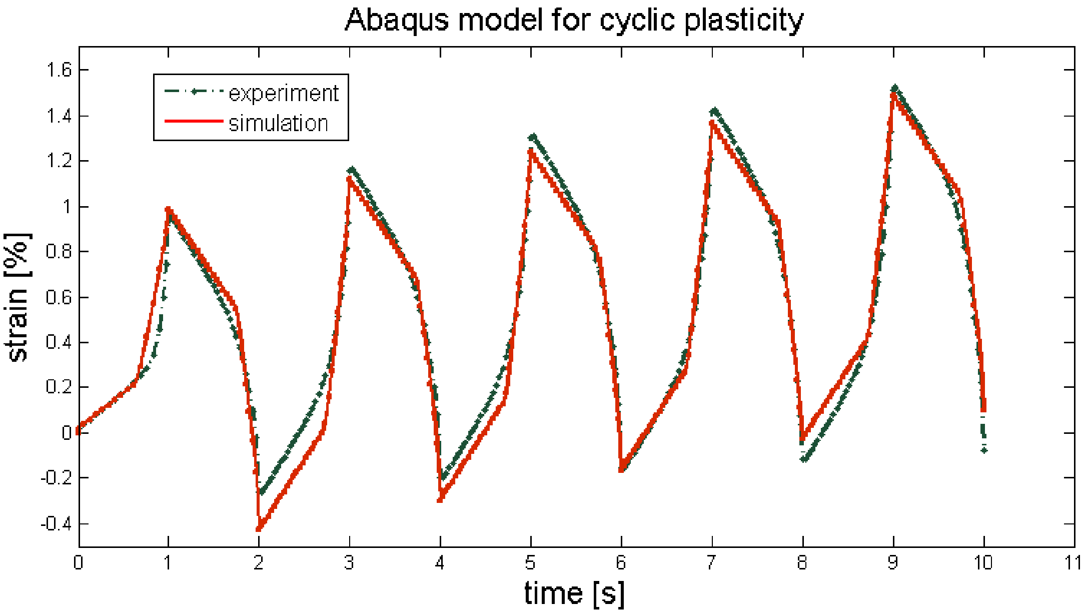

Figure 14 Comparison of simulated strain history and experimental cyclic test data.

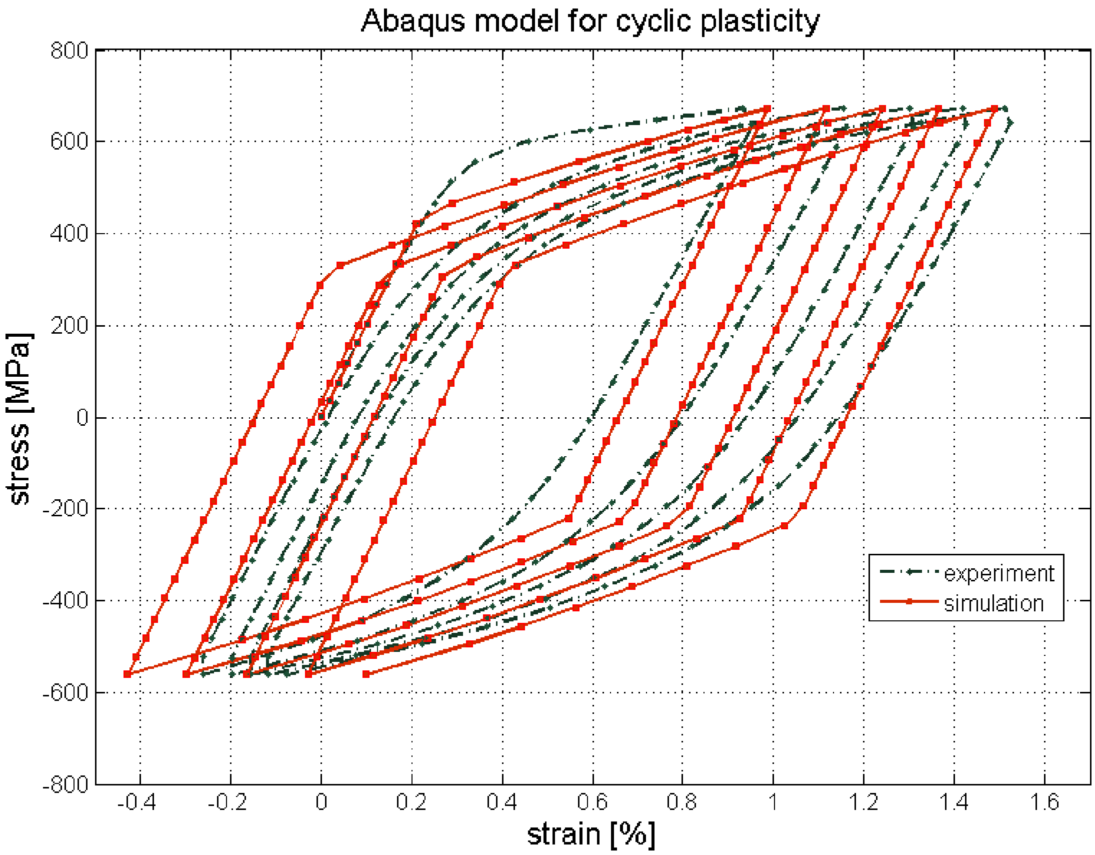

Figure 15 Comparison of simulated stress–strain evolution and experimental cyclic test data.

## 7.3 Results from FE-simulations of plastic deformation of the rail

Fringe plots are given in the appendices for the uppermost element layer at the rail surface. Results are evaluated at the integration points.

The results presented in the fringe plots include:

- von Mises effective stress defined as $q = \sqrt{3\sigma_{ij}^{\mathrm{d}}\sigma_{ij}^{\mathrm{d}}/2}$ where $\sigma_{ij}^{\mathrm{d}}$ denotes the deviatoric stress tensor and standard rules of index notation applies.
- contact pressure
- equivalent plastic strain, defined as $\bar{\varepsilon}^{\mathrm{pl}} = \bar{\varepsilon}^{\mathrm{pl}}\big|_0 + \int_0^t \dot{\bar{\varepsilon}}^{\mathrm{pl}}\mathrm{d}t$ where $\bar{\varepsilon}^{\mathrm{pl}}\big|_0$ is the initial equivalent plastic strain
- normal stress component in the *y*-direction corresponding to the direction of the applied vertical wheel load

The evaluation of the fatigue parameter FP, as discussed in section 8 is based on averaged node values.

Further, stress and strain evolutions presented in section 7.3 are averaged node values. The effective strain is here defined as $\varepsilon_{\mathrm{eff}} = \sqrt{2}/3\sqrt{(\varepsilon_x-\varepsilon_y)^2+(\varepsilon_y-\varepsilon_z)^2+(\varepsilon_z-\varepsilon_x)^2+6(\varepsilon_{xy}^2+\varepsilon_{yz}^2+\varepsilon_{zx}^2)}$ and the hydrostatic stress as $\sigma_{\mathrm{hydro}} = (\sigma_x+\sigma_y+\sigma_z)/3$. Both of these measures are invariants.

### 7.3.1 Results for the voestalpine test stand

In Appendix I results from the simulations featuring the voeastalpine test stand are shown. It is seen that the stress magnitudes are higher for load cycles 2 and onwards. This is particularly clear if the contact parssure is considered. To further investigate the cause, also the normal stress $\sigma_y$ was plotted.

It was found that the reason for the anomaly is related to a bug or lack of accuracy in Abaqus: When a load cycle is evaluated the wheel is lifted up and returned to the initial position after which the next load cycle is commences with the vertical loading. However the wheel is positioned with an initial penetration, which causes very high initial contact stresses (see the step 2, increment 1 plots in Appendix I and also the referenced animations).

Work in a work-around has been initiated. However, this is far from straightforward since a positioning of the wheel too far above the rail surface will also lead to problems in numerically establishing a physically sound contact. It should here be noted that the problem is extremely sensitive: the severe increase in contact stresses is believed to be caused by a penetration on the order of a millimetre. Further the problem is non-linear which makes the establishment of contact much more fragile. There are a multitude of contact parameters that can be tuned in the numerical evaluation, and every evaluation of a new approach takes in the order of a day to evaluate (the time to evaluate a full load cycle).

For information results from the simulations are presented below. When studying them, bear in mind that the initially applied contact pressure for load cycles 2 to 4 are too high. The response is evaluated in node 1165 of the rail part, which is located 56 mm from the gauge side. Note how the overloading mentioned above causes a severe increase in the effective strain for cycles 2 to 4 as shown in Figure 16.

In Figure 17 the hydrostatic stress is shown. Also here load cycles 2 to 4 show excessive magnitudes. Note also that due to the plastic deformation there will be a tensile residual hydrostatic stress.

In Figure 18 the evolution of stress and strain is given. In particular note the ratcheting behaviour of the $\sigma_z - \varepsilon_z$ and the $\tau_{xz} - \varepsilon_{xz}$ components.

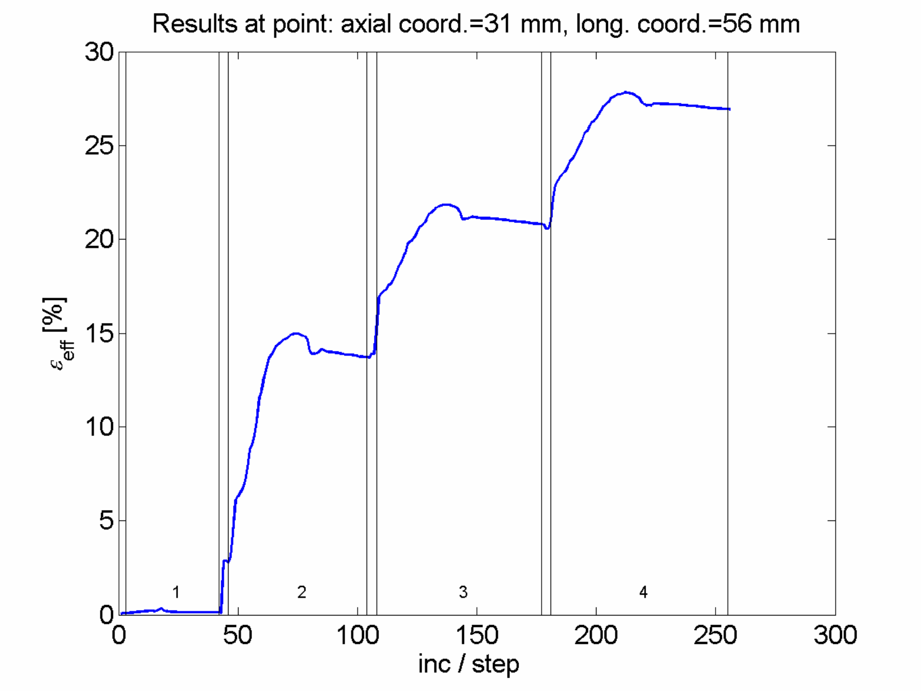

Figure 16 Evolution of the effective strain in node 1165 during the entire load history.

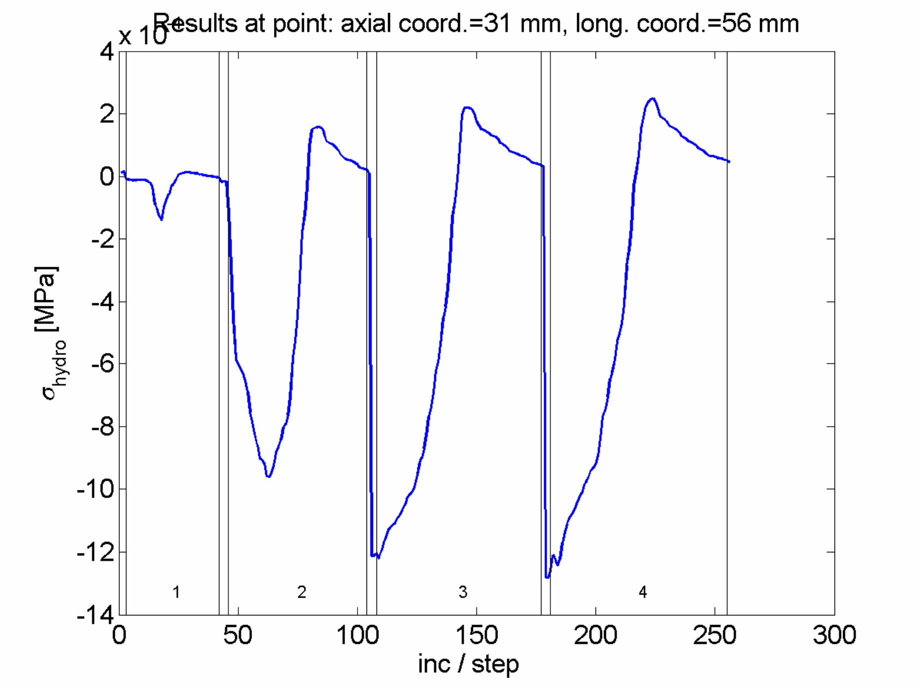

Figure 17 Evolution of the hydrostatic stress in node 1165 during the entire load history. A negative hydrostatic stress indicates overall compression.

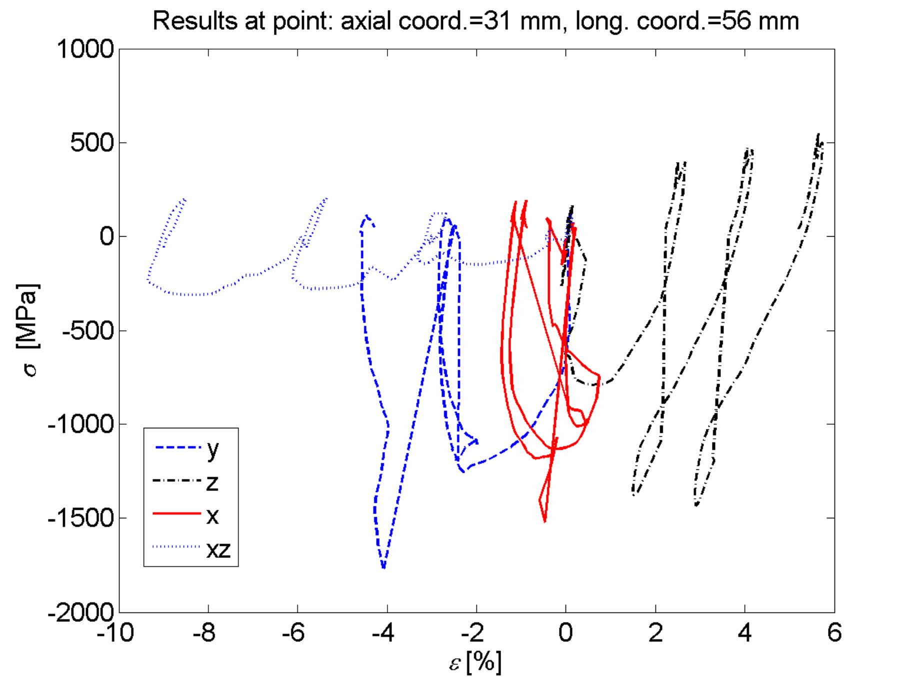

Figure 18 Evolution of stresses and strains in node 1165 during the entire load history. Coordinates *x*, *y* and *z* are according to Figure 11.

## 7.3.2 Results from the DB test stand C

In contrast to the results of the simulations of the voestalpine test stand, the simulations of the DB test stand show a good evolution of the contact stresses, as can be seen in Appendix II.

An in-depth evaluation of the response in node 4431 located 131 mm from the gauge side is presented below.

In Figure 19 the effective strain evolution is shown. Note how the largest increase in effective strain is for the first load cycle. This is due to the lack of containing residual stresses in the virgin material. Note further how the accumulated effective strain increases with every load cycle, which indicates a ratcheting material response.

Figure 20 shows the evolution of the hydrostatic stress Note here that the plastic deformation does, in this case, give raise to a compressive residual hydrostatic stress.

In Figure 21 the stress–strain evolution during five load cycles are shown. It is seen how the induced residual stresses confines the peak $\sigma_y$ magnitude and the ratcheting rate of the $\sigma_z - \varepsilon_z$ components. Further note the more moderate ratcheting of the $\tau_{xz} - \varepsilon_{xz}$ components as compared to the evaluated magnitudes for the voestalpine rig.

The simulation above was carried out with an angle of attack 0.25 degree and no additional lateral load. In the physical experiments, there was an oscillating lateral load $F_x$ varying from 5 kN 15 kN, see section 3.3. To evaluate the influence of the lateral load, a simulation was carried out

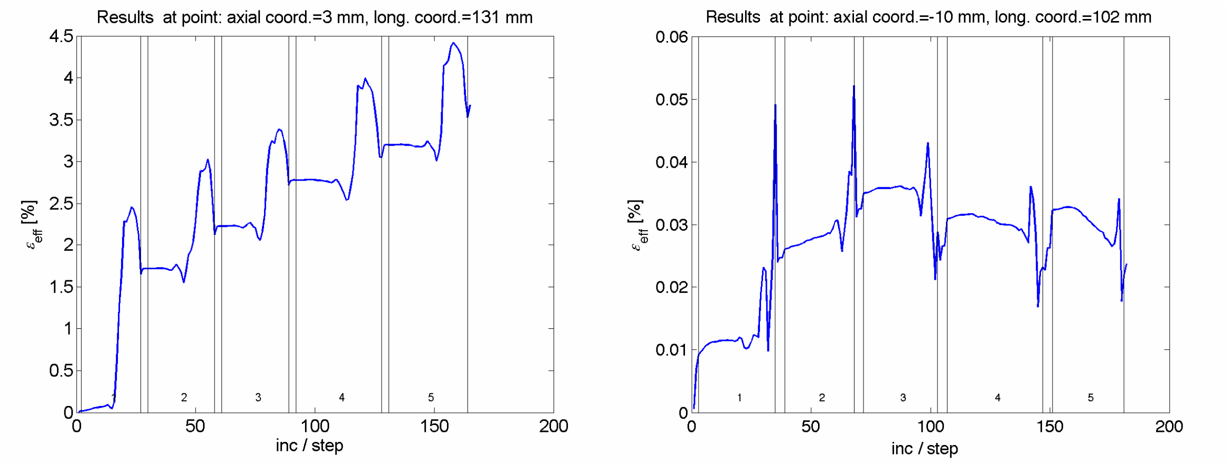

Figure 19 Evolution of the effective strain in node 4431 during the entire load history.
Left: lateral load Fx = 0 kN. Right: : lateral load Fx = 15 kN

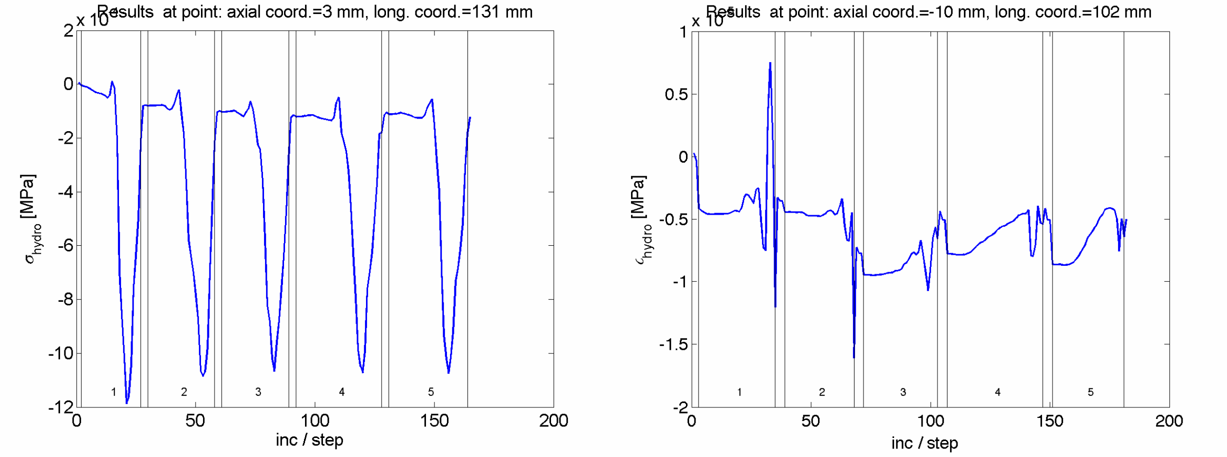

Figure 20 Evolution of the hydrostatic stress in node 4431 during the entire load history. A negative hydrostatic stress indicates overall compression.
Left: lateral load Fx = 0 kN. Right: : lateral load Fx = 15 kN

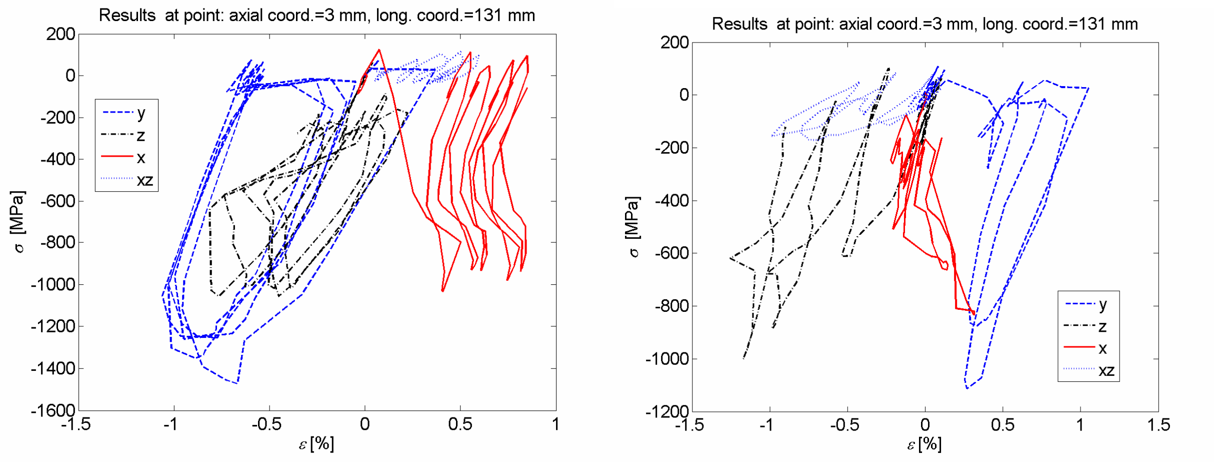

Figure 21 Evolution of stresses and strains in node 4431 during the entire load history. Coordinates *x*, *y* and *z* are according to Figure 13.
Left: lateral load Fx = 0 kN. Right: : lateral load Fx = 15 kN

# 8. Rolling contact fatigue analysis

Low cycle fatigue occurs when a material is repeatedly plastically deformed. The plastic deformation induces material damage. Once the damage exceeds a threshold a crack is initiated.

In low cycle fatigue analysis the fatigue life of a material point in a component is generally presumed to be proportional to the range of the local strain, $\Delta\varepsilon$ as in case 2 of Figure 22. If the plastic deformation is high enough and the applied stress has a mid value different than zero, ratcheting may occur, see case 3 of Figure 22. In this case plastic deformation is accumulated until the fracture strain is exceeded. This is often the case in RCF of rails. For that case, the analysis is complicated by the fact that the state of strain (and stress) is multiaxial. Further, there is a large confining hydrostatic pressure. This pressure tends to suppress the formation and growth of micro-cracks and thus has a beneficial influence in that the fracture strain is greatly increased.

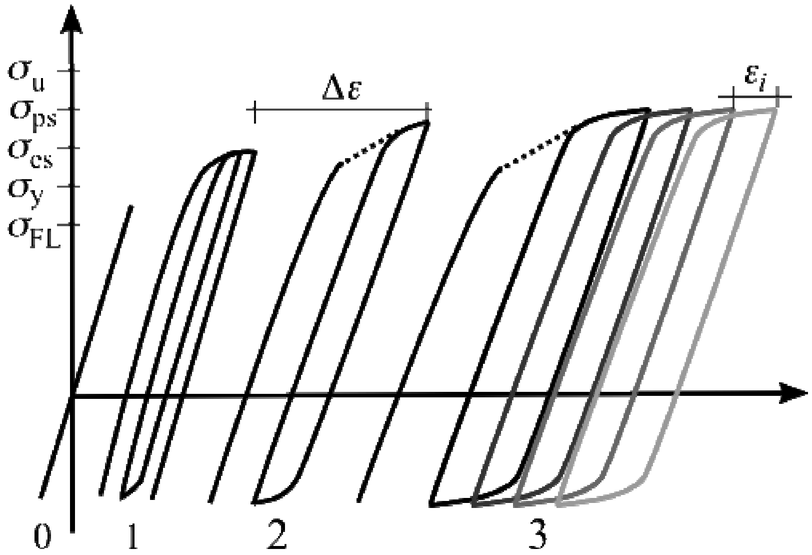

Figure 22 Material response under loading of varying magnitudes. 0: elastic loading, 1: elastic shakedown, 2: plastic shakedown, 3: ratcheting.

## 8.1 Low cycle fatigue analysis

For the current low-cycle fatigue analysis the Jiang–Sehitoglu criterion [17] has been employed. This criterion where a fatigue parameter FP is defined as

$$FP = \Delta\varepsilon \cdot \langle \sigma_{\max} \rangle + J \cdot \Delta\gamma\Delta\tau \qquad (25)$$

The criterion is evaluated for a material plane where $\Delta\varepsilon$ is the range of the normal strain acting on the plane, $\langle \sigma_{\max} \rangle = \max(\sigma_{\max}, 0)$ with $\sigma_{\max}$ being the largest normal stress on the plane. Further $J$ is a material parameter, $\Delta\gamma$ the range of the (engineering) shear strain and $\Delta\tau$ the range of the shear stress. Note that the evaluation of $\Delta\gamma$ and $\Delta\tau$ needs to account for the fact that these are vector quantities.

The fatigue life *N* can be evaluated from *FP* by an extension of traditional (uniaxial) low-cycle fatigue predictive models:

$$FP = \frac{(\sigma_f')^2}{E}(2N)^{2b} + \sigma_f'\varepsilon_f'(2N)^{b+c} \qquad (26)$$

where *E* is the elasticity modulus, and $\sigma_f'$, $\varepsilon_f'$, *b* and *c* are additional material parameters. Such an analysis has not been performed in the current study. Note that care must be taken if material parameters from “plain fatigue” are employed due to the different characteristics of rolling contact fatigue (beneficial bulk hydrostatic compression, possible hydro-pressure in initiated cracks etc).

In Figure 23 evaluated magnitudes of FP at the surface of the rail head are plotted for the four investigated load cycles for the voestalpine rig. As discussed above these magnitudes are unrealistic due to the intial penetration caused by the bug/lack of accuracy in the employed FE-code.

In Figure 24 and Figure 25 corresponding magnitudes are plotted for the DB rig without and with applied lateral load, respectively. In both cases there are two areas of high FP-magnitudes. In the case with no applied lateral loading, the band on the right will contain the highest FP-magnitudes as seen in Figure 24. In the case of an applied lateral load Fx = 15 the left band dominates, see Figure 25. This is the reason for the low stress magnitudes for the case of an applied lateral load found in section 7.3.2. In this case the left region will carry the load. The induced plasticity in this zone will even lead to an initially tensile hydrostatic stress in the right band as seen in 7.3.2. Eventually the load distribution will be more even, but also for the fifth load passage the highest load magnitudes are at the left band.

In the physical experiment the lateral load is varying between 5 and 15 kN. This will lead to a response varying between the cases shown in Figure 24 and Figure 25. Due to this alteration, the affected contact zone will be wider than the nominal zone for one loading condition. This will lead to a somewhat extended fatigue life for the component.

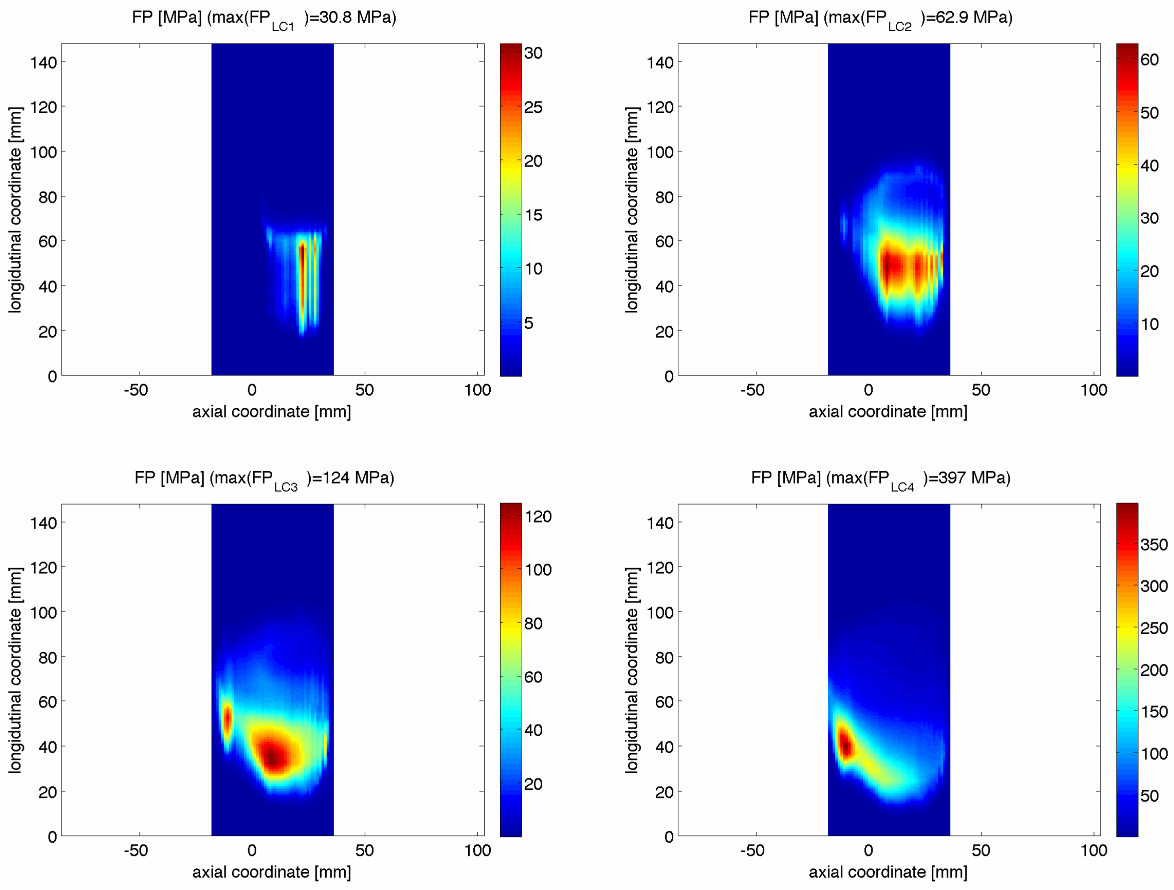

Figure 23 Evaluated fatigue parameter, *FP,* for the voestalpine rig. Results for load cycle 1 (top left), 2 (top right), 3 (bottom left) and 4 (bottom right).

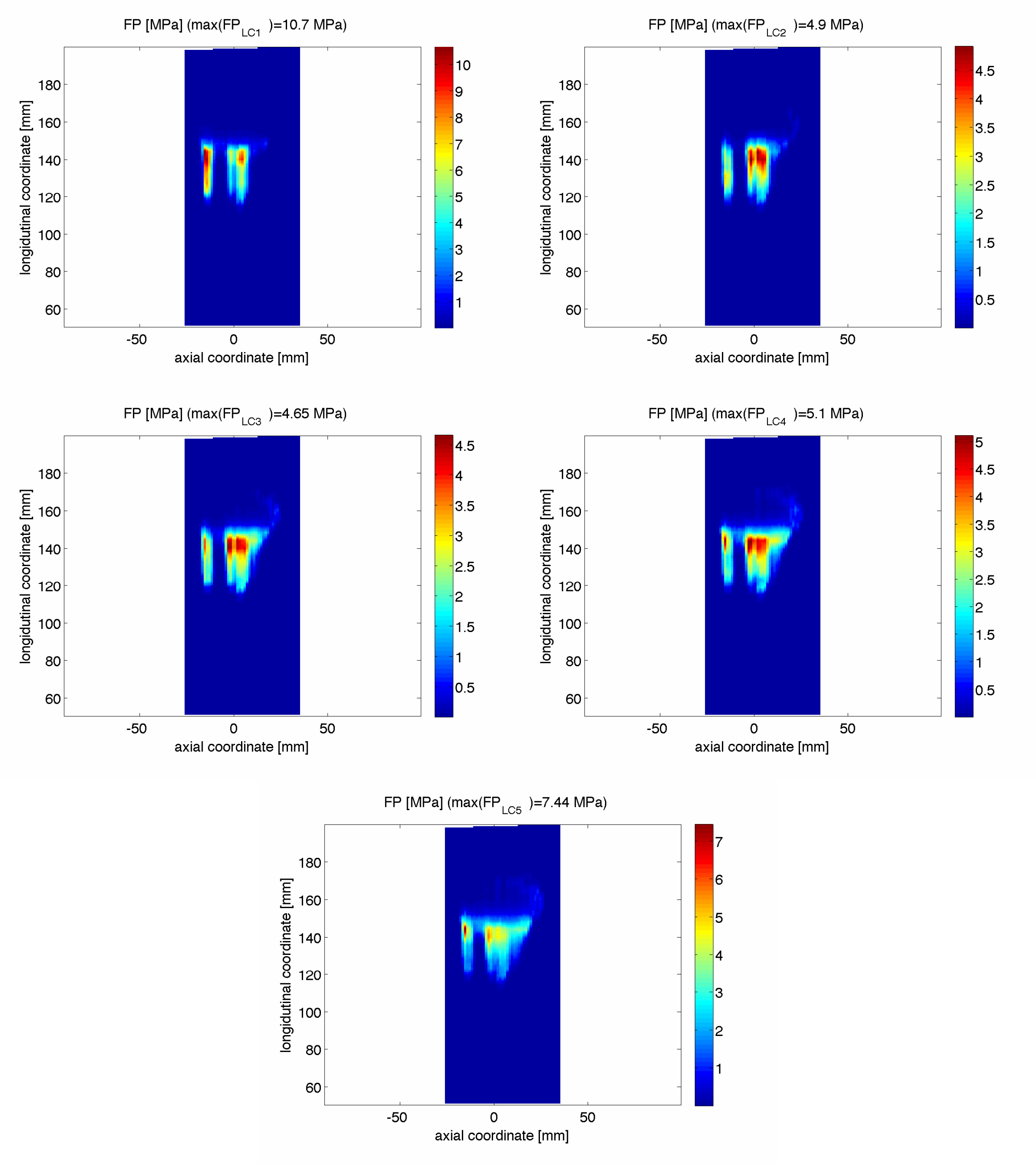

Figure 24 Evaluated fatigue parameter, *FP,* for the DB rig C with the lateral load $F_x = 0$. Results for load cycle 1 (top left), 2 (top right), 3 (mid row left), 4 (mid row right) and 5 (bottom).

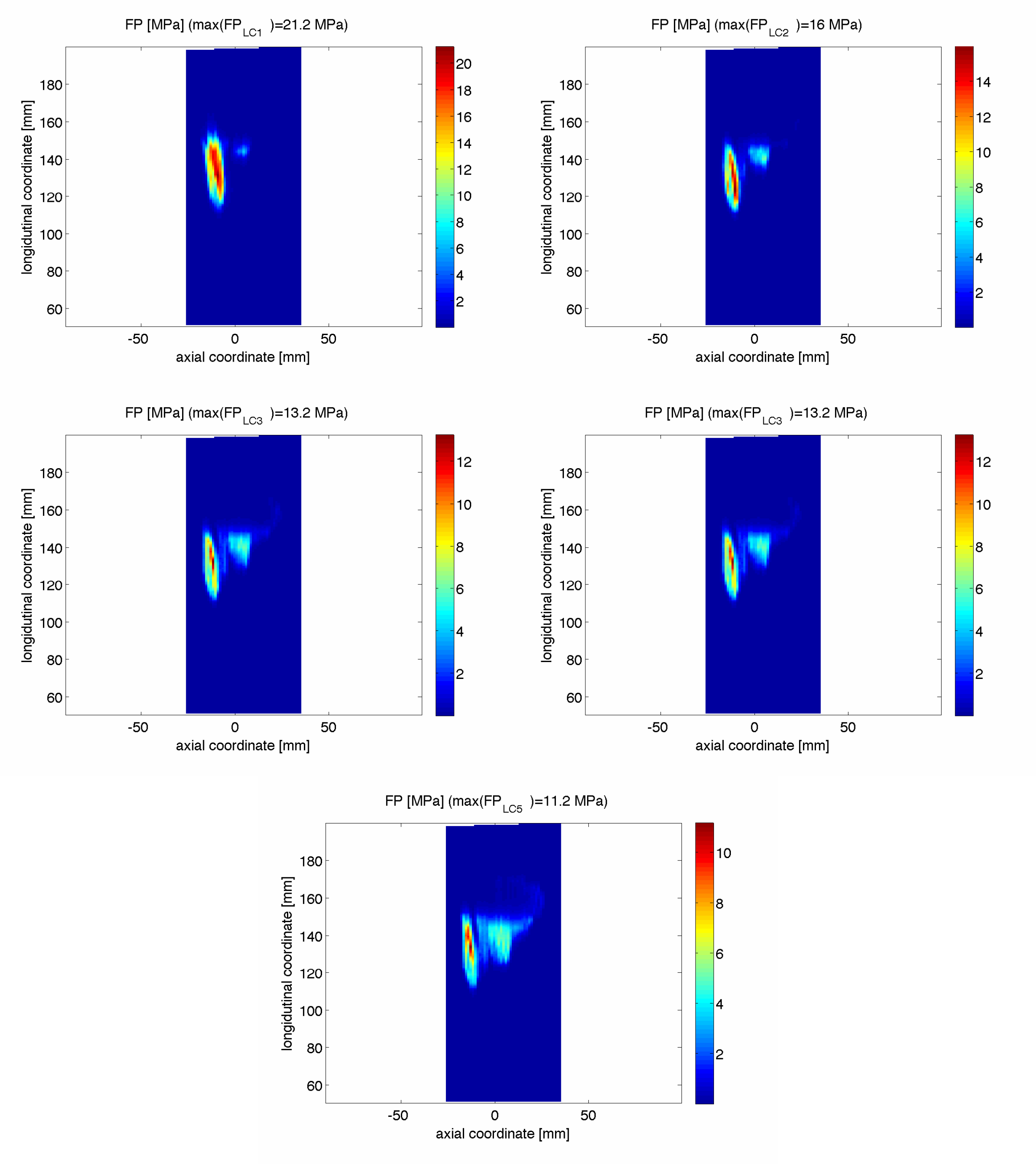

Figure 25 Evaluated fatigue parameter, *FP,* for the DB rig C with the lateral load $F_x$ = 15 kN. Results for load cycle 1 (top left), 2 (top right), 3 (mid row left), 4 (mid row right) and 5 (bottom).

## 8.2 Ratcheting analysis

Whereas low cycle fatigue analysis considers the damage mechanism to be the repeated (local) straining of a material point, ratcheting analysis presumes the damage mechanism to be the accumulation of plastic deformation. Once the accumulated strain magnitude exceeds the fracture strain of the material a crack is initiated.

If instead ratcheting is considered as the dominating damage mechanism, a ratchetting criterion may be employed [18]

$$\sum_{i} \varepsilon_i = \varepsilon_{\mathrm{c}} \tag{27}$$

Here $\varepsilon_i$ is the current strain increment and $\varepsilon_{\mathrm{c}}$ the fracture strain. When applied to surface initiated RCF in railway wheels $\varepsilon_i$ needs to account for the multiaxial state of strain. An approach to this is to define an effective strain increment in line with the use of equivalent stresses discussed above [18].

To employ the ratcheting criterion of equation (27), the strain increment $\varepsilon_i$ needs to numerically stabilise. This calls for the simulation of a large number of load passages to obtain a stabilised material response at the top of the rail head [19]. This roughly corresponds to 50–100 load passages. For the current models this is not possible with realistic computational times.

A simplified ratcheting analysis can instead be taken by employing the effective strain after five load passages as an indicator of the ratcheting response. This measure should be compared to the resistance of the material including the material’s ductility and ability to harden. It is not obvious which material quantities that are relevant in such an analysis.

# 9. Concluding remarks

The current report deals with the possibility of predicting surface initiation of rolling contact fatigue cracks. To this end a number of simulations and evaluations have been carried out:

- Elastic contact stresses have been evaluated by non-Hertzian contact theory. These simulations are presented in a previous INNOTRACK report [5].
- Fatigue indices based on shakedown theory have been evaluated and matched towards evaluated RCF lives to establish a Wöhler-like fatigue–life relationship.
- Simulation of dynamic wheel–rail interaction in a test rig has been adopted to further analyse longitudinal creep forces due to the conformal contact between wheel and rail.
- Material parameters in a constitutive model featuring non-linear kinematic hardening have been evaluated from experimental test data of cyclic deformation of rail steel.
- Non-linear FE-simulations of the elasto-plastic wheel–rail contact in the test rigs have been performed to evaluate elasto-plastic stresses and strains.
- The FE-simulations have been post-processed to evaluate measures that can be employed to predict RCF impact.

In conclusion the current study raises the possibility to compare test rig conditions. This is a good thing since the scaled geometry and the line contact conditions of the twin-disc tests make the state of stress in the discs not directly comparable to that in the wheel and rail of the full-scale test stands. On the other hand full-scale test stands cannot achieve the strain rates that are present under operational conditions. The possibility of combining twin-disc and full-scale tests should therefore be very valuable.

In addition the current study also gives the possibility to compare test stand conditions to operational conditions from an RCF impact point of view.

The study features both engineering approaches and results from three-dimensional elasto-plastic finite element simulations. It has been shown how both these approaches are on the brink of what is currently theoretically and practically possible form a computational point of view. Below the main findings and results of the study are commented and recommendations for future implementation are given.

## 9.1 RCF prediction using engineering models

The approach of adopting the fatigue index $FI_{\mathrm{surf}}$ as an RCF impact measure seems very promising. Simulations of tests in the three test rigs that featured a very broad range of load and geometry conditions. Despite this a clear Wöhler-like trend in the correlation between measured fatigue lives and the fatigue index $FI_{\mathrm{surf}}$ was found.

There are however a number of things that should be considered before this relationship is established as a “fact”:

- The magnitude of $FI_{\mathrm{surf}}$ is severely depending on magnitudes of interfacial shear stress. Currently the maximum coefficient of friction is not evaluated in the full-scale test rigs. Further, it is very cumbersome to numerically evaluate and/or measure the actual interfacial shear stress. Consequently the predictions have to be based on estimated values. From experiments, reasonable upper and lower limits can be established with some confidence, however due to the logarithmic relation between $FI_{\mathrm{surf}}$ and RCF life also a small deviation in $FI_{\mathrm{surf}}$-magnitudes will lead to major deviations in predicted RCF lives.
- The size of the contact patch will also influence predicted $FI_{\mathrm{surf}}$-magnitudes. A major work was carried out in a previous INNOTRACK report [5] to this end. Consequently the resulting error due to an erroneous estimation of the contact patch size in the current analysis is considered small.
- The analysis includes three tests, which is far to little considering the statistical spread in fatigue lives in general. On the other hand, the rolling contact fatigue initiation is strongly related to plastic deformation, which tends to decrease the statistical scatter. Further, the test conditions cover a very broad range of operational conditions, which means that “interpolation” rather than “extrapolation” can be employed for other conditions.

- The definition of "RCF-life" is not consistent between the tests. Further the detection of cracks is not completely reliable. In the current cases this was both due to the fact that RCF crack initiation is masked (worn away) by wear and that there was no continuous monitoring of crack initiation. However due to the logarithmic relationship between $FI_{\text{surf}}$ and RCF life this is most likely not a major issue: Even a rather large error in evaluated fatigue life corresponds to a comparatively small error in $FI_{\text{surf}}$-magnitude.
- Additional simulations of the dynamic wheel–rail interaction showed that a conformal wheel–rail contact gives rise to large longitudinal creep forces also for case where only no longitudinal load is applied. The simulations further demonstrated that for the current task of predicting surface initiated RCF under conditions of conformal wheel–rail contact, Hertzian contact models are not sufficient. This is in agreement with the conclusions in reference [5].
- The predictions rely on the presumption of full slip. For the current test conditions, this seems likely, considering the results of the additional simulations of dynamic wheel–rail interaction in the voestalpine test rig. However, this raises the question on how to deal with situations (e.g. in-field operations) where full slip is not prevailing.

Still the fact remains that the $FI_{\text{surf}}$ based predictions give correct qualitative trends. In particular, the longer than expected fatigue life for the DB test rig can be explained by the varying lateral load. As discussed in section 8.1 this will spread out the fatigue damage over a wider area and thus increase the fatigue life..

## 9.2 RCF prediction based on finite element simulations

From previous experience it seems that the main problem with shakedown maps is the inability to properly quantify fatigue resistance of different materials. Recall that the material characteristics are solely represented by the cyclic yield stress *k*. This is a very ambiguous parameter since it is not straightforward to measure and also may vary during the course of a test due to material hardening/softening and residual stress formation[4]. In the current study these obstacles are not introduced, but a detailed treatment for some specific cases is available, see references [11, 12]

To further this ability finite element simulations are likely to be necessary. Here the constitutive behaviour of the material is experimentally found and translated to a constitutive model. Using this constitutive model, plastic deformations are evaluated and related to the fatigue life of the component.

Elasto-plastic finite element simulations have the convenient property that they account for plastic deformation of the rail surface. This (and to some extent the discretization of the geometry and the contact algorithms in the FE-analysis) removes the need for "surface smoothing" that is needed in elastic contact analyses [5].

As shown in the report FE-simulations are very cumbersome. The very local high deformations in connection to the large displacement, the high contact pressures and interfacial shear stresses, the conformal contact and the need for sophisticated constitutive models puts tremendous challenges on the FE-code. In the current simulations success was obtained after months of non-converging solutions and still a bug (or lack of accuracy) has prevented a proper analysis of the voestalpine test rig. Naturally the removal of some of the demands would make the simulations much easier (though still far from straightforward). However it would also decrease the ability to simulate the "reality". As seen e.g. in the two analyses of the DB test rig the response is extremely sensitive to disturbances. To further aggravate this by simplistic modeling is not to be recommended.

Due to the numerical problems with the voestalpine test rig it has not been possible to compare predicted RCF lives with numerically found. It is however technically rather straightforward once the stress–strain evolution has been evaluated. In the report two possible indicators, the fatigue parameter *FP*, and the effective strain, have been described. Which is the more accurate depends on whether the damage is related more to low-cycle fatigue (in the sense that the fatigue life is related to the strain range) or to ratcheting. It should be noted that due to the sensitivity of the contact, the identification of critical regions (i.e. the regions most susceptible to RCF) is cumbersome. Consequently an automated procedure that evaluates RCF impact for the entire rail head is preferable.

---

[4] This implies that *k* is in fact not a pure material parameter, but also to some extent dependent on component geometry and loading conditions.

## 9.3 Recommendations

### 9.3.1 RCF life prediction using an engineering model

The current study has shown a feasible path to connect test bench experiments to operational conditions by the use of numerical simulations. Currently the procedure is rather cumbersome. Adopting engineering models it consists in:

- Evaluation of the contact patch size using non-Hertzian contact mechanics simulations.
- Evaluate traction coefficient from estimations/measurements of the coefficient of friction and numerical evaluation of the interfacial shear. In addition to the non-Hertzian contact mechanics simulations also creepage forces due to the dynamic wheel–rail interaction need to be considered.
- Evaluate the fatigue index $FI_{\mathrm{surf}}$ from equation (7) or (8).
- Relate $FI_{\mathrm{surf}}$ to a fatigue life using Figure 10.

To be operationally applicable, the following issues need to be addressed:

- The relative lateral wheel–rail positions need to be established in the experiments
- The coefficient of friction needs to be measured in the experiments
- The tractive force ($F_x$) needs to be evaluated in the experiments
- Less cumbersome methods to evaluate the contact patch size using non-Hertzian contact mechanics needs to be developed.
- Methods to numerically simulate the dynamic wheel–rail interaction accounting for non-Hertzian contact need to be developed.
- Methods of evaluating fatigue indices under partial slip conditions need to be established.
- The $FI_{\mathrm{surf}}$–fatigue life-relationship needs to be more firmly established with less uncertainty in predicted fatigue lives.
- The influence of lubrication (in the crack initiation and crack propagation phases) needs to be handled in a more stringent manner.

Here, the main challenges and also the most important aspects are to obtain reliable magnitudes of the contact patch size and the acting frictional stress.

### 9.3.2 RCF life predictions based on FE-simulations

Eventually FE-simulations are likely to be the way forward, partly for their ability to include the material characteristics in a much more refined way and partly because they reflect the physical damage processes in a more coherent manner. However before this is possible, several issues needs to be dealt with:

- The FE-codes need to be better in dealing with the combination of very local high deformations in connection to the large displacement, the high contact pressures and interfacial shear stresses, the conformal contact and the need for sophisticated constitutive models.
- There is a need to be better means of translating measured wheel–rail profiles to numerical models.
- More sophisticated methods of dealing with the sensitivity to load/geometry conditions are needed.
- The fatigue life predictions models need to be better calibrated to more laboratory tests.
- Since it will not be possible to simulate train–track interaction with detailed FE-models of the kind presented in the current report within the foreseeable future, there is also a need to translate the results from the FE-simulations to more “engineering-type” models.

Currently, the main stumbling block here is the limitations of the FE-codes. However, these are likely to be overcome. To compensate for the inherent sensitivity of the conditions in conformal contacts on the other hand is a major theoretical challenge.

### 9.3.3 Final conclusions

The current study is in many aspects groundbreaking. The combination of analyses and the comparison between test rigs have never before been published. It is believed that this is a major step forward, but it also highlights the shortcomings of the current top-notch analyses and procedures. It is perhaps here that the highest long-term benefit of the report lies.

# 10. References

1. INNOTRACK report D4.3.1 “Initial definition of conditions for testing matrix of rail steels and welds”, 24 pp
2. INNOTRACK report D4.3.3 “Results of first test rig measurements”, 87 pp
3. Johnson K L, The strength of surfaces in rolling contact, *IMechE, Mechanical Engineering Science*, vol 203, pp 151-163, 1989
4. Ekberg A, Kabo E & Andersson H, An engineering model for rolling contact fatigue, *Fatigue & Fracture of Engineering Materials & Structures*, vol 25, pp 899-909, 2002
5. INNOTRACK report D4.3.4 “Calculation of contact stresses and wear”, 23 pp and 4 appendices
6. Li Z, Analysis of the VAS test results, Appendix to INNOTRACK report D4.3.4 “Calculation of contact stresses and wear”, 21 pp
7. Li Z, Analysis of the DB rig C test results, Appendix to INNOTRACK report D4.3.4 “Calculation of contact stresses and wear”, 19 pp
8. Hertz H, Über die Berührung fester elastischer Körper, *Journal der reine und angewandte Mathematik*, vol 92, pp 156–171, 1882
9. Fletcher, DI, & Beynon, JH, Equilibrium of crack growth and wear rates during unlubricated rolling-sliding contact of pearlitic rail steel, *Proc Instn Mech Engrs Part F*, vol 214 (), pp 93-105, 2000
10. www.gensys.se
11. Kapoor A, Beynon J H, Fletcher D I & Loo-Morrey M, Computer simulation of strain accumulation and hardening for pearlitic rail steel undergoing repeated contact, *J. Strain Analysis*, vol 39, 383-396, 2004
12. Dyson I, Williams J & Kapoor A, The Effect of Surface Hardening on the Elastic Shakedown of Elliptical Contacts, *Proc IMechE Part J Journal of Engineering Tribology*, vol 213, pp. 287-298, 1999
13. Lemaitre J & Chaboche J-L, Mechanics of solid materials, Cambridge Univ. Press, 556 pp, 1990
14. Johansson G, Ahlström J & Ekh M, Parameter identification and modeling of large ratcheting strains in carbon steel. *Computers and Structures*, vol 84, pp. 1002-1011, 2006
15. Ahlström, J & Karlsson, B, Fatigue behaviour of rail steel - a comparison between strain and stress controlled loading. Wear, 258 (7-8) pp. 1187-1193, 2005
16. http://www.simulia.com/products/abaqus_fea.html
17. Jiang, Y, and H Sehitoglu, A model for rolling contact fatigue, Wear vol 224, pp 38–49, 1999
18. Kapoor, A, Re-evaluation of the life to rupture of ductile metals by cyclic plastic strain, Fatigue & Fracture of Engineering Materials & Structures vol 17, no 2, 201–219, 1994
19. Ringsberg, J, Cyclic ratchetting and failure of a pearlitic rail steel, Fatigue & Fracture of Engineering Materials & Structures 23(9), 747–758, 2000

# 11. Appendix I
# Results from FE simulations of the voestalpine test rig

## 11.1 Animations

Animations of the evolution of von Mises stress, contact pressures and equivalent plastic strain, are uploaded to the INNOTRACK KMS. The movies contain insets with rail part and rail cross section. Node 1165 of the rail part, which is located 56 mm from the gauge side, is marked for reference.

## 11.2 Contour plots

The figures are identified with an identification tag C*x* – S*y* – i*z*. Here *x*, *y* and *z* are serial numbers. The identifier C denotes load cycle number. S denoted step, where S1 is the application of the vertical load, S2 the application of the lateral load and S3 wheel movement along the rail. Finally, I denoted the time increment during the solution step. The last increment shown for S1 is always when the total vertical load of 20 tonnes is applied.

## 11.3 Evolution of the von Mises effective stress

In the following figures the distribution of the von Mises (denoted S, Mises) effective stress is shown for the following load cases.

- C1 – S1 – I11
- C2 – S3 – I16
- C2 – S1 – I22
- C2 – S3 – I22
- C3 – S1 – I22
- C3 – S3 – I22
- C4 – S1 – I22
- C4 – S3 – I22

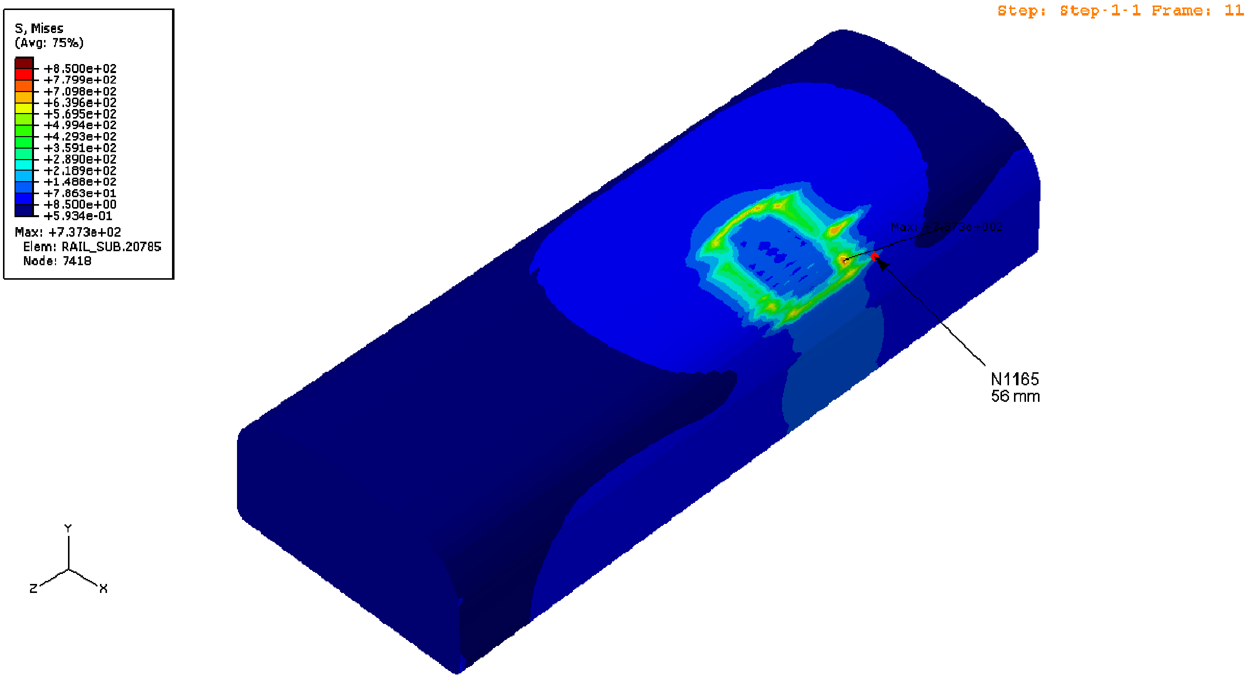
S, Mises
(Avg: 75%)
+8.500e+02
+7.799e+02
+7.098e+02
+6.396e+02
+5.695e+02
+4.994e+02
+4.293e+02
+3.591e+02
+2.890e+02
+2.189e+02
+1.488e+02
+7.863e+01
+8.500e+00
+5.934e-01
Max: +7.373e+02
Elem: RAIL_SUB.20785
Node: 7418
Step: Step-1-1 Frame: 11
Max: +7.373e+002
N1165
56 mm
Y
Z
X

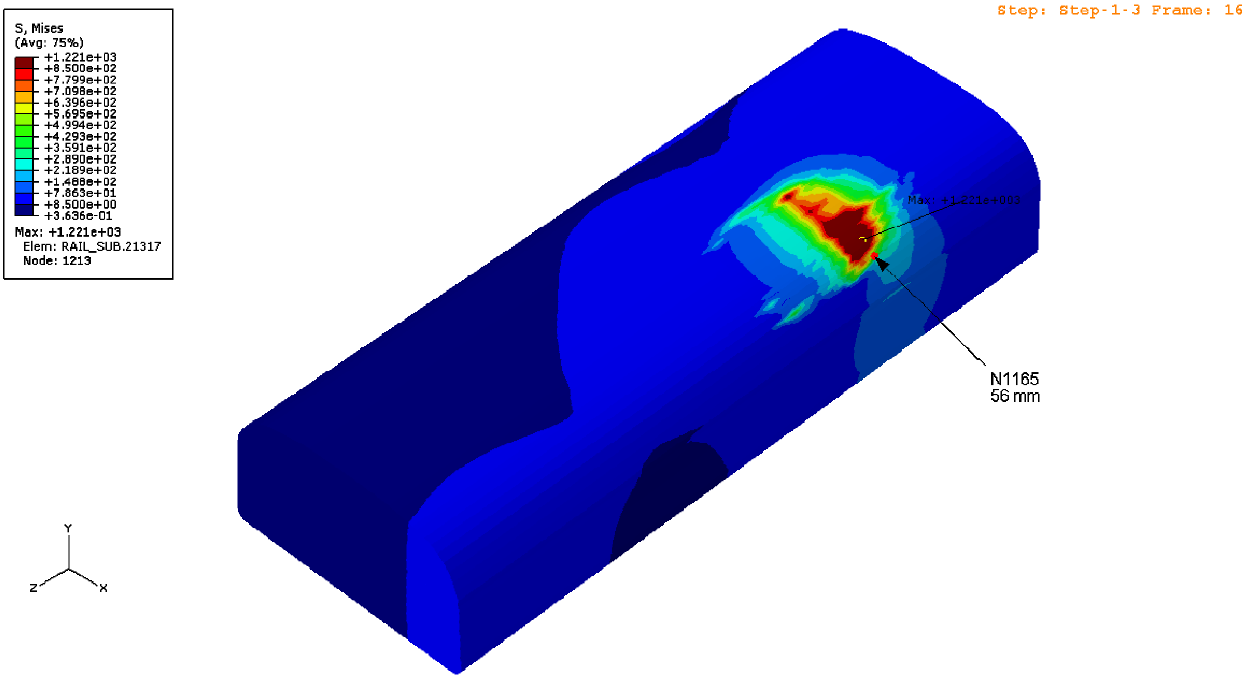
S, Mises
(Avg: 75%)
+1.221e+03
+8.500e+02
+7.799e+02
+7.098e+02
+6.396e+02
+5.695e+02
+4.994e+02
+4.293e+02
+3.591e+02
+2.890e+02
+2.189e+02
+1.488e+02
+7.863e+01
+8.500e+00
+3.636e-01
Max: +1.221e+03
Elem: RAIL_SUB.21317
Node: 1213
Step: Step-1-3 Frame: 16
Max: +1.221e+003
N1165
56 mm
Y
Z
X

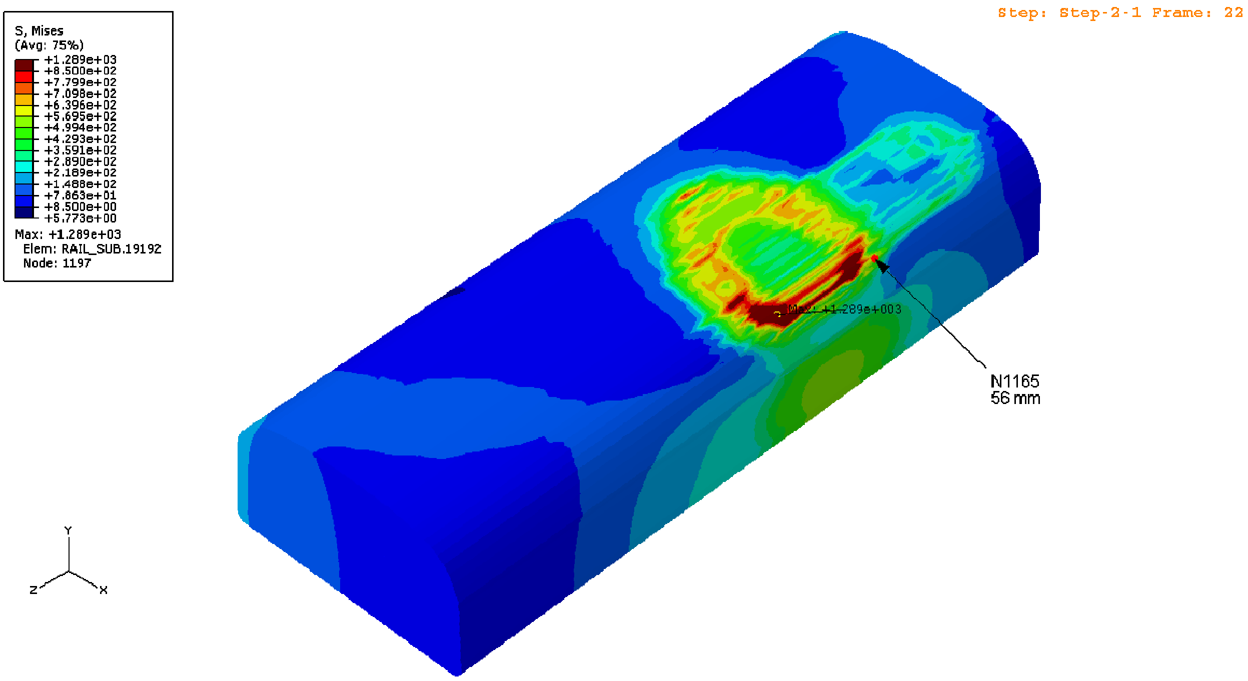
S, Mises
(Avg: 75%)
+1.289e+03
+8.500e+02
+7.799e+02
+7.098e+02
+6.396e+02
+5.695e+02
+4.994e+02
+4.293e+02
+3.591e+02
+2.890e+02
+2.189e+02
+1.488e+02
+7.863e+01
+8.500e+00
+5.773e+00
Max: +1.289e+03
Elem: RAIL_SUB.19192
Node: 1197
Step: Step-2-1 Frame: 22
Max: +1.289e+003
N1165
56 mm
Y
Z
X

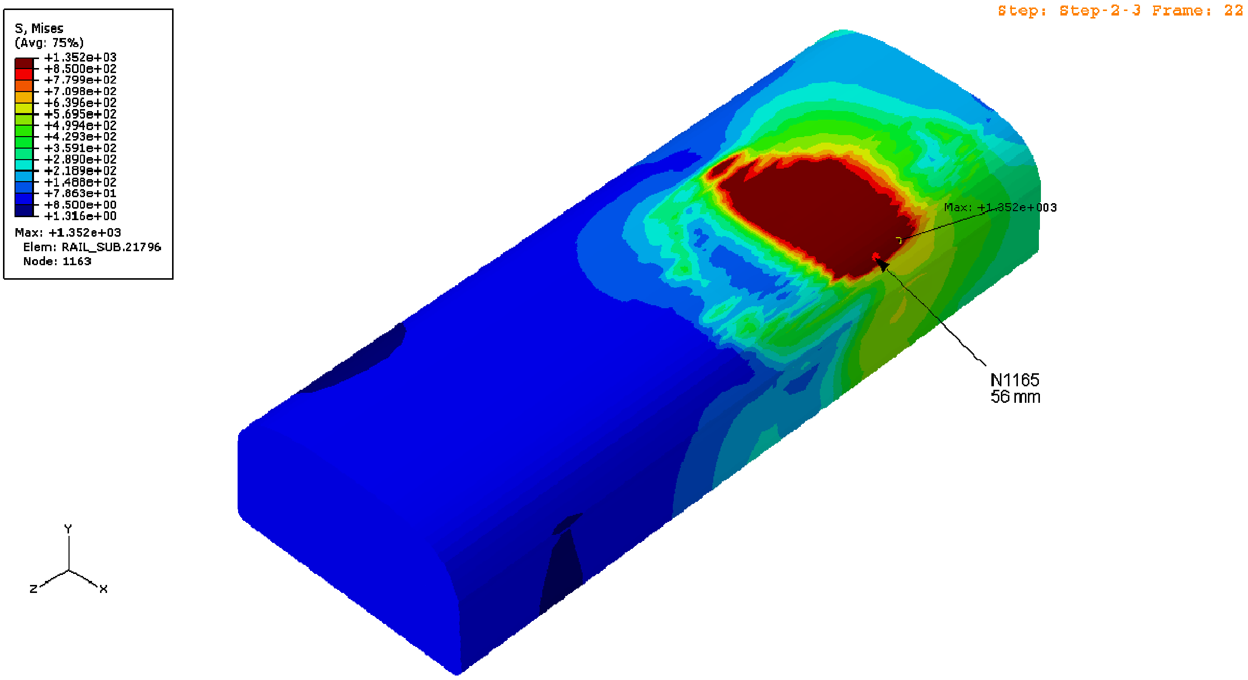
S, Mises
(Avg: 75%)
+1.352e+03
+8.500e+02
+7.799e+02
+7.098e+02
+6.396e+02
+5.695e+02
+4.994e+02
+4.293e+02
+3.591e+02
+2.890e+02
+2.189e+02
+1.488e+02
+7.863e+01
+8.500e+00
+1.316e+00
Max: +1.352e+03
Elem: RAIL_SUB.21796
Node: 1163
Step: Step-2-3 Frame: 22
Max: +1.352e+003
N1165
56 mm
Y
Z
X

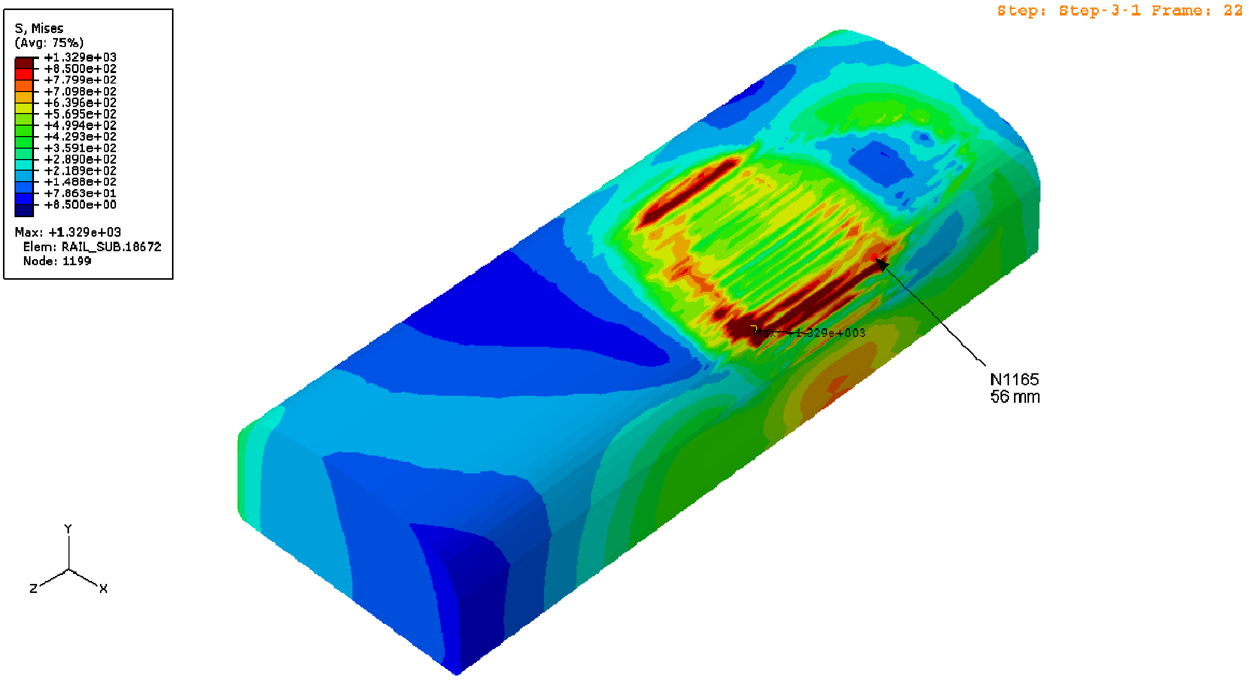
S, Mises
(Avg: 75%)
+1.329e+03
+8.500e+02
+7.799e+02
+7.098e+02
+6.396e+02
+5.695e+02
+4.994e+02
+4.293e+02
+3.591e+02
+2.890e+02
+2.189e+02
+1.488e+02
+7.863e+01
+8.500e+00
Max: +1.329e+03
Elem: RAIL_SUB.18672
Node: 1199
Step: Step-3-1 Frame: 22
Max: +1.329e+003
N1165
56 mm
Y
Z
X

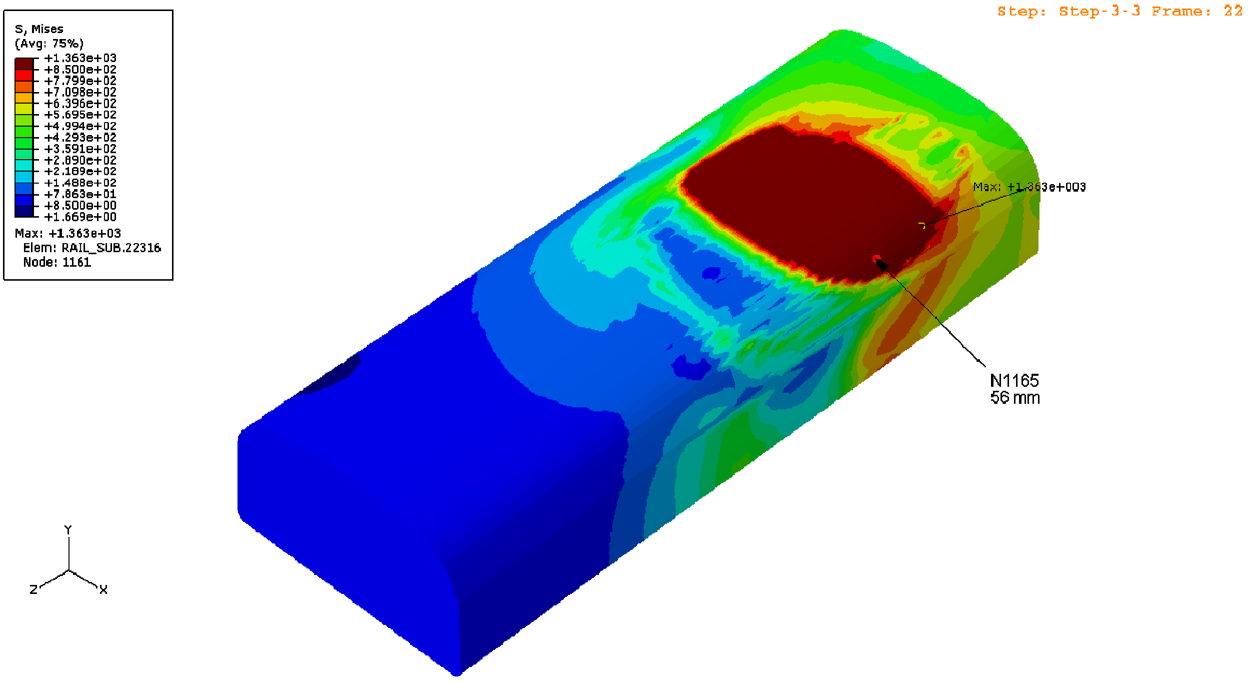
S, Mises
(Avg: 75%)
+1.363e+03
+8.500e+02
+7.799e+02
+7.098e+02
+6.396e+02
+5.695e+02
+4.994e+02
+4.293e+02
+3.591e+02
+2.890e+02
+2.189e+02
+1.488e+02
+7.863e+01
+8.500e+00
+1.669e+00
Max: +1.363e+03
Elem: RAIL_SUB.22316
Node: 1161
Step: Step-3-3 Frame: 22
Max: +1.363e+003
N1165
56 mm
Y
Z
X

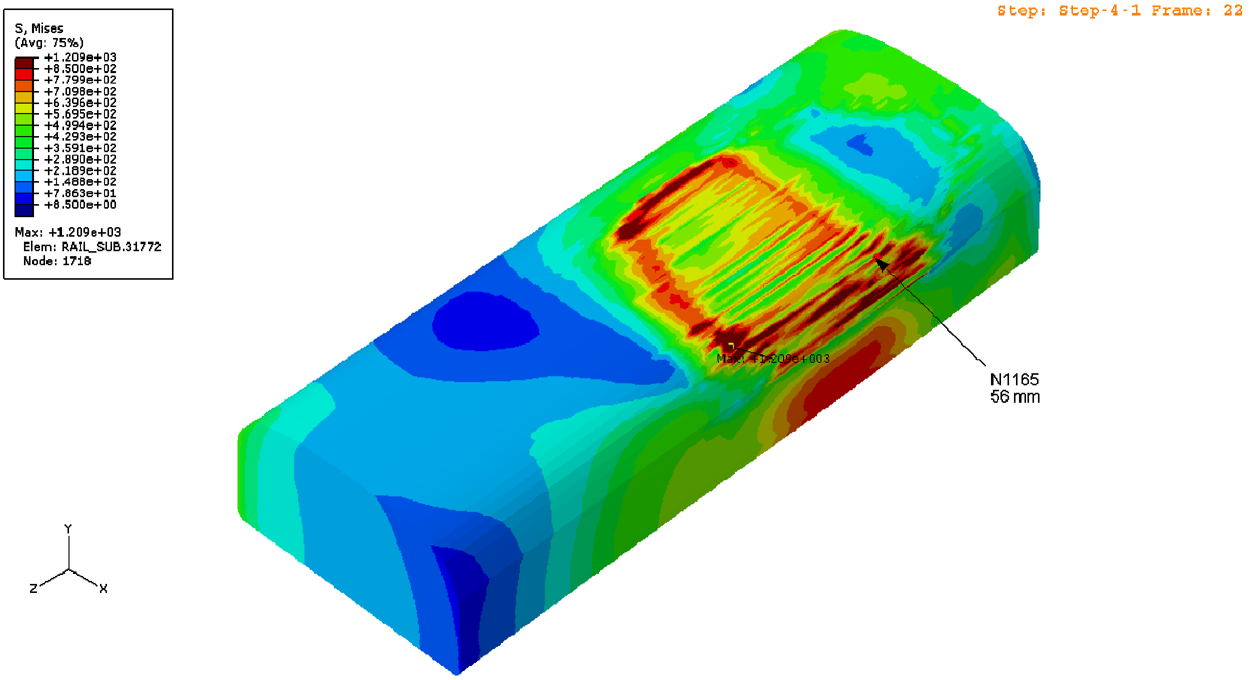
S, Mises
(Avg: 75%)
+1.209e+03
+8.500e+02
+7.799e+02
+7.098e+02
+6.396e+02
+5.695e+02
+4.994e+02
+4.293e+02
+3.591e+02
+2.890e+02
+2.189e+02
+1.488e+02
+7.863e+01
+8.500e+00
Max: +1.209e+03
Elem: RAIL_SUB.31772
Node: 1718
Step: Step-4-1 Frame: 22
Max: +1.209e+003
N1165
56 mm
Y
Z
X

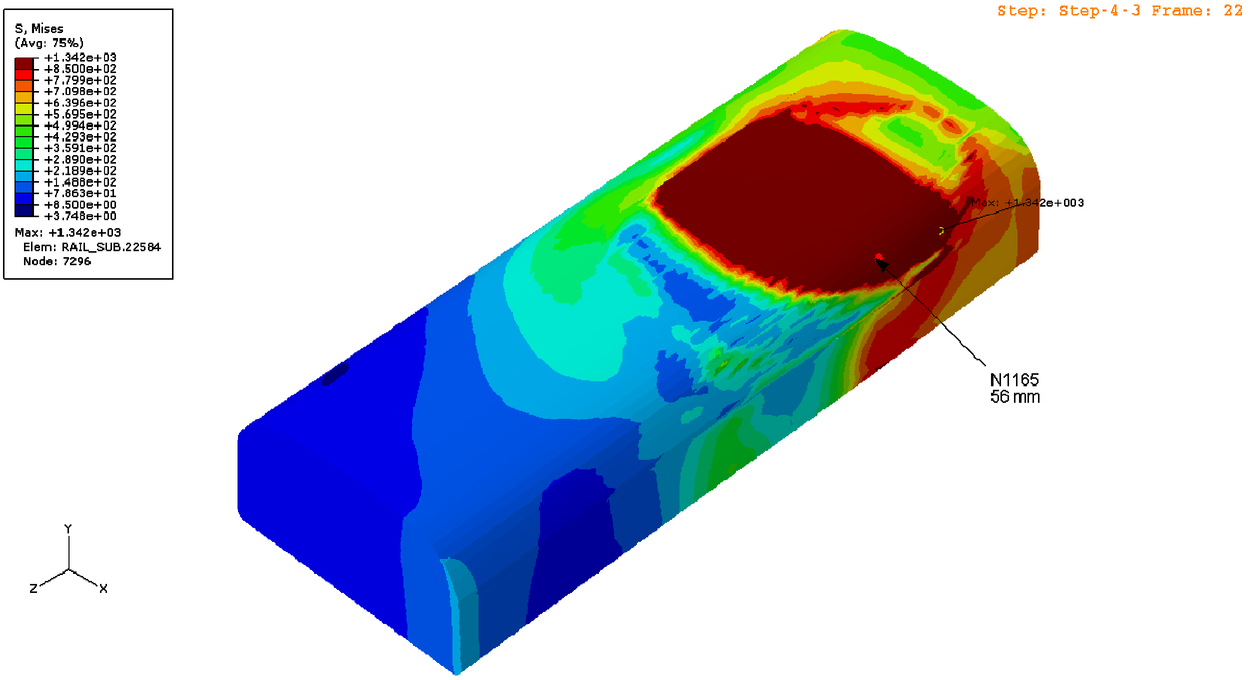
S, Mises
(Avg: 75%)
+1.342e+03
+8.500e+02
+7.799e+02
+7.098e+02
+6.396e+02
+5.695e+02
+4.994e+02
+4.293e+02
+3.591e+02
+2.890e+02
+2.189e+02
+1.488e+02
+7.863e+01
+8.500e+00
+3.748e+00
Max: +1.342e+03
Elem: RAIL_SUB.22584
Node: 7296
Step: Step-4-3 Frame: 22
Max: +1.342e+003
N1165
56 mm
Y
Z
X

## 11.4 Evolution of the contact pressure

In the following figures the distribution of the contact pressure (denoted CPRESS is shown for the following load cases.

- C1 – S1 – I11
- C2 – S3 – I16
- C2 – S1 – I22
- C2 – S3 – I22
- C3 – S1 – I22
- C3 – S3 – I22
- C4 – S1 – I22
- C4 – S3 – I22

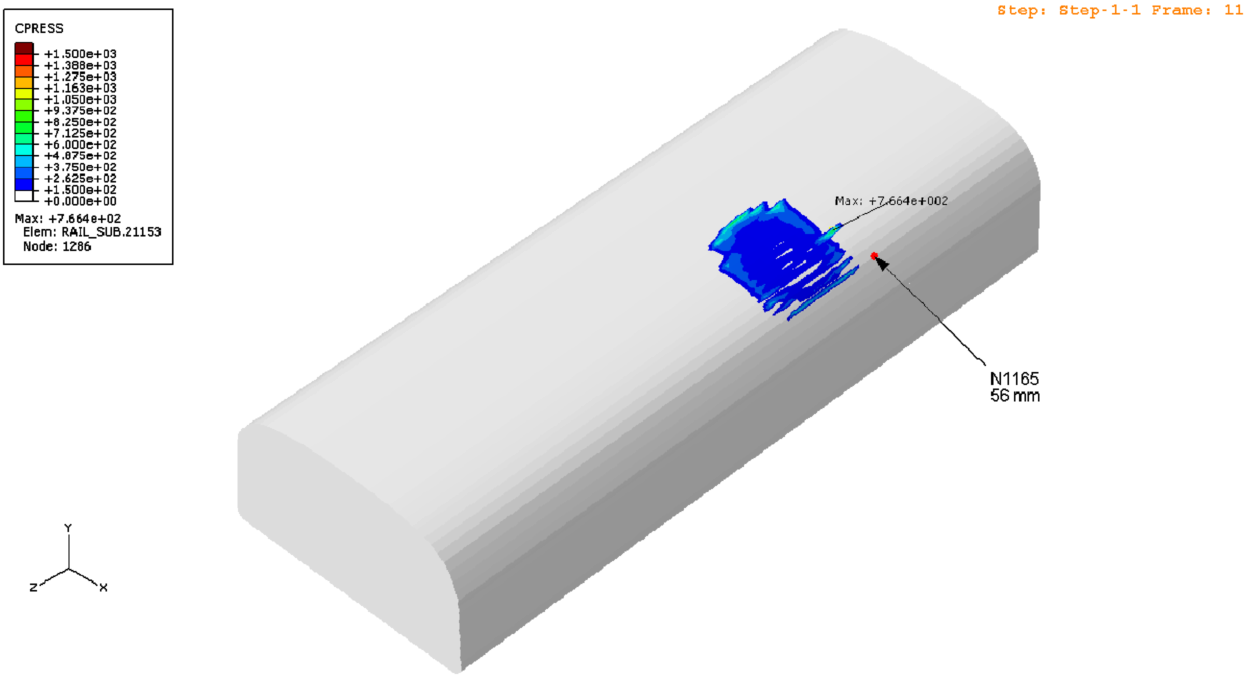
CPRESS
+1.500e+03
+1.388e+03
+1.275e+03
+1.163e+03
+1.050e+03
+9.375e+02
+8.250e+02
+7.125e+02
+6.000e+02
+4.875e+02
+3.750e+02
+2.625e+02
+1.500e+02
+0.000e+00
Max: +7.664e+02
Elem: RAIL_SUB.21153
Node: 1286
Step: Step-1-1 Frame: 11
Max: +7.664e+002
N1165
56 mm
Y
Z
X

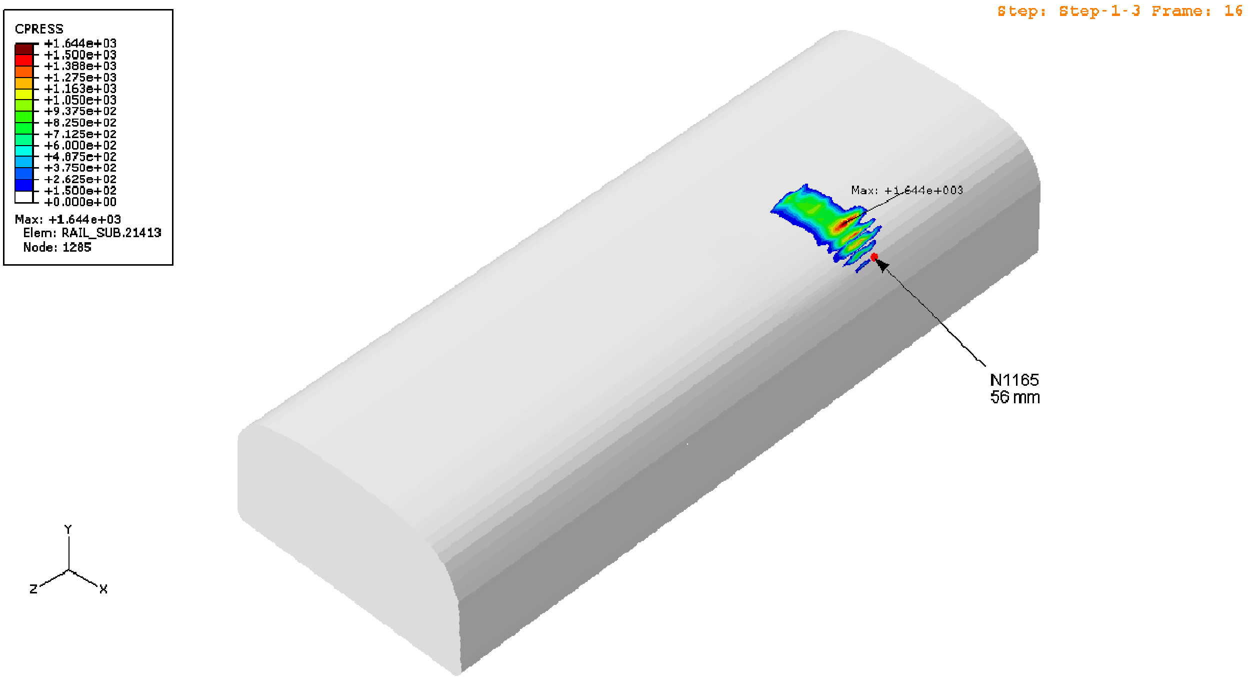
CPRESS
+1.644e+03
+1.500e+03
+1.388e+03
+1.275e+03
+1.163e+03
+1.050e+03
+9.375e+02
+8.250e+02
+7.125e+02
+6.000e+02
+4.875e+02
+3.750e+02
+2.625e+02
+1.500e+02
+0.000e+00
Max: +1.644e+03
Elem: RAIL_SUB.21413
Node: 1285
Step: Step-1-3 Frame: 16
Max: +1.644e+003
N1165
56 mm
Y
Z
X

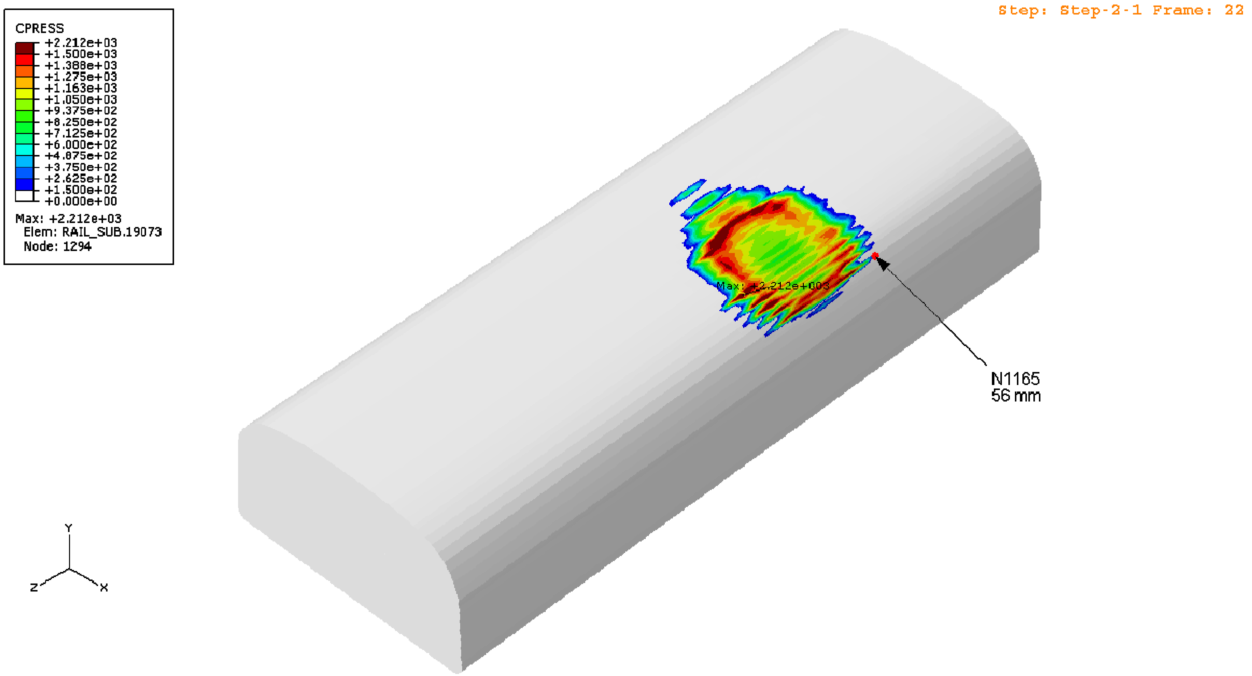
CPRESS
+2.212e+03
+1.500e+03
+1.388e+03
+1.275e+03
+1.163e+03
+1.050e+03
+9.375e+02
+8.250e+02
+7.125e+02
+6.000e+02
+4.875e+02
+3.750e+02
+2.625e+02
+1.500e+02
+0.000e+00
Max: +2.212e+03
Elem: RAIL_SUB.19073
Node: 1294
Step: Step-2-1 Frame: 22
Max: +2.212e+003
N1165
56 mm
Y
Z
X

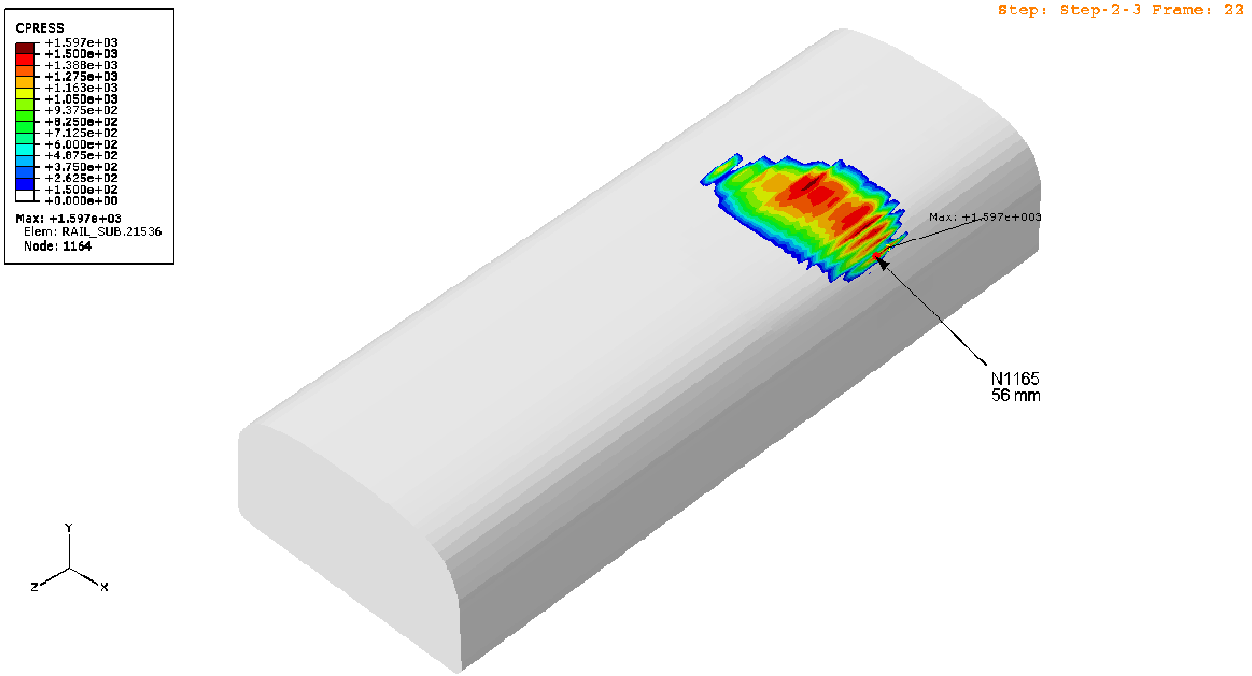
CPRESS
+1.597e+03
+1.500e+03
+1.388e+03
+1.275e+03
+1.163e+03
+1.050e+03
+9.375e+02
+8.250e+02
+7.125e+02
+6.000e+02
+4.875e+02
+3.750e+02
+2.625e+02
+1.500e+02
+0.000e+00
Max: +1.597e+03
Elem: RAIL_SUB.21536
Node: 1164
Step: Step-2-3 Frame: 22
Max: +1.597e+003
N1165
56 mm
Y
Z
X

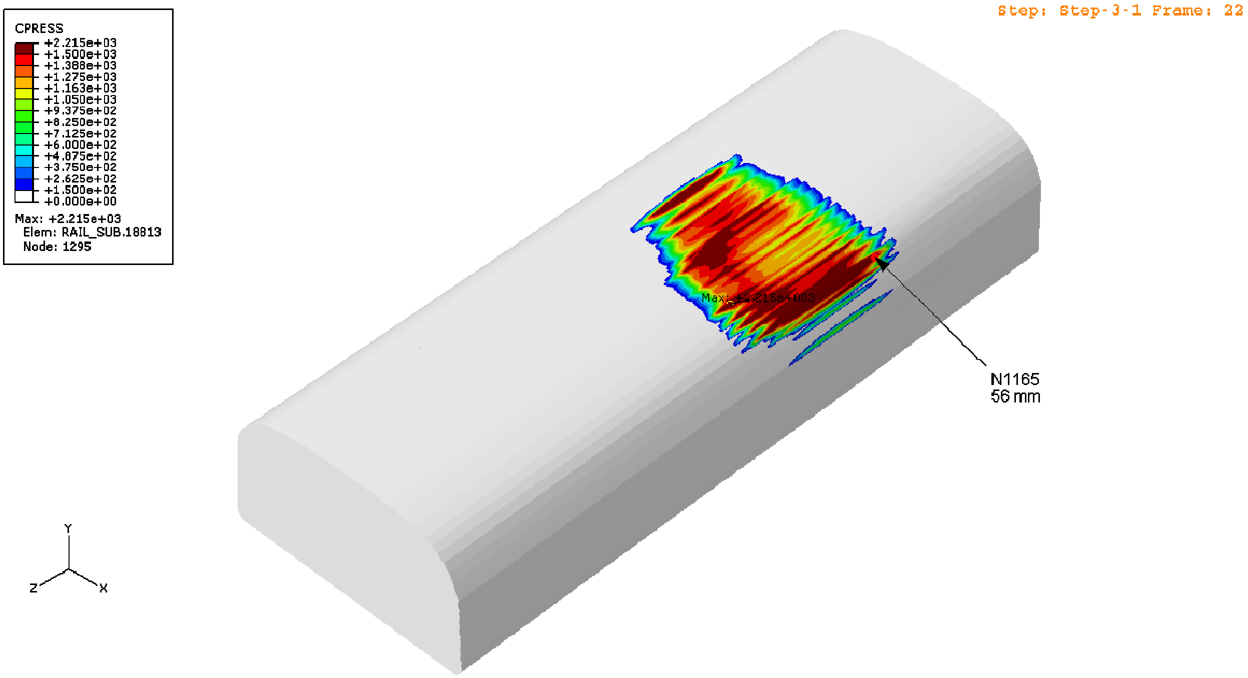
CPRESS
+2.215e+03
+1.500e+03
+1.388e+03
+1.275e+03
+1.163e+03
+1.050e+03
+9.375e+02
+8.250e+02
+7.125e+02
+6.000e+02
+4.875e+02
+3.750e+02
+2.625e+02
+1.500e+02
+0.000e+00
Max: +2.215e+03
Elem: RAIL_SUB.18813
Node: 1295
Step: Step-3-1 Frame: 22
Max: +2.215e+003
N1165
56 mm
Y
Z
X

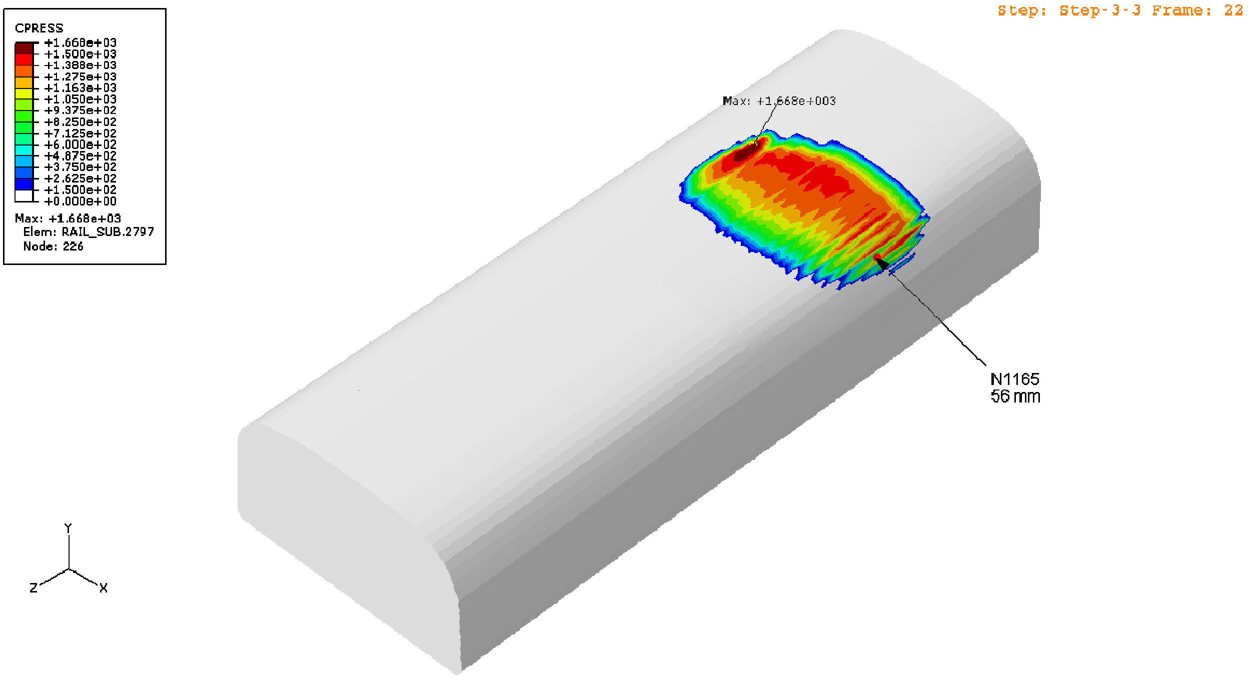
CPRESS
+1.668e+03
+1.500e+03
+1.388e+03
+1.275e+03
+1.163e+03
+1.050e+03
+9.375e+02
+8.250e+02
+7.125e+02
+6.000e+02
+4.875e+02
+3.750e+02
+2.625e+02
+1.500e+02
+0.000e+00
Max: +1.668e+03
Elem: RAIL_SUB.2797
Node: 226
Step: Step-3-3 Frame: 22
Max: +1.668e+003
N1165
56 mm
Y
Z
X

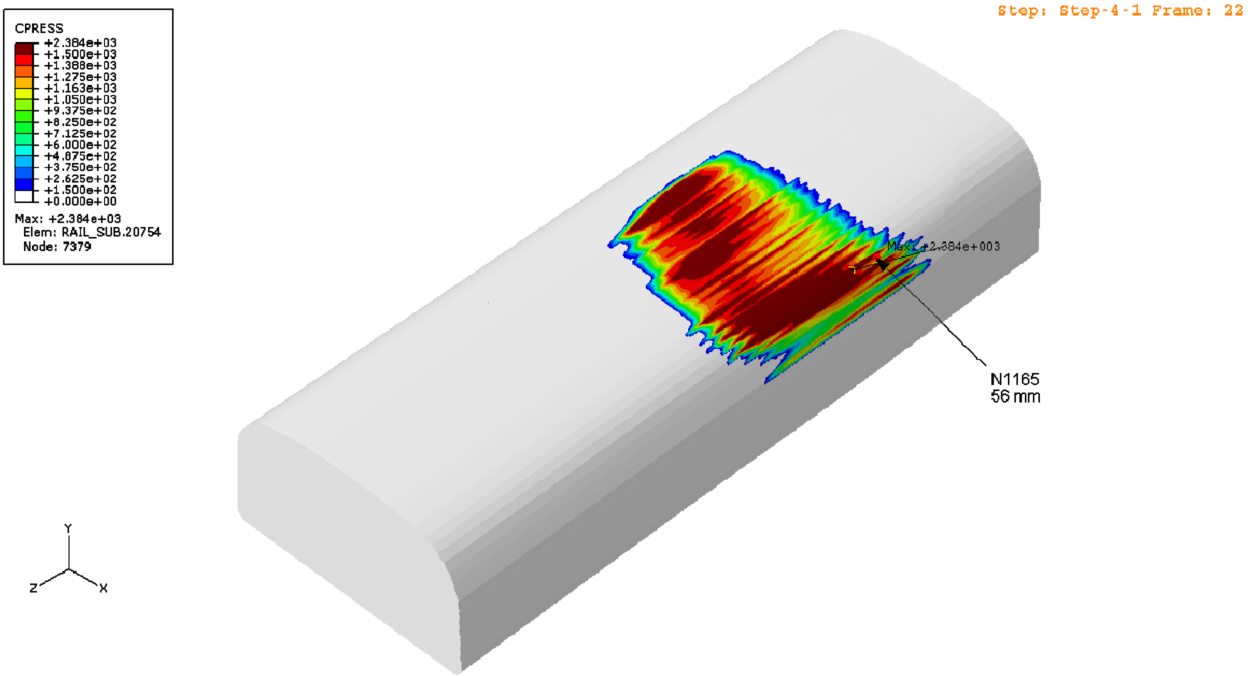
CPRESS
+2.384e+03
+1.500e+03
+1.388e+03
+1.275e+03
+1.163e+03
+1.050e+03
+9.375e+02
+8.250e+02
+7.125e+02
+6.000e+02
+4.875e+02
+3.750e+02
+2.625e+02
+1.500e+02
+0.000e+00
Max: +2.384e+03
Elem: RAIL_SUB.20754
Node: 7379
Step: Step-4-1 Frame: 22
Max: +2.384e+003
N1165
56 mm
Y
Z
X

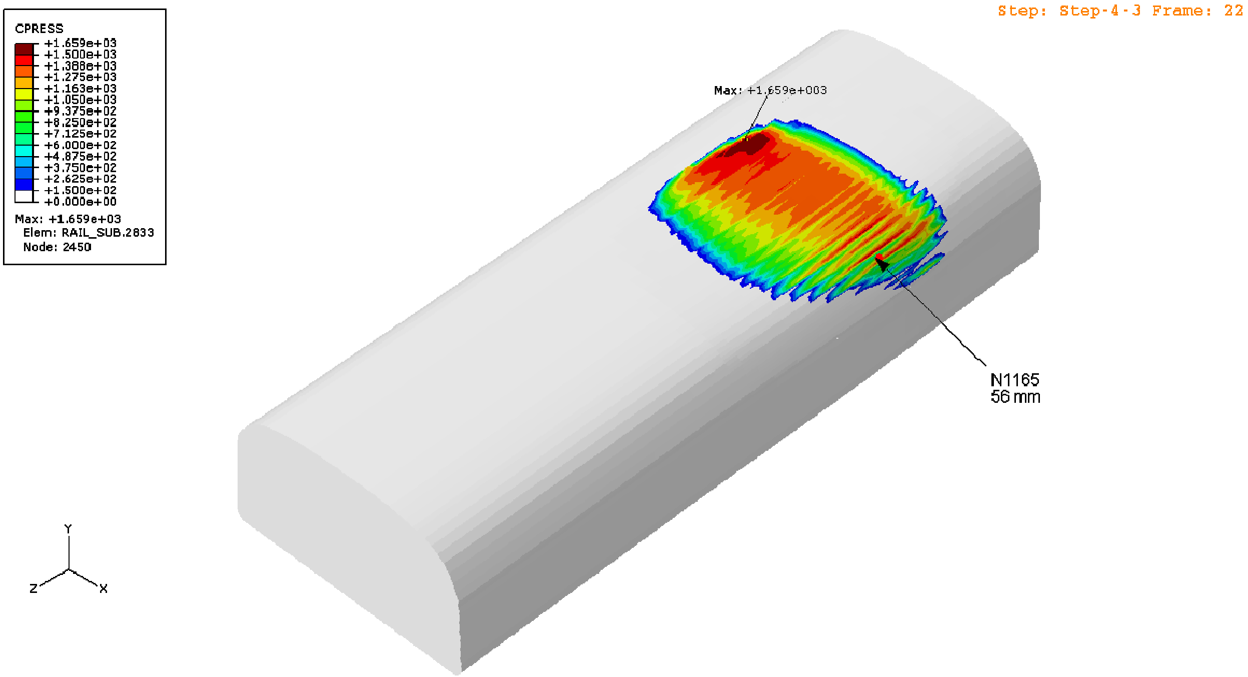
CPRESS
+1.659e+03
+1.500e+03
+1.388e+03
+1.275e+03
+1.163e+03
+1.050e+03
+9.375e+02
+8.250e+02
+7.125e+02
+6.000e+02
+4.875e+02
+3.750e+02
+2.625e+02
+1.500e+02
+0.000e+00
Max: +1.659e+03
Elem: RAIL_SUB.2833
Node: 2450
Step: Step-4-3 Frame: 22
Max: +1.659e+003
N1165
56 mm
Y
Z
X

## 11.5 Evolution of the vertical stress component

In the following figures the distribution of the vertical stress component, i.e. the normal stress in the *y*-direction (denoted S22) is shown for the following load cases.

- C1 – S1 – i11
- C2 – S3 – i16
- C2 – S1 – i22
- C2 – S3 – i22
- C3 – S1 – i22
- C3 – S3 – i22
- C4 – S1 – i22
- C4 – S3 – i22

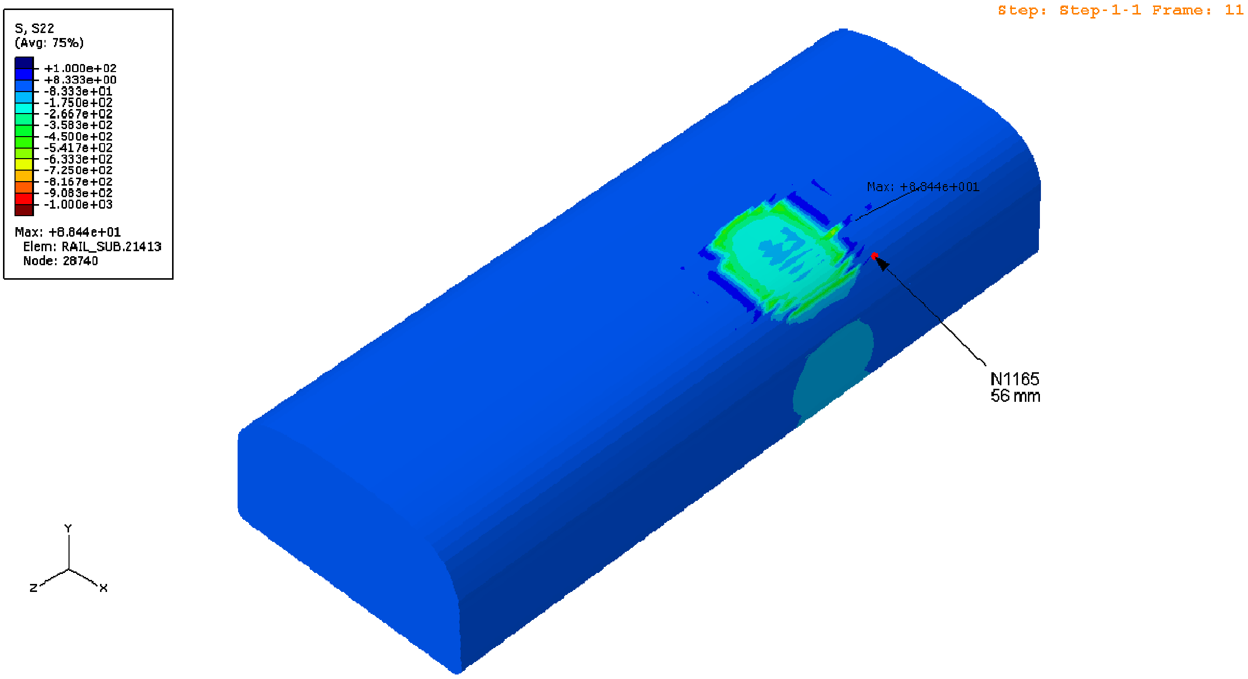
S, S22
(Avg: 75%)
+1.000e+02
+8.333e+00
-8.333e+01
-1.750e+02
-2.667e+02
-3.583e+02
-4.500e+02
-5.417e+02
-6.333e+02
-7.250e+02
-8.167e+02
-9.083e+02
-1.000e+03
Max: +8.844e+01
Elem: RAIL_SUB.21413
Node: 28740
Step: Step-1-1 Frame: 11
Max: +8.844e+001
N1165
56 mm
Y
Z
X

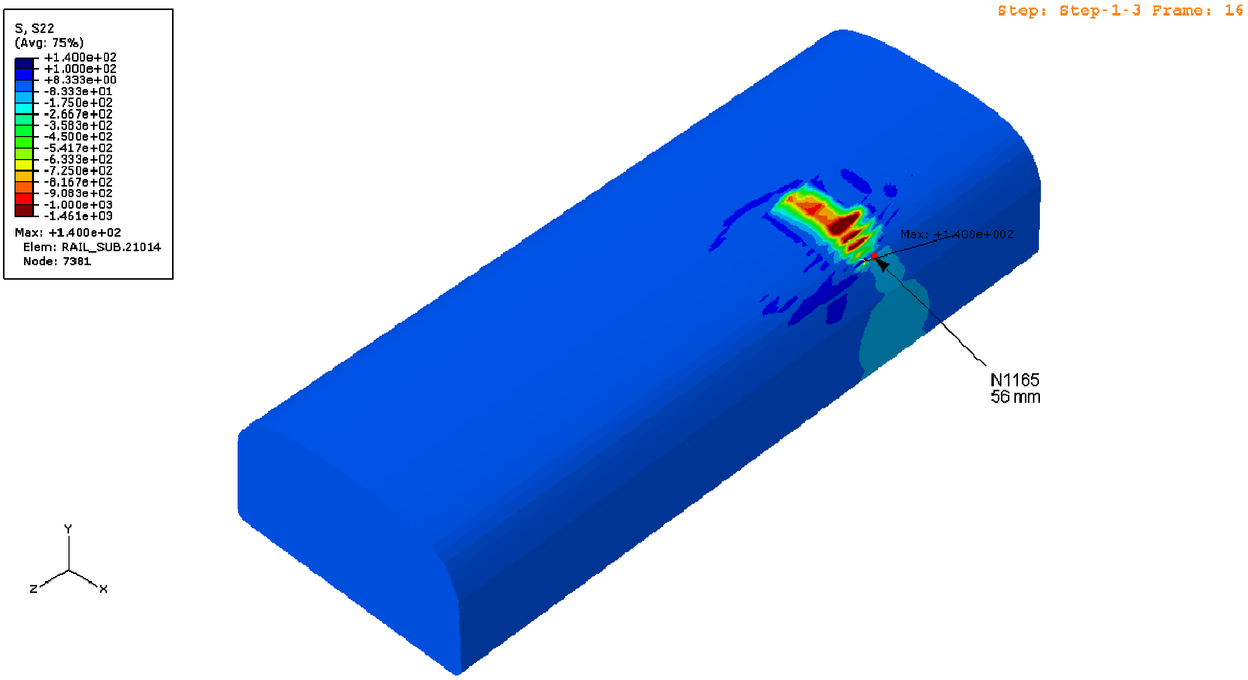
S, S22
(Avg: 75%)
+1.400e+02
+1.000e+02
+8.333e+00
-8.333e+01
-1.750e+02
-2.667e+02
-3.583e+02
-4.500e+02
-5.417e+02
-6.333e+02
-7.250e+02
-8.167e+02
-9.083e+02
-1.000e+03
-1.461e+03
Max: +1.400e+02
Elem: RAIL_SUB.21014
Node: 7381
Step: Step-1-3 Frame: 16
Max: +1.400e+002
N1165
56 mm
Y
Z
X

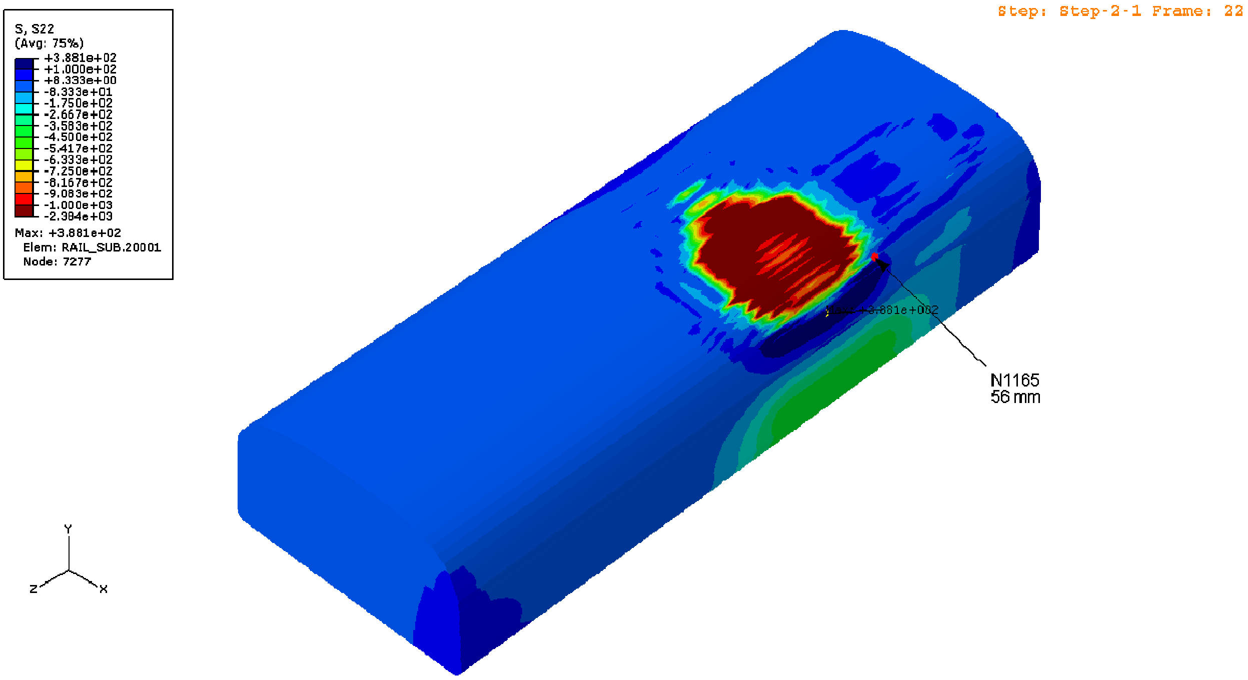
S, S22
(Avg: 75%)
+3.881e+02
+1.000e+02
+8.333e+00
-8.333e+01
-1.750e+02
-2.667e+02
-3.583e+02
-4.500e+02
-5.417e+02
-6.333e+02
-7.250e+02
-8.167e+02
-9.083e+02
-1.000e+03
-2.384e+03
Max: +3.881e+02
Elem: RAIL_SUB.20001
Node: 7277
Step: Step-2-1 Frame: 22
+3.881e+002
N1165
56 mm
Y
Z
X

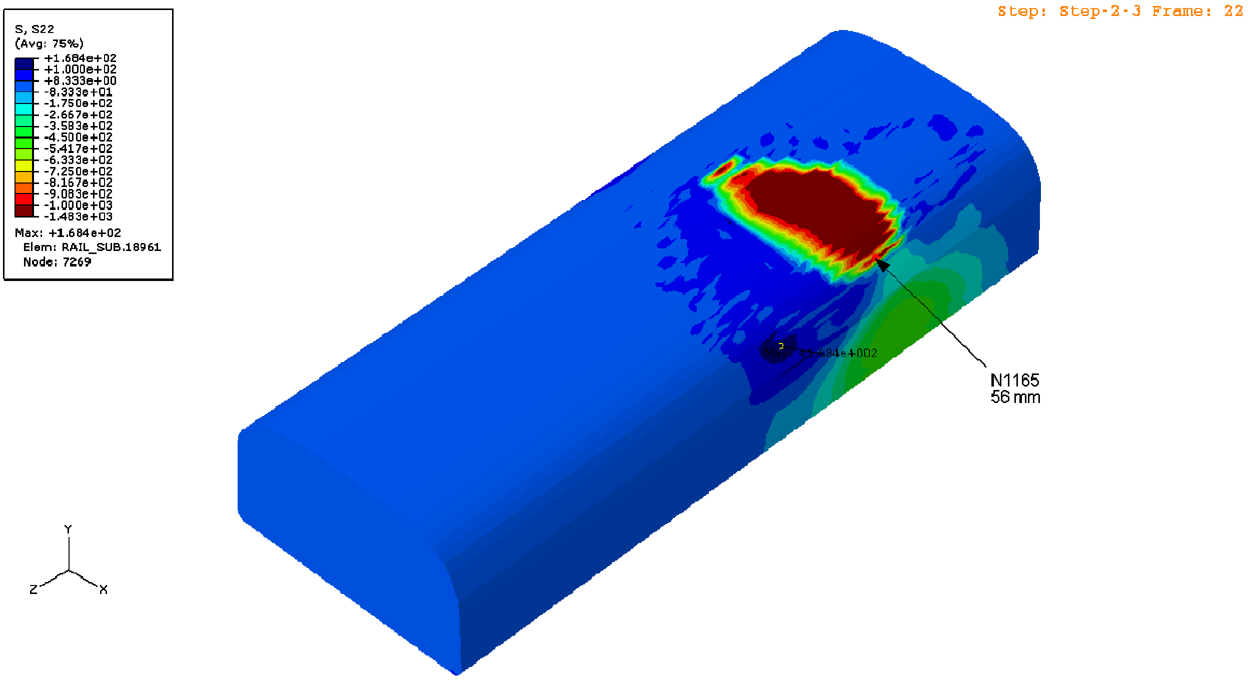
S, S22
(Avg: 75%)
+1.684e+02
+1.000e+02
+8.333e+00
-8.333e+01
-1.750e+02
-2.667e+02
-3.583e+02
-4.500e+02
-5.417e+02
-6.333e+02
-7.250e+02
-8.167e+02
-9.083e+02
-1.000e+03
-1.483e+03
Max: +1.684e+02
Elem: RAIL_SUB.18961
Node: 7269
Step: Step-2-3 Frame: 22
+1.684e+002
N1165
56 mm
Y
Z
X

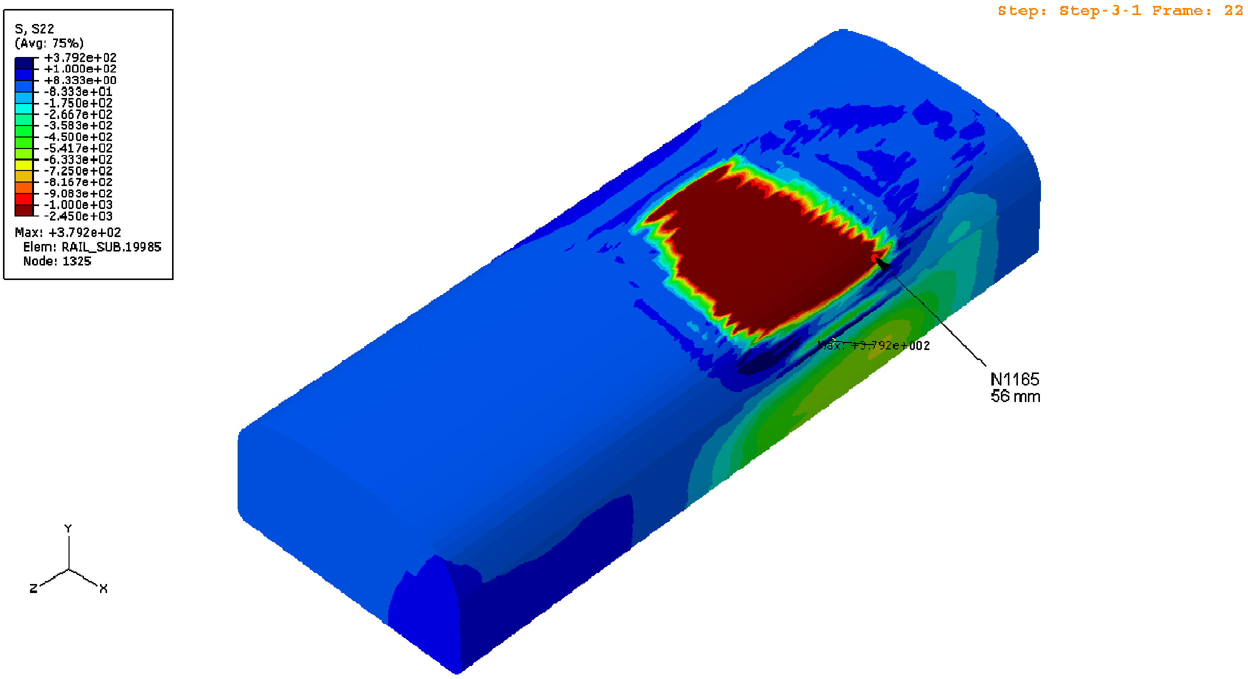
Step: Step-3-1 Frame: 22
S, S22
(Avg: 75%)
+3.792e+02
+1.000e+02
+8.333e+00
-8.333e+01
-1.750e+02
-2.667e+02
-3.583e+02
-4.500e+02
-5.417e+02
-6.333e+02
-7.250e+02
-8.167e+02
-9.083e+02
-1.000e+03
-2.450e+03
Max: +3.792e+02
Elem: RAIL_SUB.19985
Node: 1325
Max: +3.792e+002
N1165
56 mm
Y
Z
X

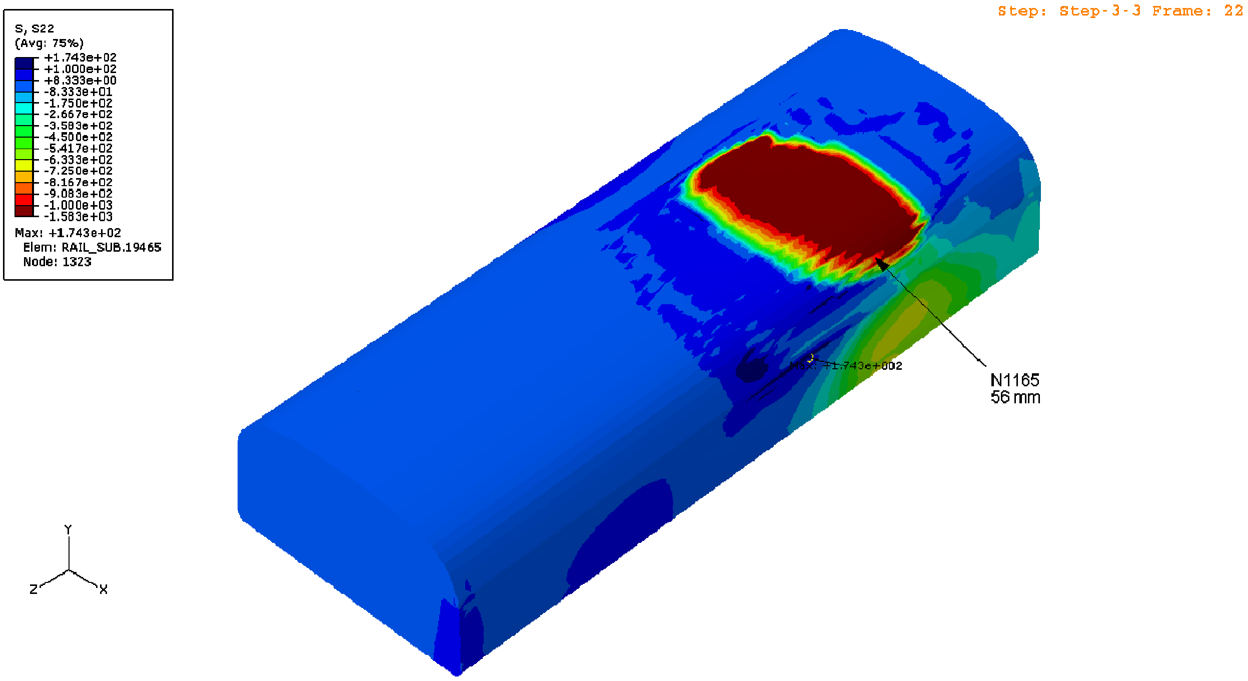
Step: Step-3-3 Frame: 22
S, S22
(Avg: 75%)
+1.743e+02
+1.000e+02
+8.333e+00
-8.333e+01
-1.750e+02
-2.667e+02
-3.583e+02
-4.500e+02
-5.417e+02
-6.333e+02
-7.250e+02
-8.167e+02
-9.083e+02
-1.000e+03
-1.583e+03
Max: +1.743e+02
Elem: RAIL_SUB.19465
Node: 1323
Max: +1.743e+002
N1165
56 mm
Y
Z
X

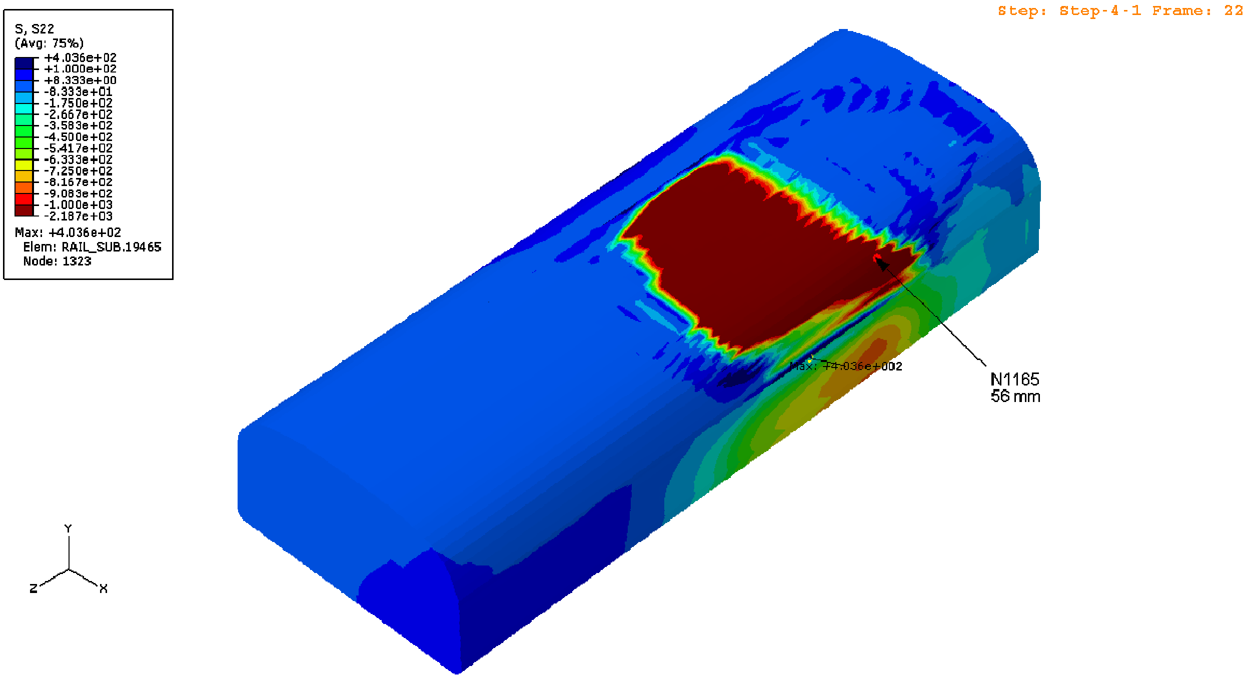
S, S22
(Avg: 75%)
+4.036e+02
+1.000e+02
+8.333e+00
-8.333e+01
-1.750e+02
-2.667e+02
-3.583e+02
-4.500e+02
-5.417e+02
-6.333e+02
-7.250e+02
-8.167e+02
-9.083e+02
-1.000e+03
-2.187e+03
Max: +4.036e+02
Elem: RAIL_SUB.19465
Node: 1323
Step: Step-4-1 Frame: 22
Max: +4.036e+002
N1165
56 mm
Y
Z
X

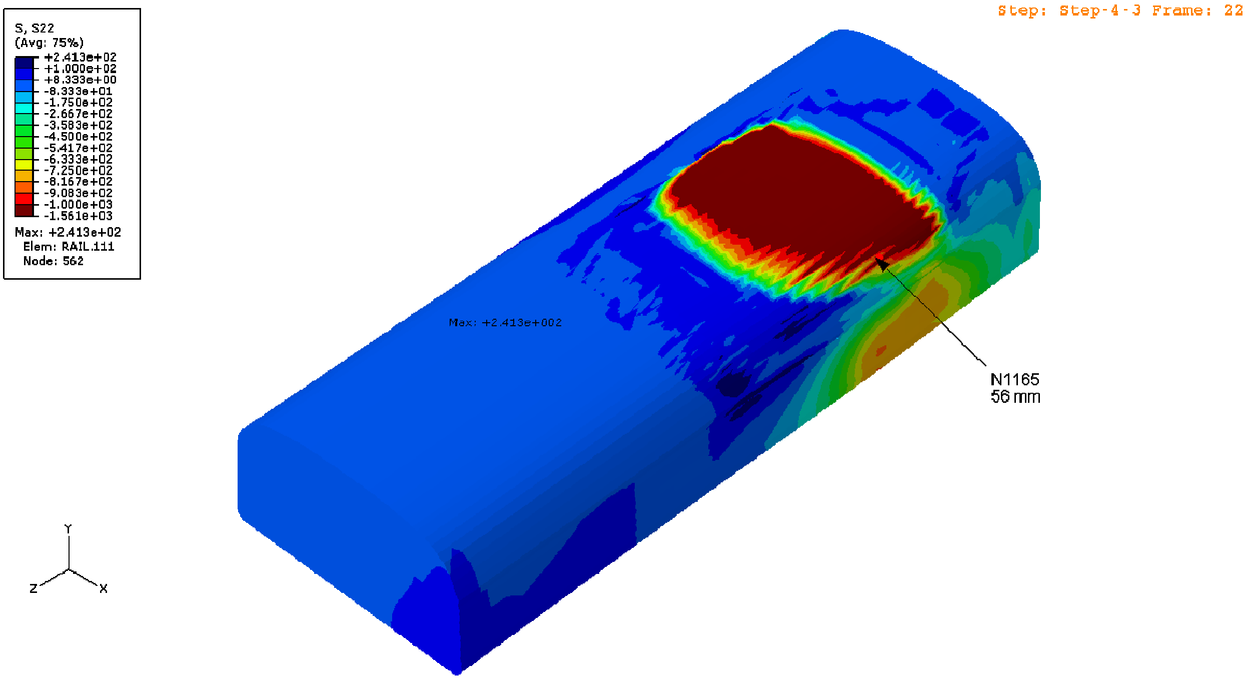
S, S22
(Avg: 75%)
+2.413e+02
+1.000e+02
+8.333e+00
-8.333e+01
-1.750e+02
-2.667e+02
-3.583e+02
-4.500e+02
-5.417e+02
-6.333e+02
-7.250e+02
-8.167e+02
-9.083e+02
-1.000e+03
-1.561e+03
Max: +2.413e+02
Elem: RAIL.111
Node: 562
Step: Step-4-3 Frame: 22
Max: +2.413e+002
N1165
56 mm
Y
Z
X

## 11.6 Evolution of equivalent plastic strain

In the following figures the distribution of the equivalent plastic strain (denoted PEEQ) is shown for the following load cases.

- C1 – S1 – i11
- C2 – S3 – i16
- C2 – S1 – i22
- C2 – S3 – i22
- C3 – S1 – i22
- C3 – S3 – i22
- C4 – S1 – i22
- C4 – S3 – i22

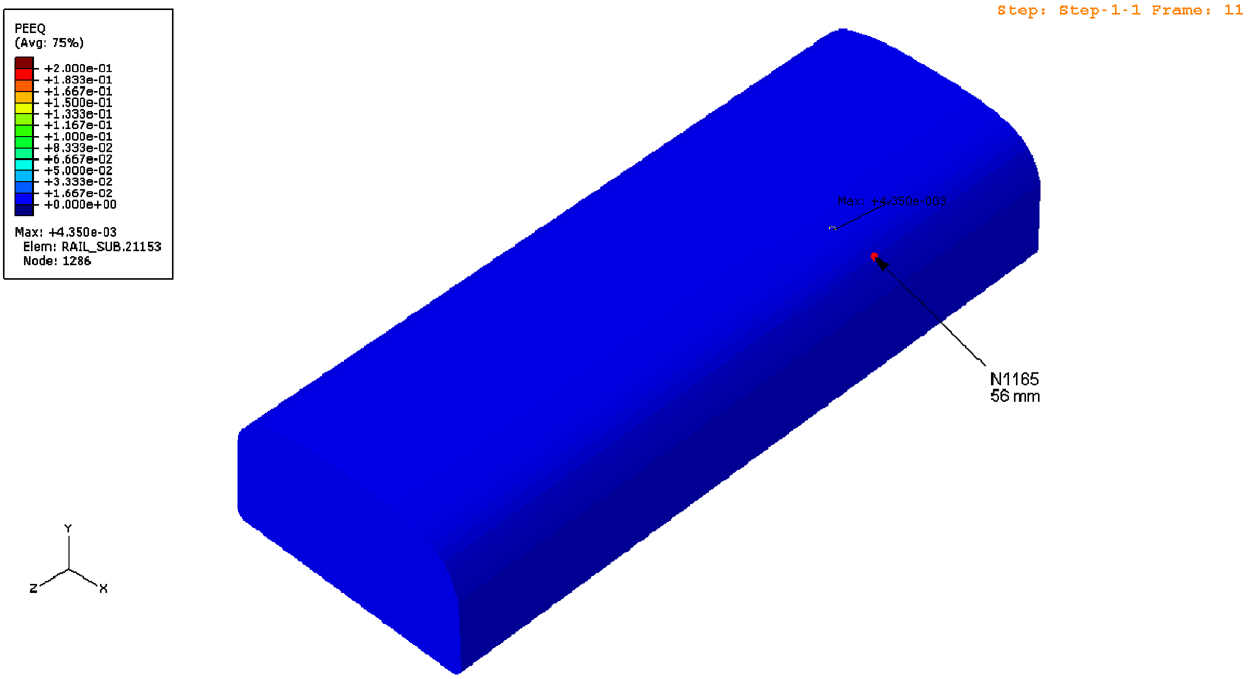
PEEQ
(Avg: 75%)
+2.000e-01
+1.833e-01
+1.667e-01
+1.500e-01
+1.333e-01
+1.167e-01
+1.000e-01
+8.333e-02
+6.667e-02
+5.000e-02
+3.333e-02
+1.667e-02
+0.000e+00
Max: +4.350e-03
Elem: RAIL_SUB.21153
Node: 1286
Step: Step-1-1 Frame: 11
Max: +4.350e-003
N1165
56 mm
Y
Z
X

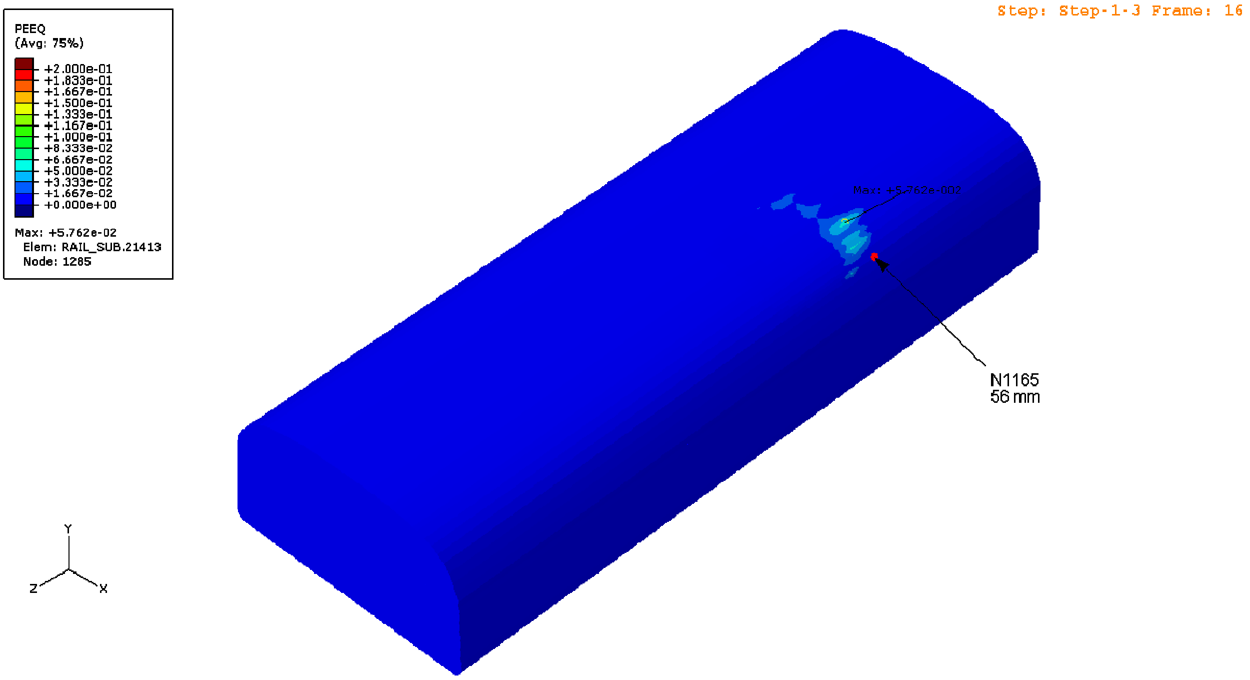
PEEQ
(Avg: 75%)
+2.000e-01
+1.833e-01
+1.667e-01
+1.500e-01
+1.333e-01
+1.167e-01
+1.000e-01
+8.333e-02
+6.667e-02
+5.000e-02
+3.333e-02
+1.667e-02
+0.000e+00
Max: +5.762e-02
Elem: RAIL_SUB.21413
Node: 1285
Step: Step-1-3 Frame: 16
Max: +5.762e-002
N1165
56 mm
Y
Z
X

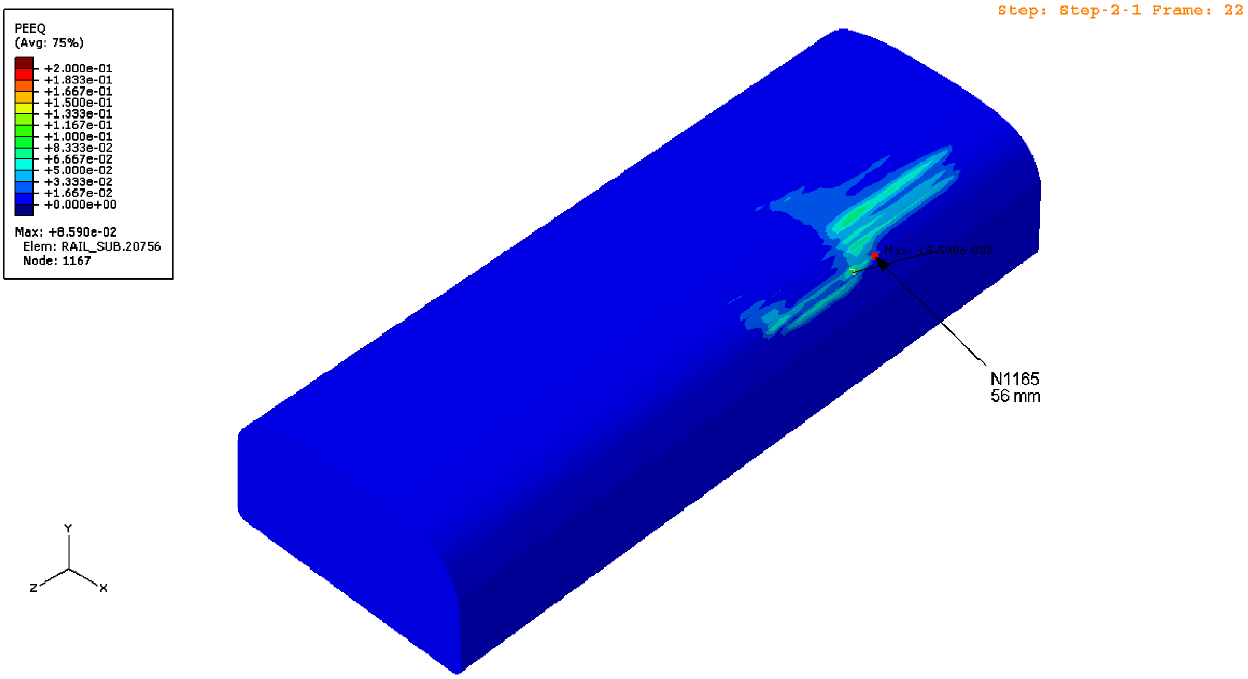
PEEQ
(Avg: 75%)
+2.000e-01
+1.833e-01
+1.667e-01
+1.500e-01
+1.333e-01
+1.167e-01
+1.000e-01
+8.333e-02
+6.667e-02
+5.000e-02
+3.333e-02
+1.667e-02
+0.000e+00
Max: +8.590e-02
Elem: RAIL_SUB.20756
Node: 1167
Step: Step-2-1 Frame: 22
Max: +8.590e-002
N1165
56 mm
Y
Z
X

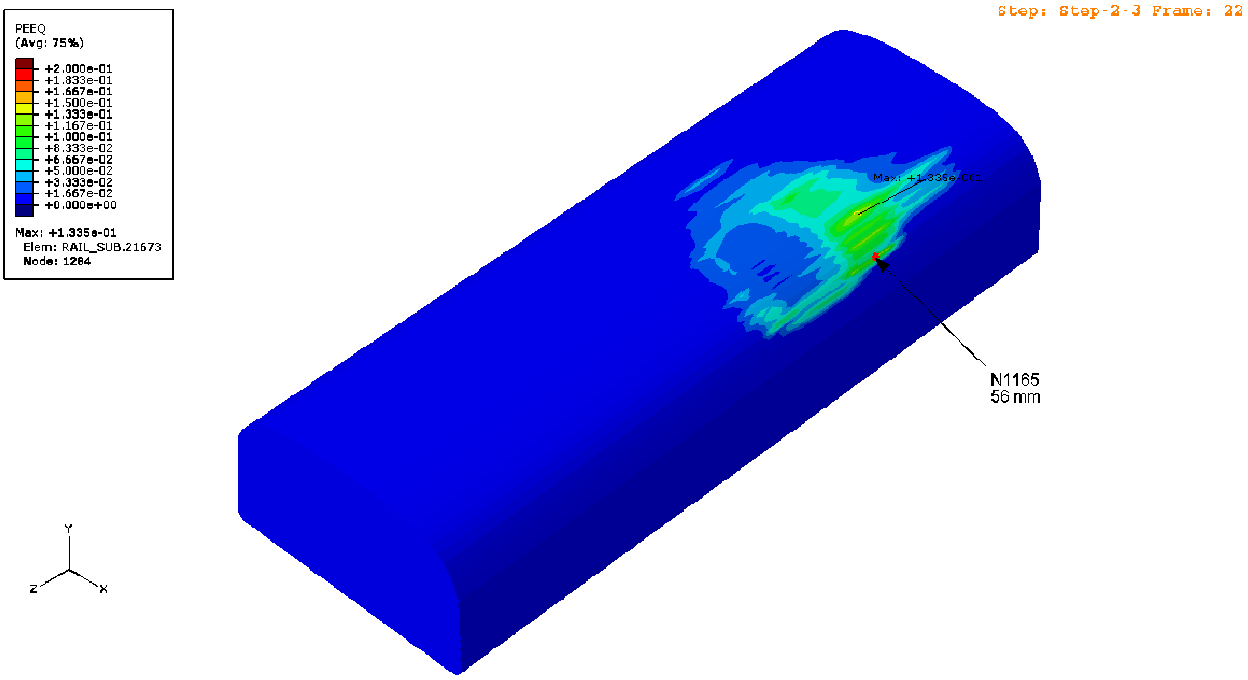
PEEQ
(Avg: 75%)
+2.000e-01
+1.833e-01
+1.667e-01
+1.500e-01
+1.333e-01
+1.167e-01
+1.000e-01
+8.333e-02
+6.667e-02
+5.000e-02
+3.333e-02
+1.667e-02
+0.000e+00
Max: +1.335e-01
Elem: RAIL_SUB.21673
Node: 1284
Step: Step-2-3 Frame: 22
Max: +1.335e-001
N1165
56 mm
Y
Z
X

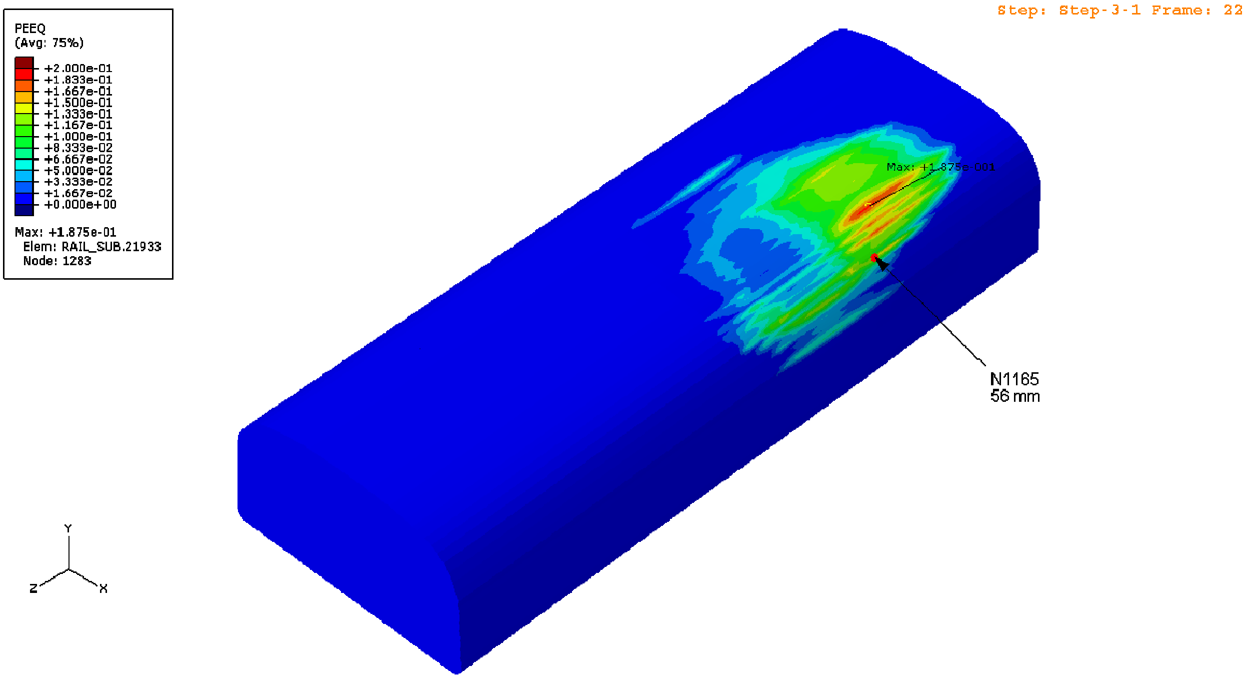
PEEQ
(Avg: 75%)
+2.000e-01
+1.833e-01
+1.667e-01
+1.500e-01
+1.333e-01
+1.167e-01
+1.000e-01
+8.333e-02
+6.667e-02
+5.000e-02
+3.333e-02
+1.667e-02
+0.000e+00
Max: +1.875e-01
Elem: RAIL_SUB.21933
Node: 1283
Step: Step-3-1 Frame: 22
Max: +1.875e-001
N1165
56 mm
Y
Z
X

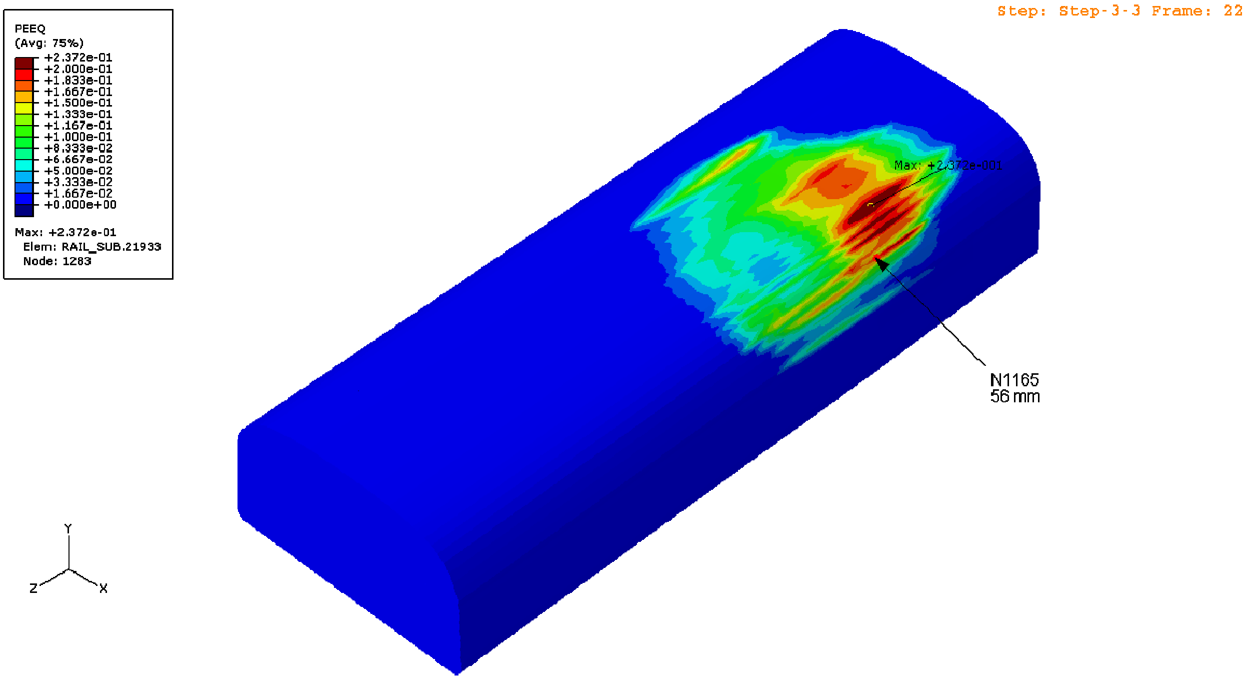
PEEQ
(Avg: 75%)
+2.372e-01
+2.000e-01
+1.833e-01
+1.667e-01
+1.500e-01
+1.333e-01
+1.167e-01
+1.000e-01
+8.333e-02
+6.667e-02
+5.000e-02
+3.333e-02
+1.667e-02
+0.000e+00
Max: +2.372e-01
Elem: RAIL_SUB.21933
Node: 1283
Step: Step-3-3 Frame: 22
Max: +2.372e-001
N1165
56 mm
Y
Z
X

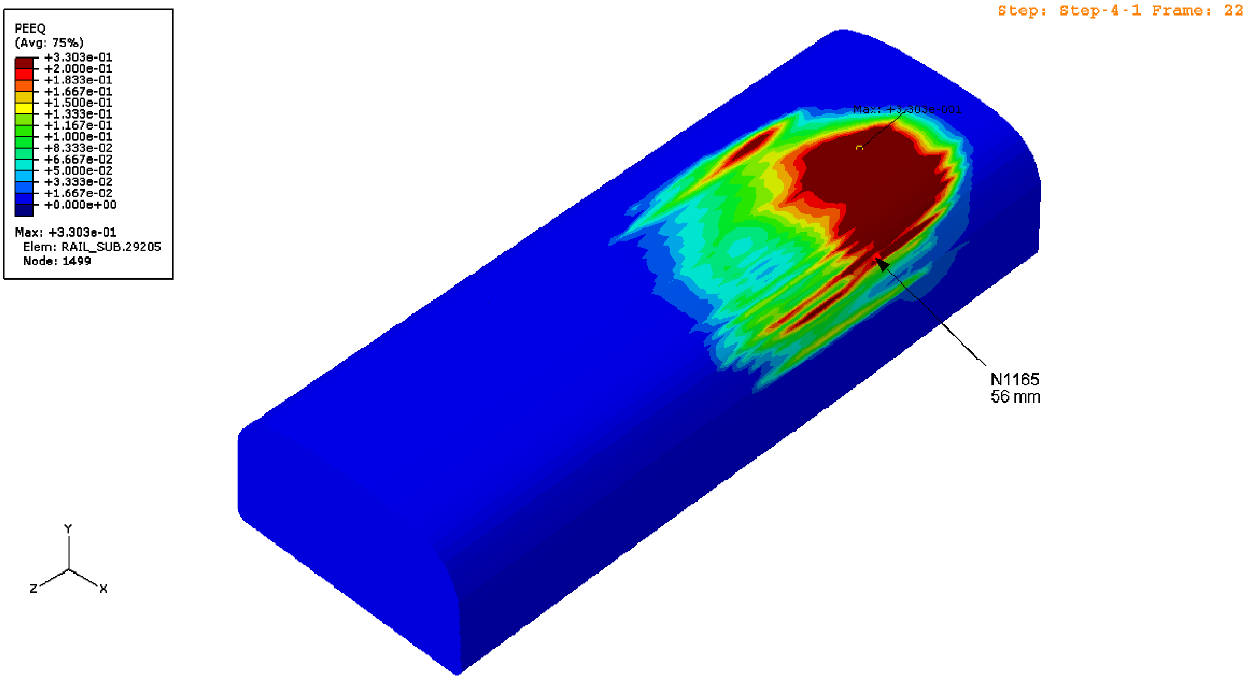
PEEQ
(Avg: 75%)
+3.303e-01
+2.000e-01
+1.833e-01
+1.667e-01
+1.500e-01
+1.333e-01
+1.167e-01
+1.000e-01
+8.333e-02
+6.667e-02
+5.000e-02
+3.333e-02
+1.667e-02
+0.000e+00
Max: +3.303e-01
Elem: RAIL_SUB.29205
Node: 1499
Step: Step-4-1 Frame: 22
Max: +3.303e-01
N1165
56 mm
Y
Z
X

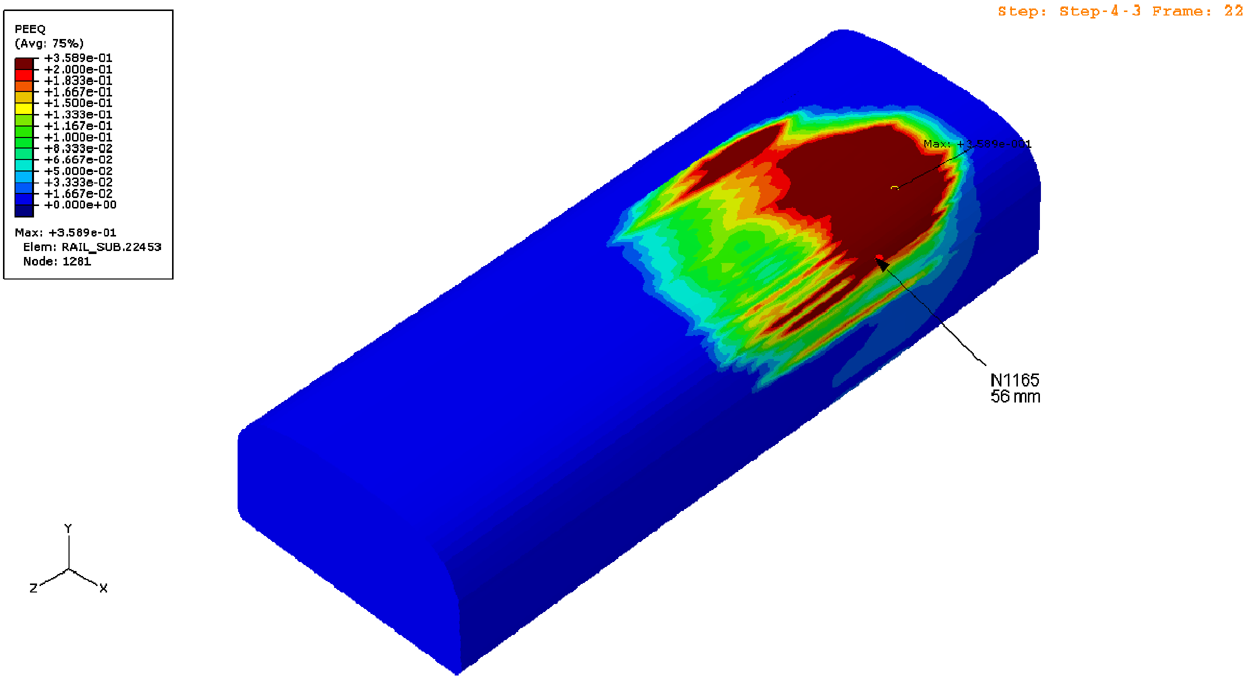
PEEQ
(Avg: 75%)
+3.589e-01
+2.000e-01
+1.833e-01
+1.667e-01
+1.500e-01
+1.333e-01
+1.167e-01
+1.000e-01
+8.333e-02
+6.667e-02
+5.000e-02
+3.333e-02
+1.667e-02
+0.000e+00
Max: +3.589e-01
Elem: RAIL_SUB.22453
Node: 1281
Step: Step-4-3 Frame: 22
Max: +3.589e-01
N1165
56 mm
Y
Z
X

# 12. Appendix II
# Results from FE simulations of the DB test rig C with no lateral load

## 12.1 Animations

Animations of the evolution of von Mises stress, contact pressures and equivalent plastic strain, are uploaded to the INNOTRACK KMS. The movies contain insets with rail part and rail cross section. Node 4431 of the rail part, which is located 131 mm from the gauge side, is marked for reference.

## 12.2 Contour plots

The figures are identified with an identification tag C*x* – S*y* – i*z*. Here *x*, *y* and *z* are serial numbers. The identifier C denotes load cycle number. S denoted step, where S1 is the application of the vertical load, S2 wheel movement along the rail. Finally, I denoted the time increment during the solution step. The last increment shown for S1 is always when the total vertical load of 15 tonnes is applied.

## 12.3 Evolution of the von Mises effective stress

In the following figures the distribution of the von Mises (denoted S, Mises) effective stress is shown for the following load cases.

- C1 – S1 – I11
- C2 – S2 – I20
- C2 – S1 – I11
- C2 – S2 – I23
- C3 – S1 – I11
- C3 – S2 – I23
- C4 – S1 – I11
- C4 – S2 – I28
- C5 – S1 – I11
- C5 – S2 – I26

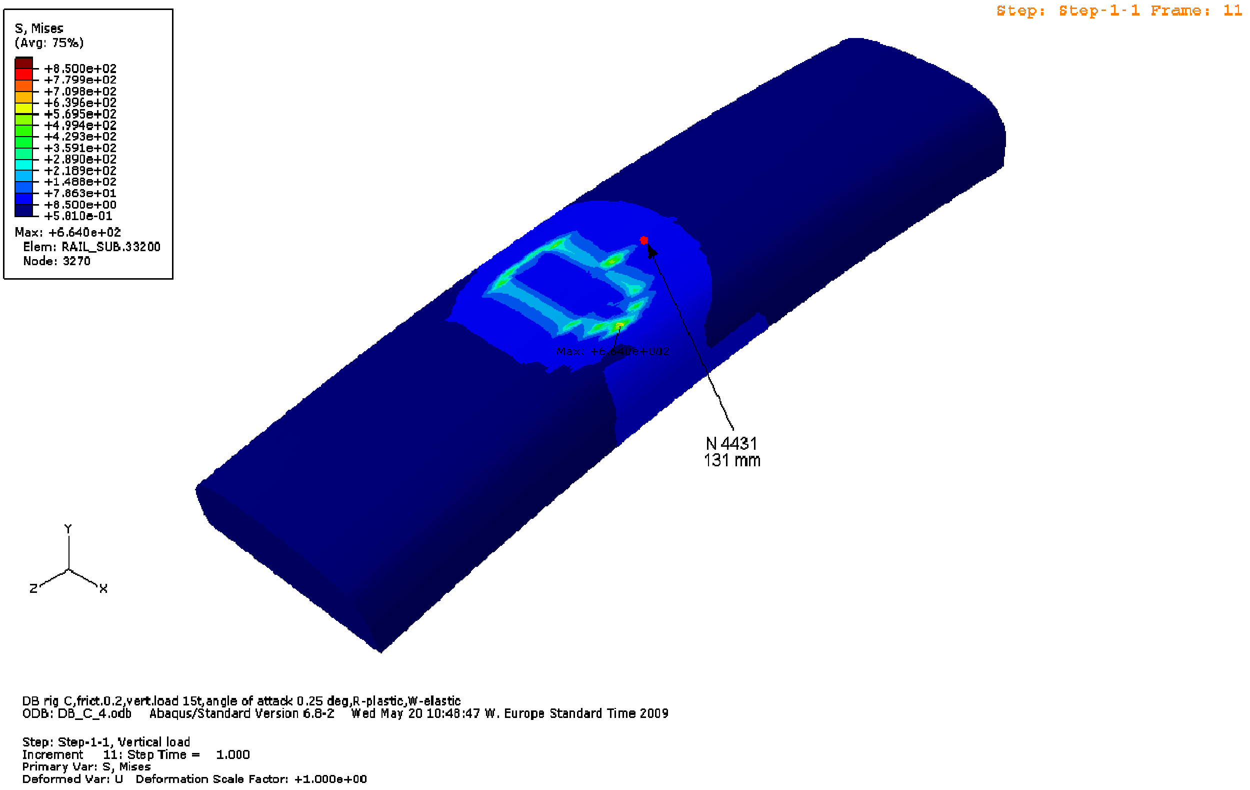
Step: Step-1-1 Frame: 11
S, Mises
(Avg: 75%)
+8.500e+02
+7.799e+02
+7.098e+02
+6.396e+02
+5.695e+02
+4.994e+02
+4.293e+02
+3.591e+02
+2.890e+02
+2.189e+02
+1.488e+02
+7.863e+01
+8.500e+00
+5.810e-01
Max: +6.640e+02
Elem: RAIL_SUB.33200
Node: 3270
Max: +6.640e+002
N 4431
131 mm
Y
Z
X
DB rig C,frict.0.2,vert.load 15t,angle of attack 0.25 deg,R-plastic,W-elastic
ODB: DB_C_4.odb Abaqus/Standard Version 6.8-2 Wed May 20 10:48:47 W. Europe Standard Time 2009
Step: Step-1-1, Vertical load
Increment 11: Step Time = 1.000
Primary Var: S, Mises
Deformed Var: U Deformation Scale Factor: +1.000e+00

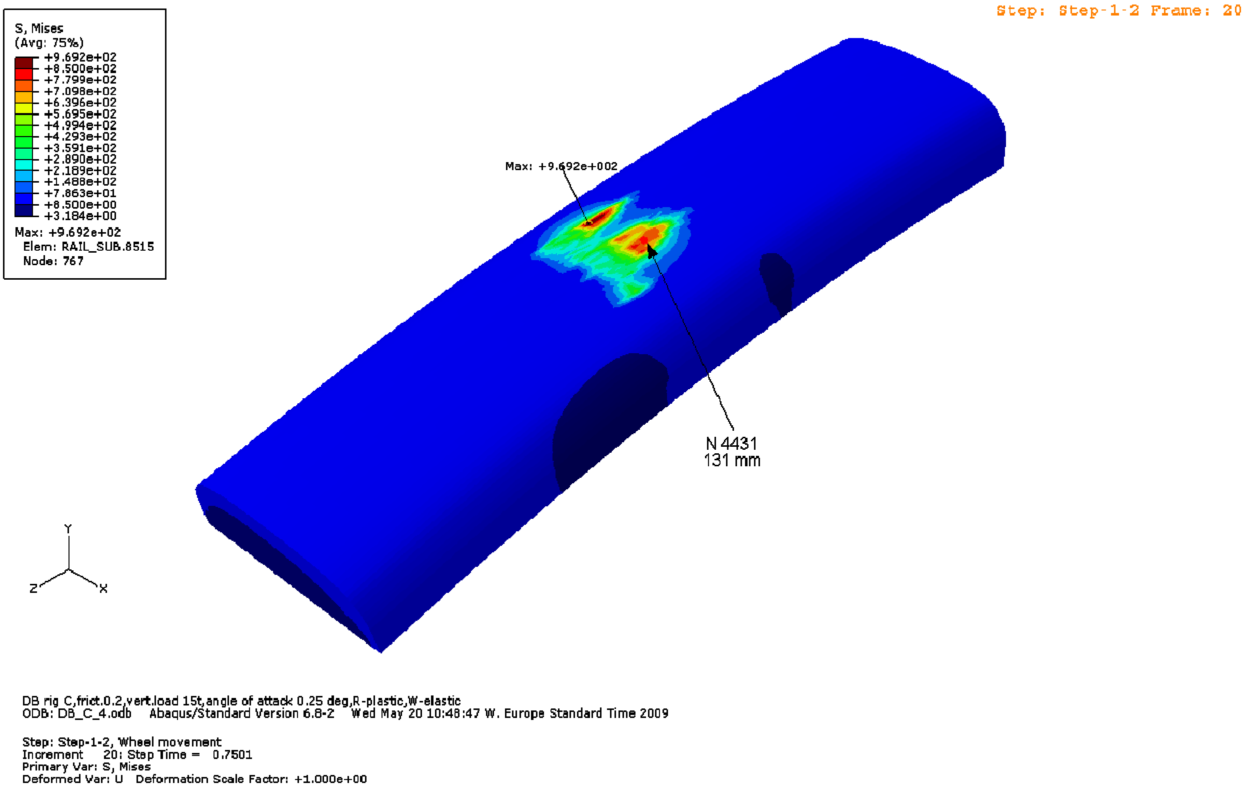
Step: Step-1-2 Frame: 20
S, Mises
(Avg: 75%)
+9.692e+02
+8.500e+02
+7.799e+02
+7.098e+02
+6.396e+02
+5.695e+02
+4.994e+02
+4.293e+02
+3.591e+02
+2.890e+02
+2.189e+02
+1.488e+02
+7.863e+01
+8.500e+00
+3.184e+00
Max: +9.692e+02
Elem: RAIL_SUB.8515
Node: 767
Max: +9.692e+002
N 4431
131 mm
Y
Z
X
DB rig C,frict.0.2,vert.load 15t,angle of attack 0.25 deg,R-plastic,W-elastic
ODB: DB_C_4.odb Abaqus/Standard Version 6.8-2 Wed May 20 10:48:47 W. Europe Standard Time 2009
Step: Step-1-2, Wheel movement
Increment 20: Step Time = 0.7501
Primary Var: S, Mises
Deformed Var: U Deformation Scale Factor: +1.000e+00

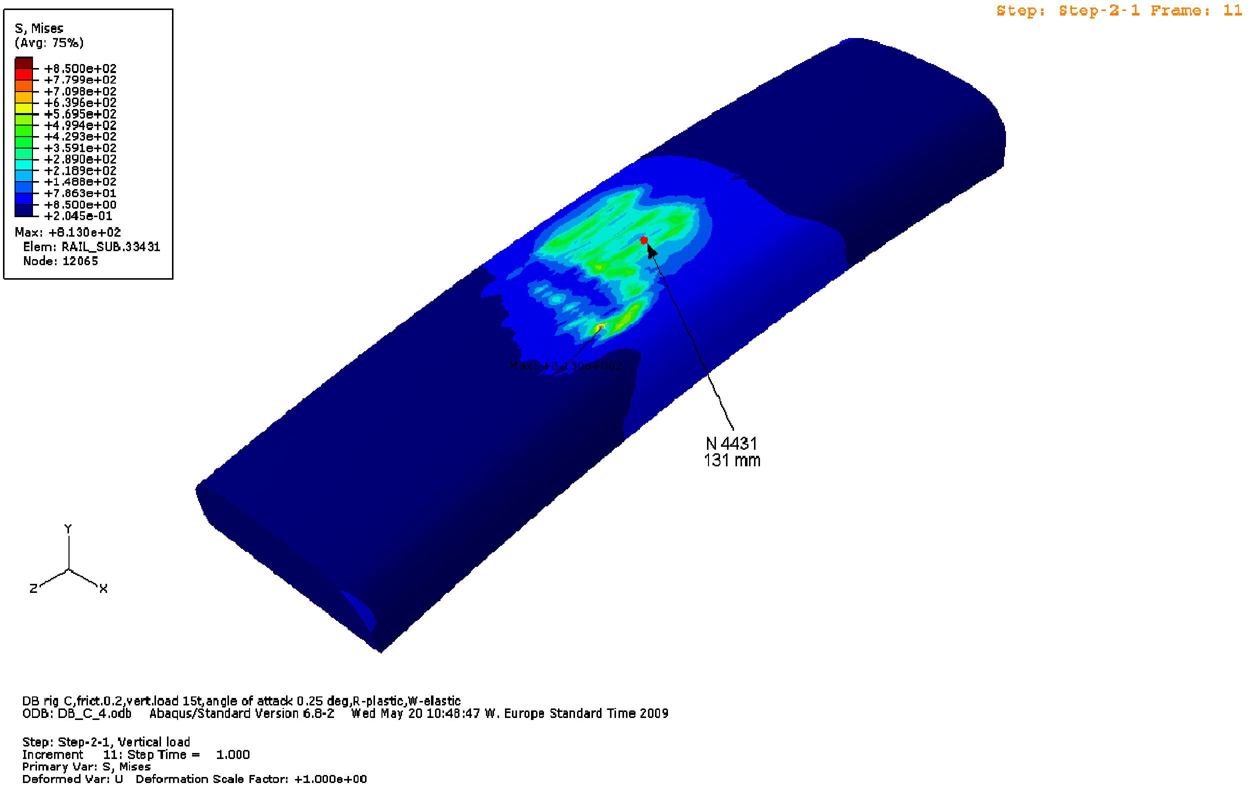
Step: Step-2-1 Frame: 11
S, Mises
(Avg: 75%)
+8.500e+02
+7.799e+02
+7.098e+02
+6.396e+02
+5.695e+02
+4.994e+02
+4.293e+02
+3.591e+02
+2.890e+02
+2.189e+02
+1.488e+02
+7.863e+01
+8.500e+00
+2.045e-01
Max: +8.130e+02
Elem: RAIL_SUB.33431
Node: 12065
N 4431
131 mm
Y
Z
X
DB rig C,frict.0.2,vert.load 15t,angle of attack 0.25 deg,R-plastic,W-elastic
ODB: DB_C_4.odb Abaqus/Standard Version 6.8-2 Wed May 20 10:48:47 W. Europe Standard Time 2009
Step: Step-2-1, Vertical load
Increment 11: Step Time = 1.000
Primary Var: S, Mises
Deformed Var: U Deformation Scale Factor: +1.000e+00

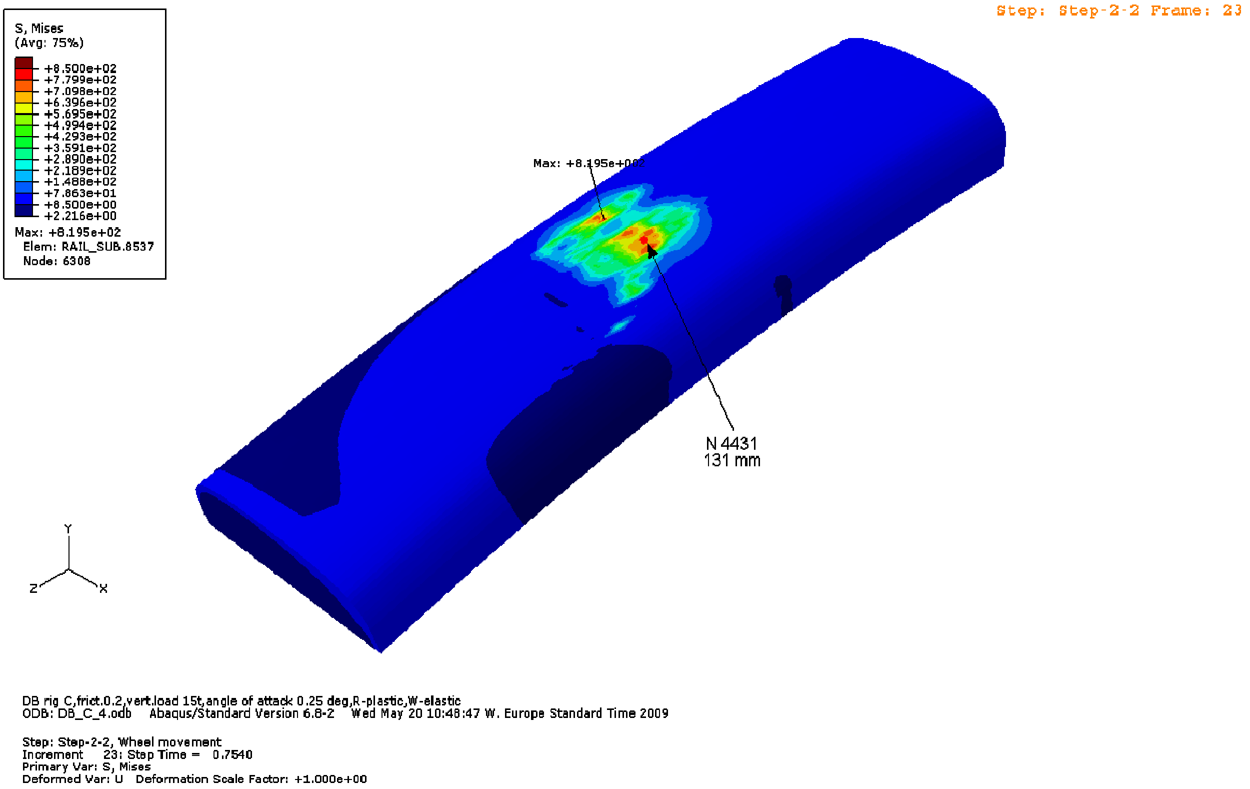
Step: Step-2-2 Frame: 23
S, Mises
(Avg: 75%)
+8.500e+02
+7.799e+02
+7.098e+02
+6.396e+02
+5.695e+02
+4.994e+02
+4.293e+02
+3.591e+02
+2.890e+02
+2.189e+02
+1.488e+02
+7.863e+01
+8.500e+00
+2.216e+00
Max: +8.195e+02
Elem: RAIL_SUB.8537
Node: 6308
Max: +8.195e+02
N 4431
131 mm
Y
Z
X
DB rig C,frict.0.2,vert.load 15t,angle of attack 0.25 deg,R-plastic,W-elastic
ODB: DB_C_4.odb Abaqus/Standard Version 6.8-2 Wed May 20 10:48:47 W. Europe Standard Time 2009
Step: Step-2-2, Wheel movement
Increment 23: Step Time = 0.7540
Primary Var: S, Mises
Deformed Var: U Deformation Scale Factor: +1.000e+00

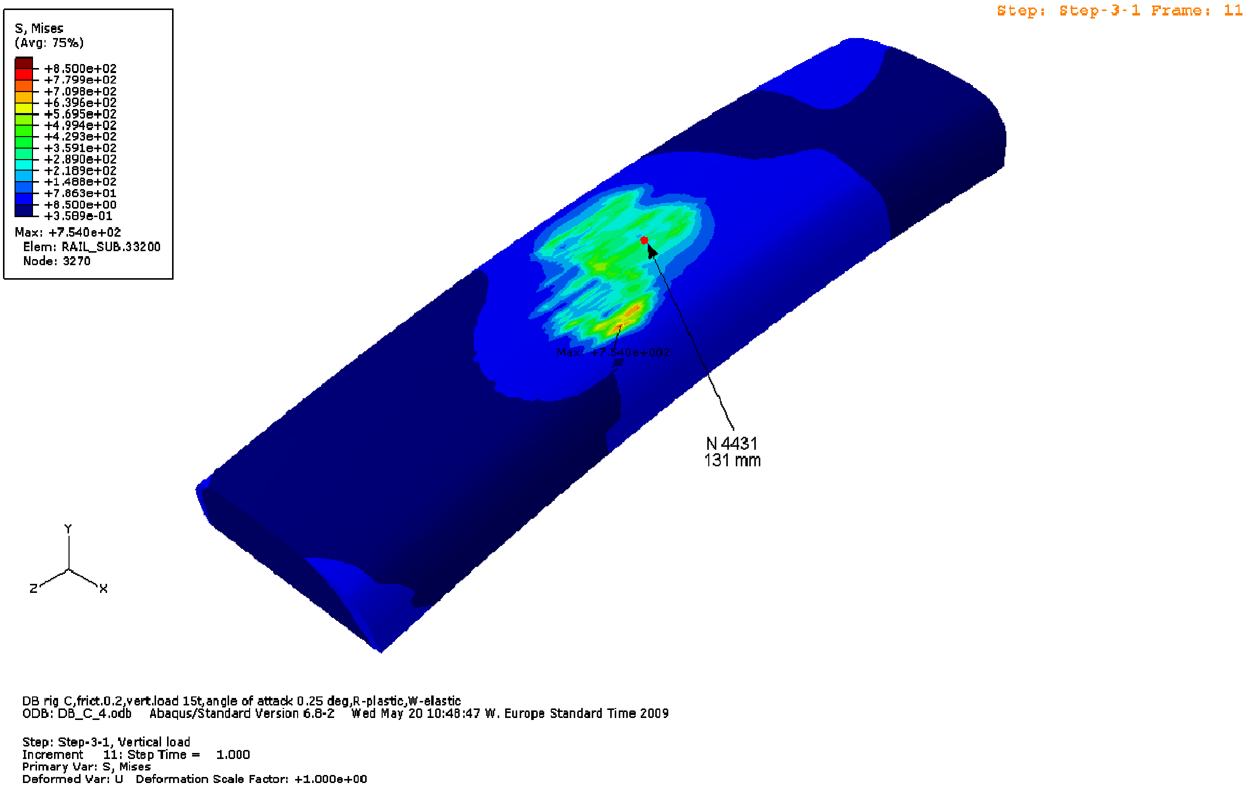
S, Mises
(Avg: 75%)
+8.500e+02
+7.799e+02
+7.098e+02
+6.396e+02
+5.695e+02
+4.994e+02
+4.293e+02
+3.591e+02
+2.890e+02
+2.189e+02
+1.488e+02
+7.863e+01
+8.500e+00
+3.589e-01
Max: +7.540e+02
Elem: RAIL_SUB.33200
Node: 3270
Step: Step-3-1 Frame: 11
Max: +7.540e+02
N 4431
131 mm
Y
Z
X
DB rig C,frict.0.2,vert.load 15t,angle of attack 0.25 deg,R-plastic,W-elastic
ODB: DB_C_4.odb Abaqus/Standard Version 6.8-2 Wed May 20 10:48:47 W. Europe Standard Time 2009
Step: Step-3-1, Vertical load
Increment 11: Step Time = 1.000
Primary Var: S, Mises
Deformed Var: U Deformation Scale Factor: +1.000e+00

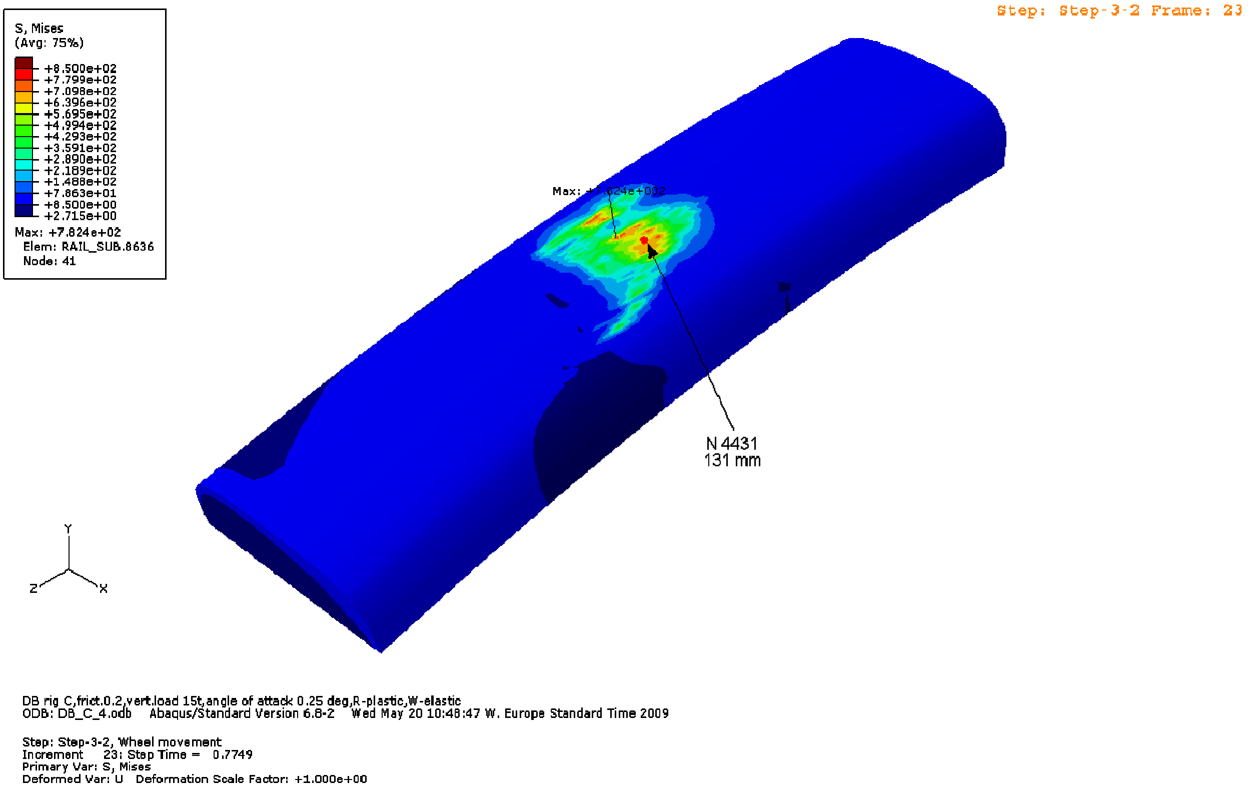
S, Mises
(Avg: 75%)
+8.500e+02
+7.799e+02
+7.098e+02
+6.396e+02
+5.695e+02
+4.994e+02
+4.293e+02
+3.591e+02
+2.890e+02
+2.189e+02
+1.488e+02
+7.863e+01
+8.500e+00
+2.715e+00
Max: +7.824e+02
Elem: RAIL_SUB.8636
Node: 41
Step: Step-3-2 Frame: 23
Max: +7.824e+02
N 4431
131 mm
Y
Z
X
DB rig C,frict.0.2,vert.load 15t,angle of attack 0.25 deg,R-plastic,W-elastic
ODB: DB_C_4.odb Abaqus/Standard Version 6.8-2 Wed May 20 10:48:47 W. Europe Standard Time 2009
Step: Step-3-2, Wheel movement
Increment 23: Step Time = 0.7749
Primary Var: S, Mises
Deformed Var: U Deformation Scale Factor: +1.000e+00

## 12.4 Evolution of the contact pressure

In the following figures the distribution of the contact pressure (denoted CPRESS) effective stress is shown for the following load cases.

- C1 – S1 – I11
- C2 – S2 – I20
- C2 – S1 – I11
- C2 – S2 – I23
- C3 – S1 – I11
- C3 – S2 – I23
- C4 – S1 – I11
- C4 – S2 – I28
- C5 – S1 – I11
- C5 – S2 – I26

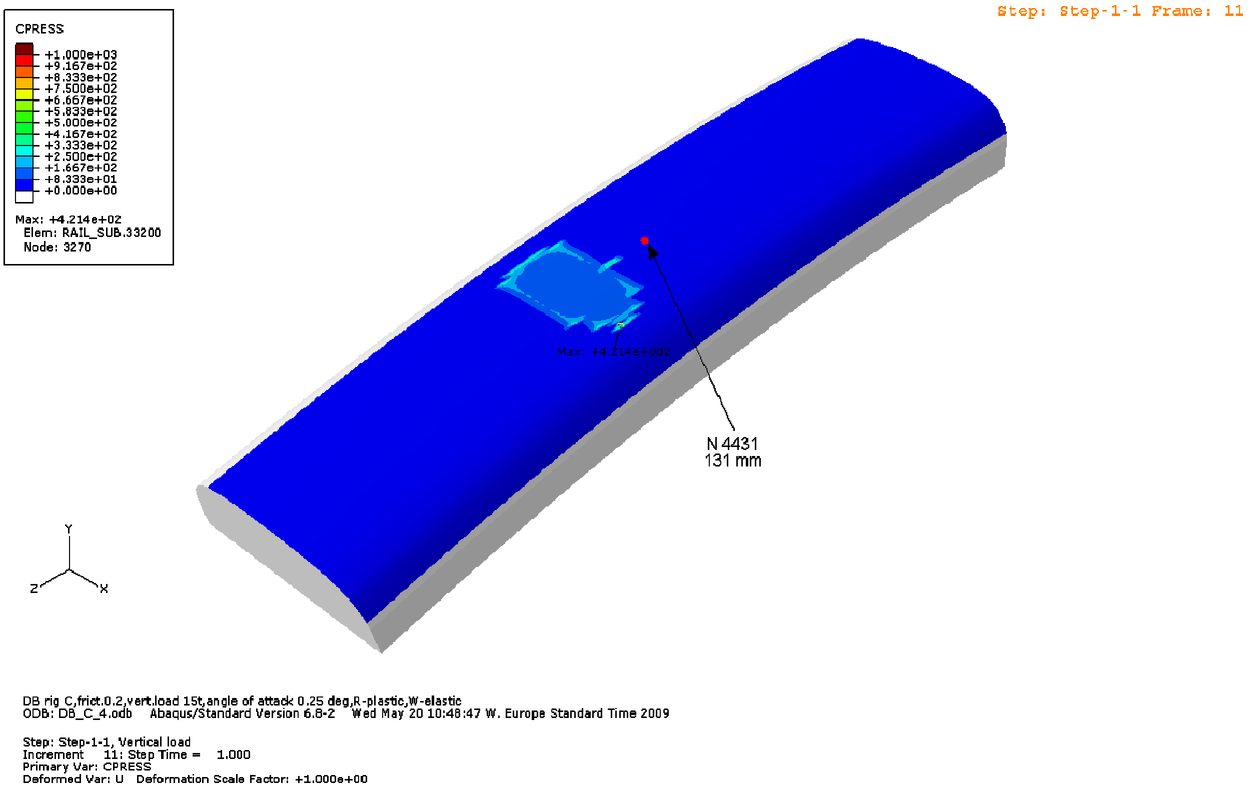
Step: Step-1-1 Frame: 11
CPRESS
+1.000e+03
+9.167e+02
+8.333e+02
+7.500e+02
+6.667e+02
+5.833e+02
+5.000e+02
+4.167e+02
+3.333e+02
+2.500e+02
+1.667e+02
+8.333e+01
+0.000e+00
Max: +4.214e+02
Elem: RAIL_SUB.33200
Node: 3270
Max: +4.214e+002
N 4431
131 mm
Y
Z
X
DB rig C,frict.0.2,vert.load 15t,angle of attack 0.25 deg,R-plastic,W-elastic
ODB: DB_C_4.odb Abaqus/Standard Version 6.8-2 Wed May 20 10:48:47 W. Europe Standard Time 2009
Step: Step-1-1, Vertical load
Increment 11: Step Time = 1.000
Primary Var: CPRESS
Deformed Var: U Deformation Scale Factor: +1.000e+00

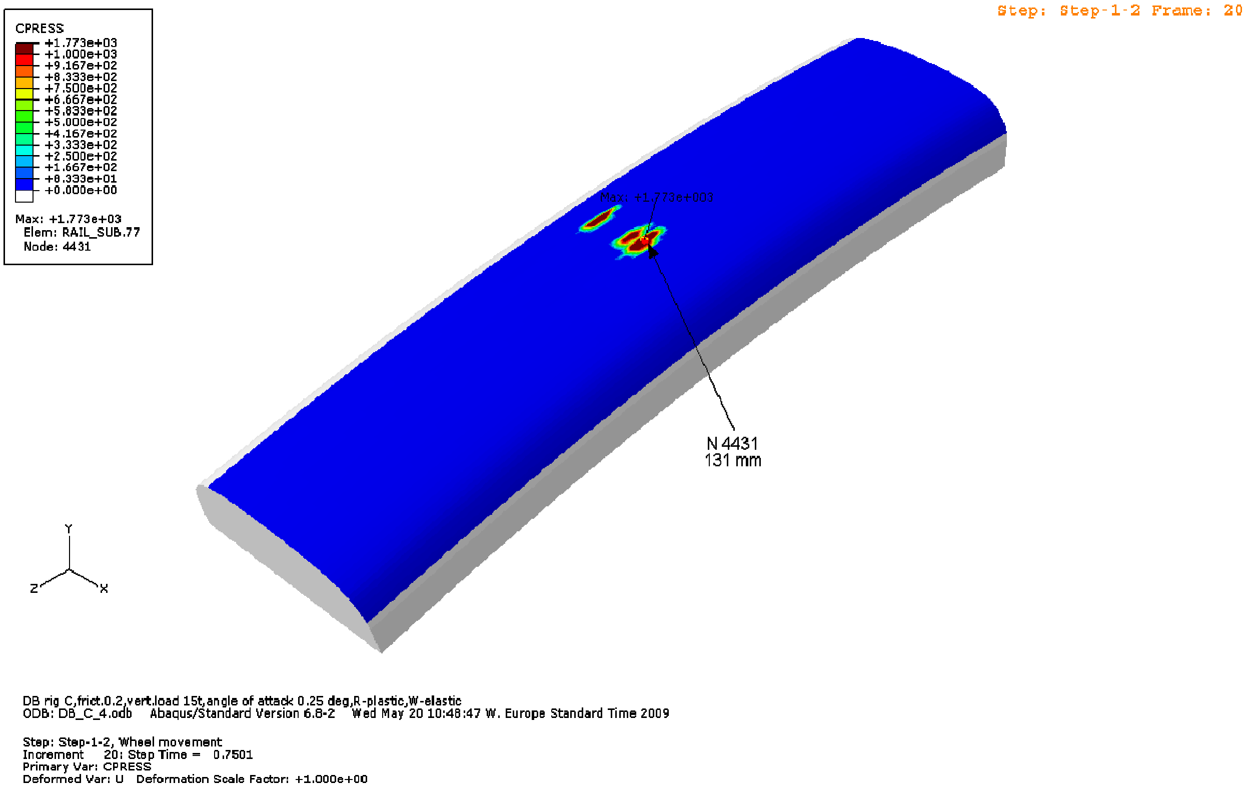
Step: Step-1-2 Frame: 20
CPRESS
+1.773e+03
+1.000e+03
+9.167e+02
+8.333e+02
+7.500e+02
+6.667e+02
+5.833e+02
+5.000e+02
+4.167e+02
+3.333e+02
+2.500e+02
+1.667e+02
+8.333e+01
+0.000e+00
Max: +1.773e+03
Elem: RAIL_SUB.77
Node: 4431
Max: +1.773e+003
N 4431
131 mm
Y
Z
X
DB rig C,frict.0.2,vert.load 15t,angle of attack 0.25 deg,R-plastic,W-elastic
ODB: DB_C_4.odb Abaqus/Standard Version 6.8-2 Wed May 20 10:48:47 W. Europe Standard Time 2009
Step: Step-1-2, Wheel movement
Increment 20: Step Time = 0.7501
Primary Var: CPRESS
Deformed Var: U Deformation Scale Factor: +1.000e+00

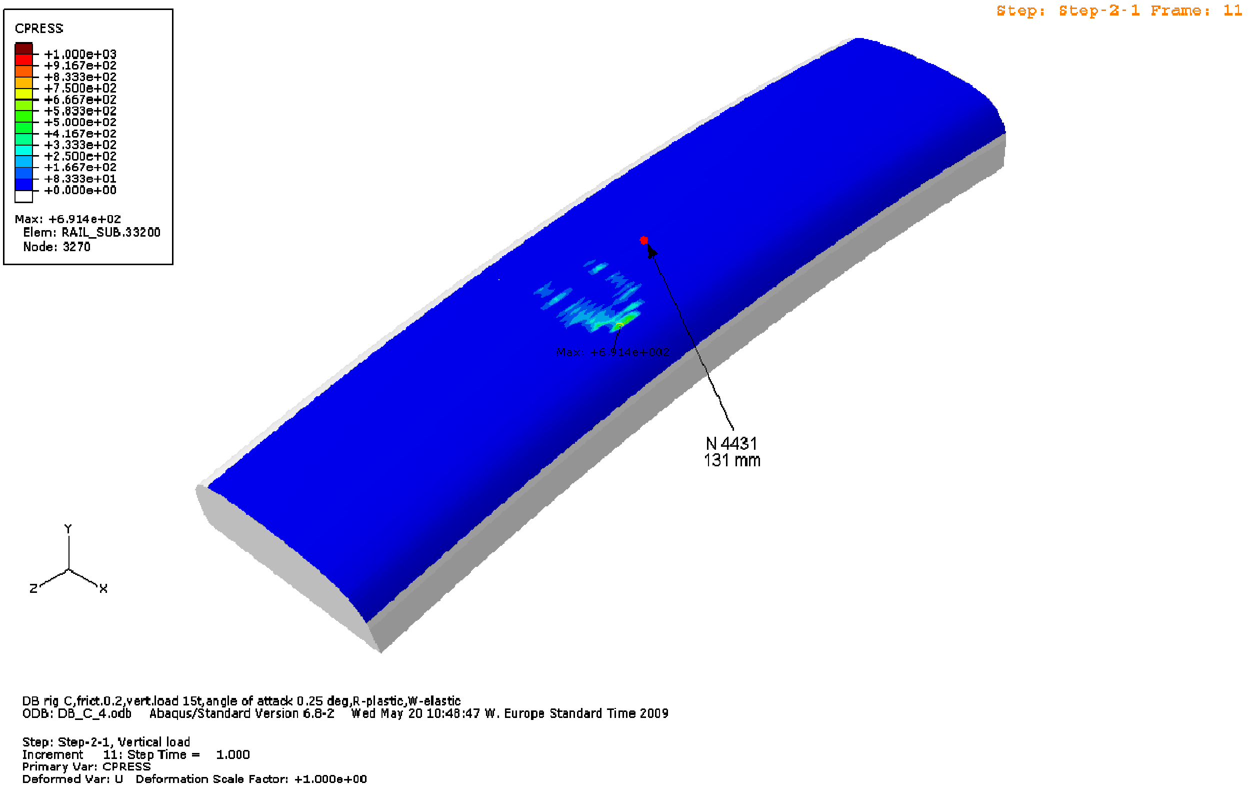
CPRESS
+1.000e+03
+9.167e+02
+8.333e+02
+7.500e+02
+6.667e+02
+5.833e+02
+5.000e+02
+4.167e+02
+3.333e+02
+2.500e+02
+1.667e+02
+8.333e+01
+0.000e+00
Max: +6.914e+02
Elem: RAIL_SUB.33200
Node: 3270
Step: Step-2-1 Frame: 11
Max: +6.914e+02
N 4431
131 mm
Y
Z
X
DB rig C,frict.0.2,vert.load 15t,angle of attack 0.25 deg,R-plastic,W-elastic
ODB: DB_C_4.odb Abaqus/Standard Version 6.8-2 Wed May 20 10:48:47 W. Europe Standard Time 2009
Step: Step-2-1, Vertical load
Increment 11: Step Time = 1.000
Primary Var: CPRESS
Deformed Var: U Deformation Scale Factor: +1.000e+00

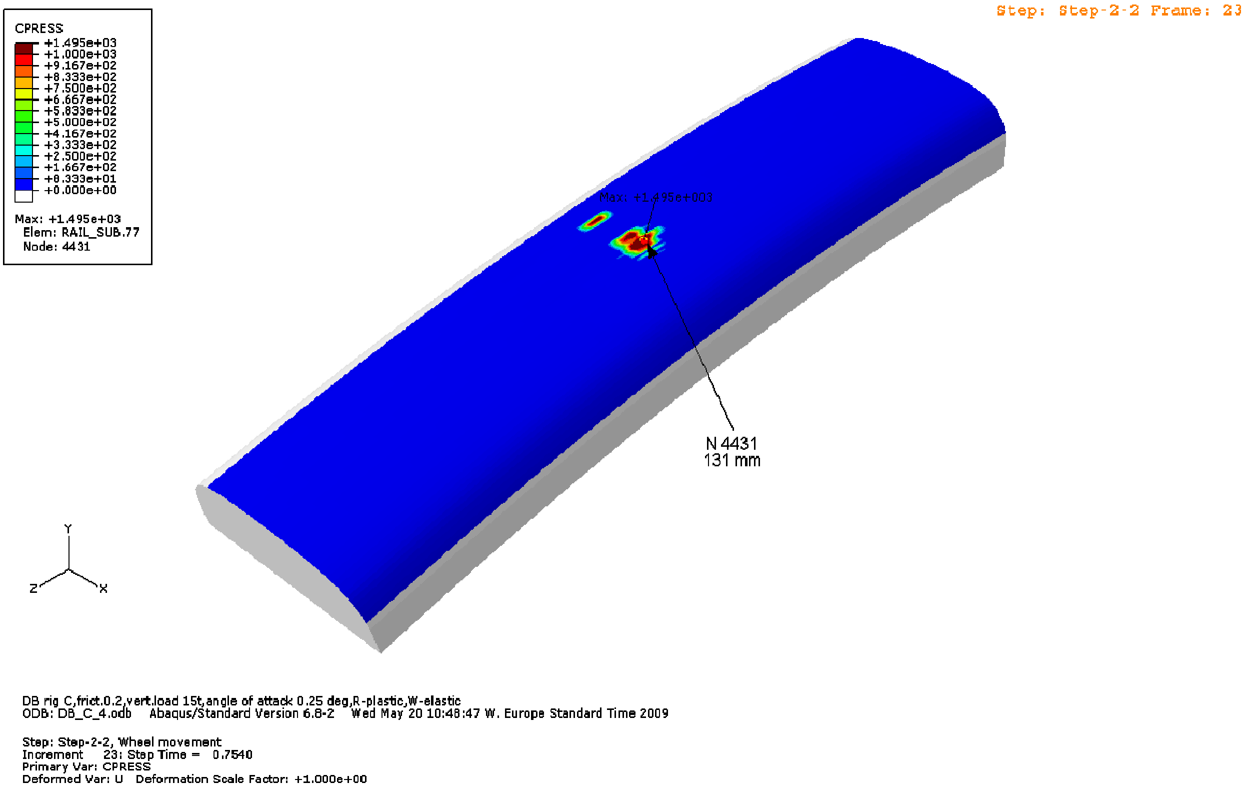
CPRESS
+1.495e+03
+1.000e+03
+9.167e+02
+8.333e+02
+7.500e+02
+6.667e+02
+5.833e+02
+5.000e+02
+4.167e+02
+3.333e+02
+2.500e+02
+1.667e+02
+8.333e+01
+0.000e+00
Max: +1.495e+03
Elem: RAIL_SUB.77
Node: 4431
Step: Step-2-2 Frame: 23
Max: +1.495e+03
N 4431
131 mm
Y
Z
X
DB rig C,frict.0.2,vert.load 15t,angle of attack 0.25 deg,R-plastic,W-elastic
ODB: DB_C_4.odb Abaqus/Standard Version 6.8-2 Wed May 20 10:48:47 W. Europe Standard Time 2009
Step: Step-2-2, Wheel movement
Increment 23: Step Time = 0.7540
Primary Var: CPRESS
Deformed Var: U Deformation Scale Factor: +1.000e+00

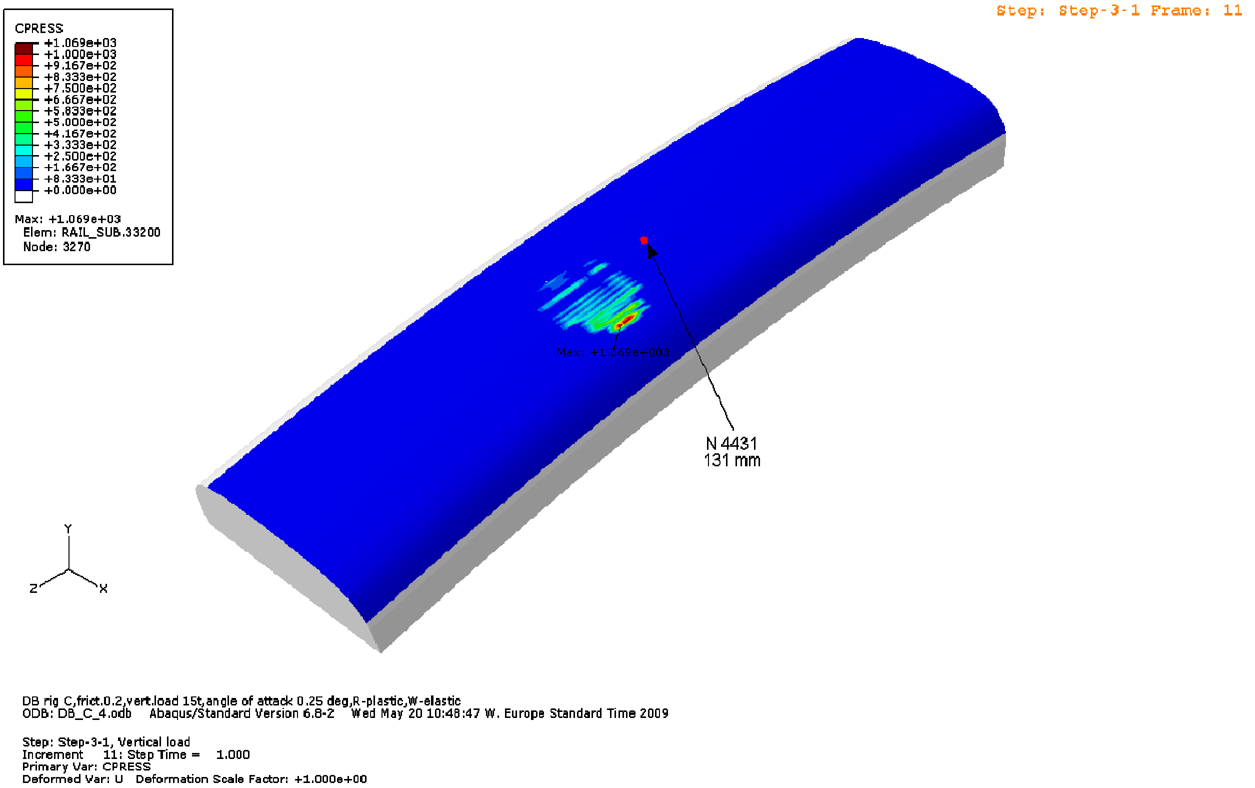
Step: Step-3-1 Frame: 11
CPRESS
+1.069e+03
+1.000e+03
+9.167e+02
+8.333e+02
+7.500e+02
+6.667e+02
+5.833e+02
+5.000e+02
+4.167e+02
+3.333e+02
+2.500e+02
+1.667e+02
+8.333e+01
+0.000e+00
Max: +1.069e+03
Elem: RAIL_SUB.33200
Node: 3270
Max: +1.069e+03
N 4431
131 mm
Y
Z
X

DB rig C,frict.0.2,vert.load 15t,angle of attack 0.25 deg,R-plastic,W-elastic
ODB: DB_C_4.odb    Abaqus/Standard Version 6.8-2    Wed May 20 10:48:47 W. Europe Standard Time 2009

Step: Step-3-1, Vertical load
Increment    11: Step Time =    1.000
Primary Var: CPRESS
Deformed Var: U   Deformation Scale Factor: +1.000e+00

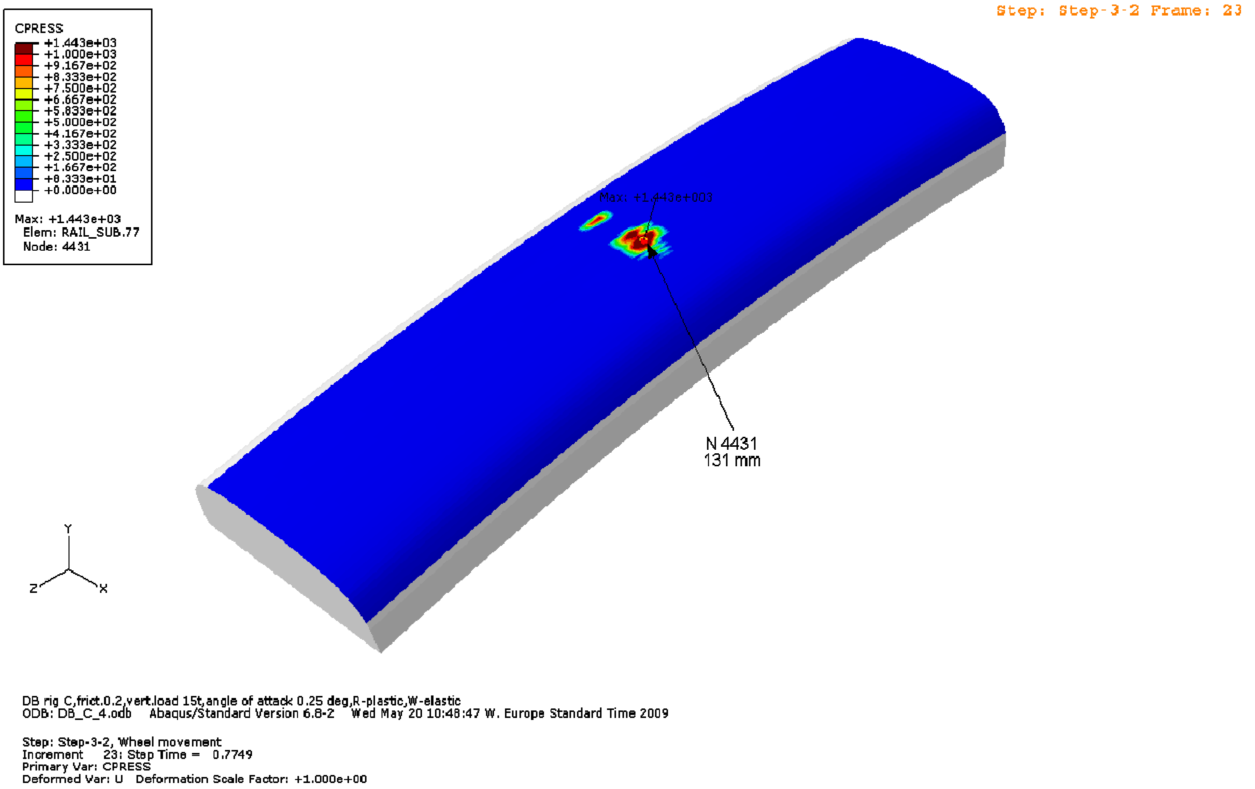
Step: Step-3-2 Frame: 23
CPRESS
+1.443e+03
+1.000e+03
+9.167e+02
+8.333e+02
+7.500e+02
+6.667e+02
+5.833e+02
+5.000e+02
+4.167e+02
+3.333e+02
+2.500e+02
+1.667e+02
+8.333e+01
+0.000e+00
Max: +1.443e+03
Elem: RAIL_SUB.77
Node: 4431
Max: +1.443e+03
N 4431
131 mm
Y
Z
X

DB rig C,frict.0.2,vert.load 15t,angle of attack 0.25 deg,R-plastic,W-elastic
ODB: DB_C_4.odb    Abaqus/Standard Version 6.8-2    Wed May 20 10:48:47 W. Europe Standard Time 2009

Step: Step-3-2, Wheel movement
Increment    23: Step Time =    0.7749
Primary Var: CPRESS
Deformed Var: U   Deformation Scale Factor: +1.000e+00

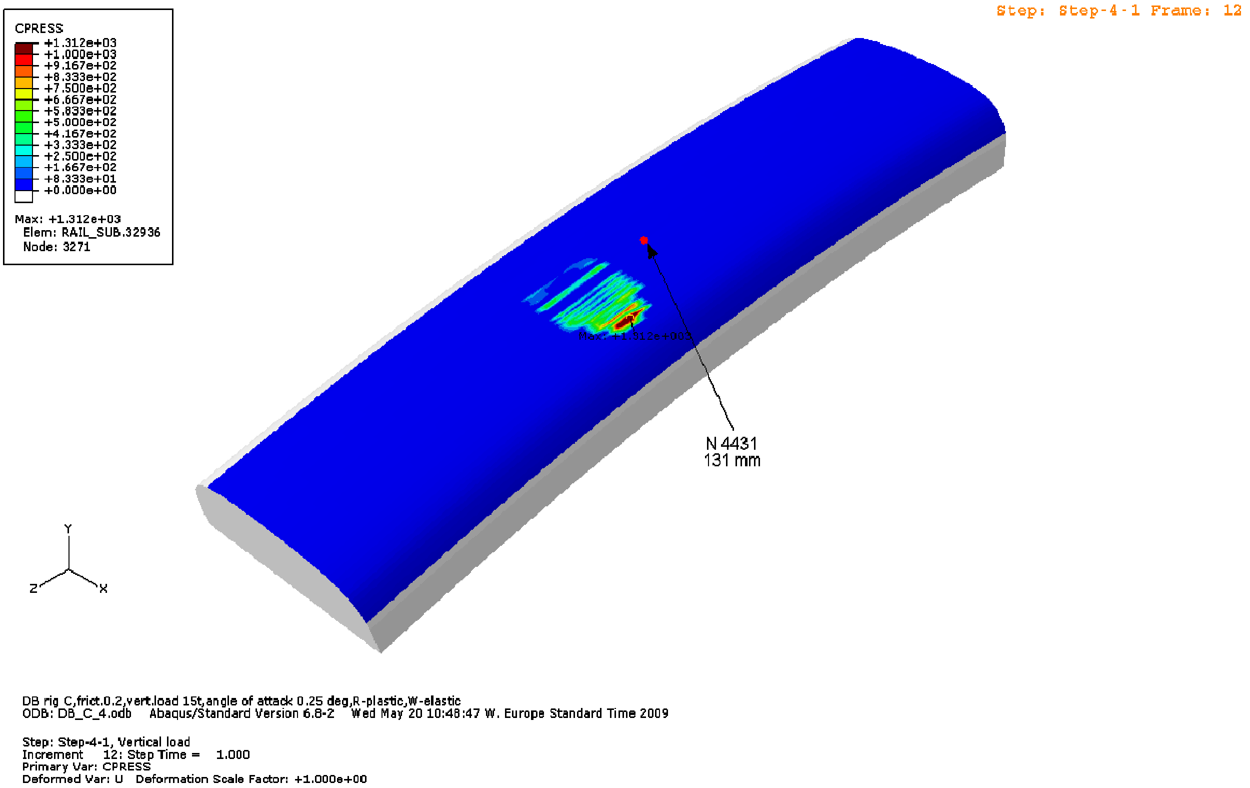
Step: Step-4-1 Frame: 12
CPRESS
+1.312e+03
+1.000e+03
+9.167e+02
+8.333e+02
+7.500e+02
+6.667e+02
+5.833e+02
+5.000e+02
+4.167e+02
+3.333e+02
+2.500e+02
+1.667e+02
+8.333e+01
+0.000e+00
Max: +1.312e+03
Elem: RAIL_SUB.32936
Node: 3271
Max: +1.312e+003
N 4431
131 mm
Y
Z
X

```
DB rig C,frict.0.2,vert.load 15t,angle of attack 0.25 deg,R-plastic,W-elastic
ODB: DB_C_4.odb    Abaqus/Standard Version 6.8-2    Wed May 20 10:48:47 W. Europe Standard Time 2009

Step: Step-4-1, Vertical load
Increment     12: Step Time =    1.000
Primary Var: CPRESS
Deformed Var: U   Deformation Scale Factor: +1.000e+00
```

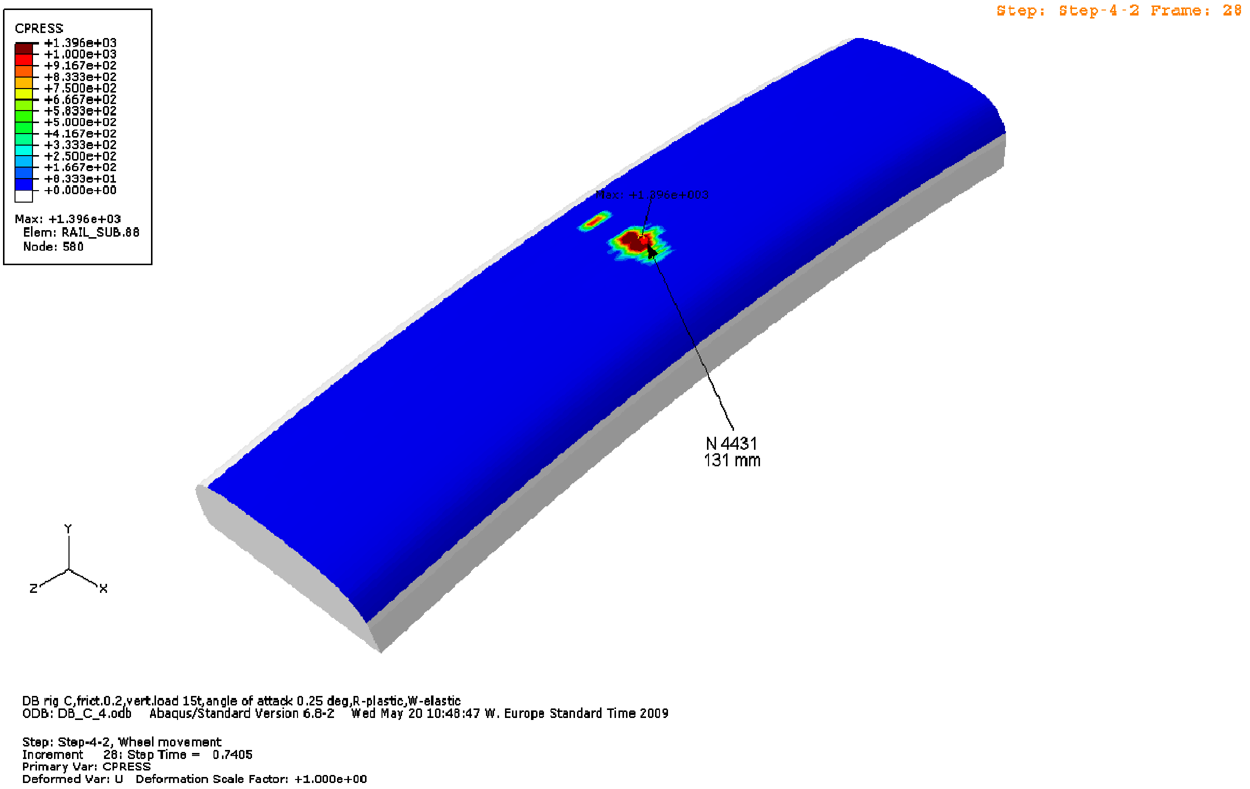
Step: Step-4-2 Frame: 28
CPRESS
+1.396e+03
+1.000e+03
+9.167e+02
+8.333e+02
+7.500e+02
+6.667e+02
+5.833e+02
+5.000e+02
+4.167e+02
+3.333e+02
+2.500e+02
+1.667e+02
+8.333e+01
+0.000e+00
Max: +1.396e+03
Elem: RAIL_SUB.88
Node: 580
Max: +1.396e+003
N 4431
131 mm
Y
Z
X

```
DB rig C,frict.0.2,vert.load 15t,angle of attack 0.25 deg,R-plastic,W-elastic
ODB: DB_C_4.odb    Abaqus/Standard Version 6.8-2    Wed May 20 10:48:47 W. Europe Standard Time 2009

Step: Step-4-2, Wheel movement
Increment     28: Step Time =    0.7405
Primary Var: CPRESS
Deformed Var: U   Deformation Scale Factor: +1.000e+00
```

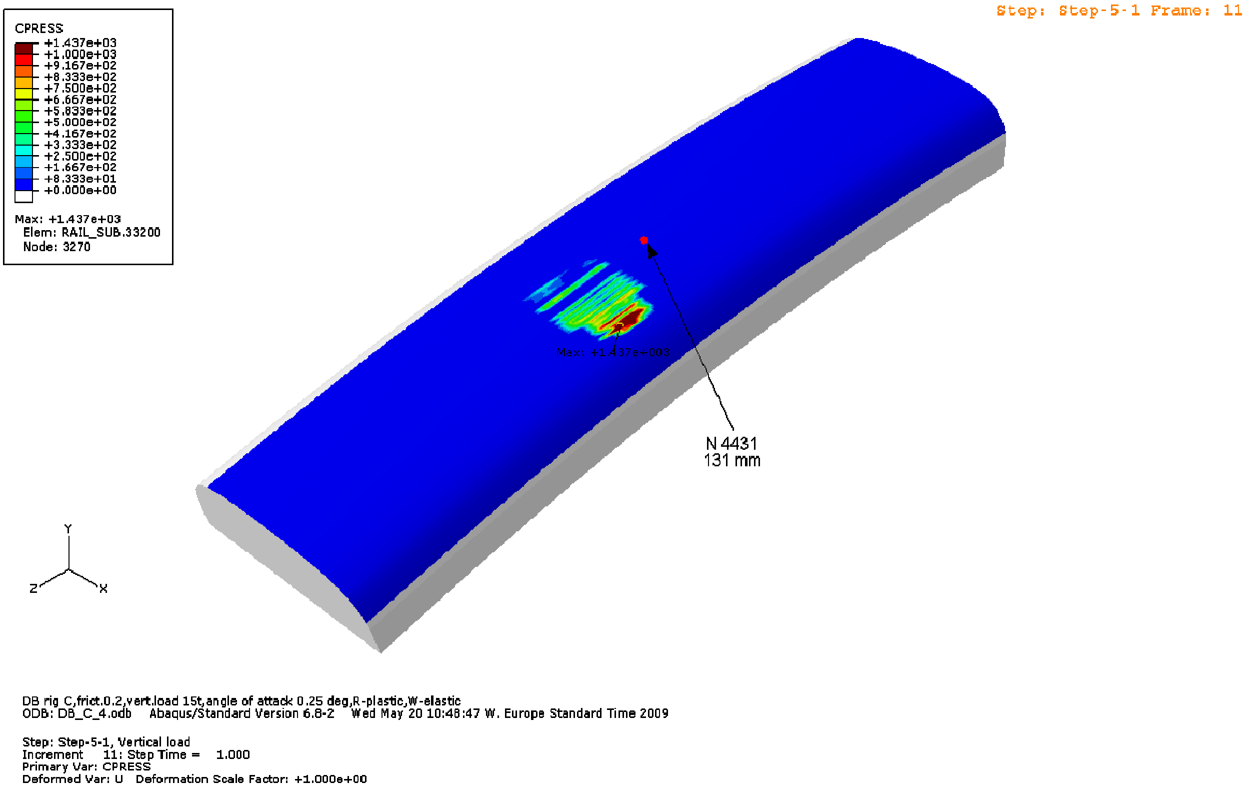
Step: Step-5-1 Frame: 11
CPRESS
+1.437e+03
+1.000e+03
+9.167e+02
+8.333e+02
+7.500e+02
+6.667e+02
+5.833e+02
+5.000e+02
+4.167e+02
+3.333e+02
+2.500e+02
+1.667e+02
+8.333e+01
+0.000e+00
Max: +1.437e+03
Elem: RAIL_SUB.33200
Node: 3270
Max: +1.437e+03
N 4431
131 mm
Y
Z
X

DB rig C,frict.0.2,vert.load 15t,angle of attack 0.25 deg,R-plastic,W-elastic
ODB: DB_C_4.odb Abaqus/Standard Version 6.8-2 Wed May 20 10:48:47 W. Europe Standard Time 2009

Step: Step-5-1, Vertical load
Increment 11: Step Time = 1.000
Primary Var: CPRESS
Deformed Var: U Deformation Scale Factor: +1.000e+00

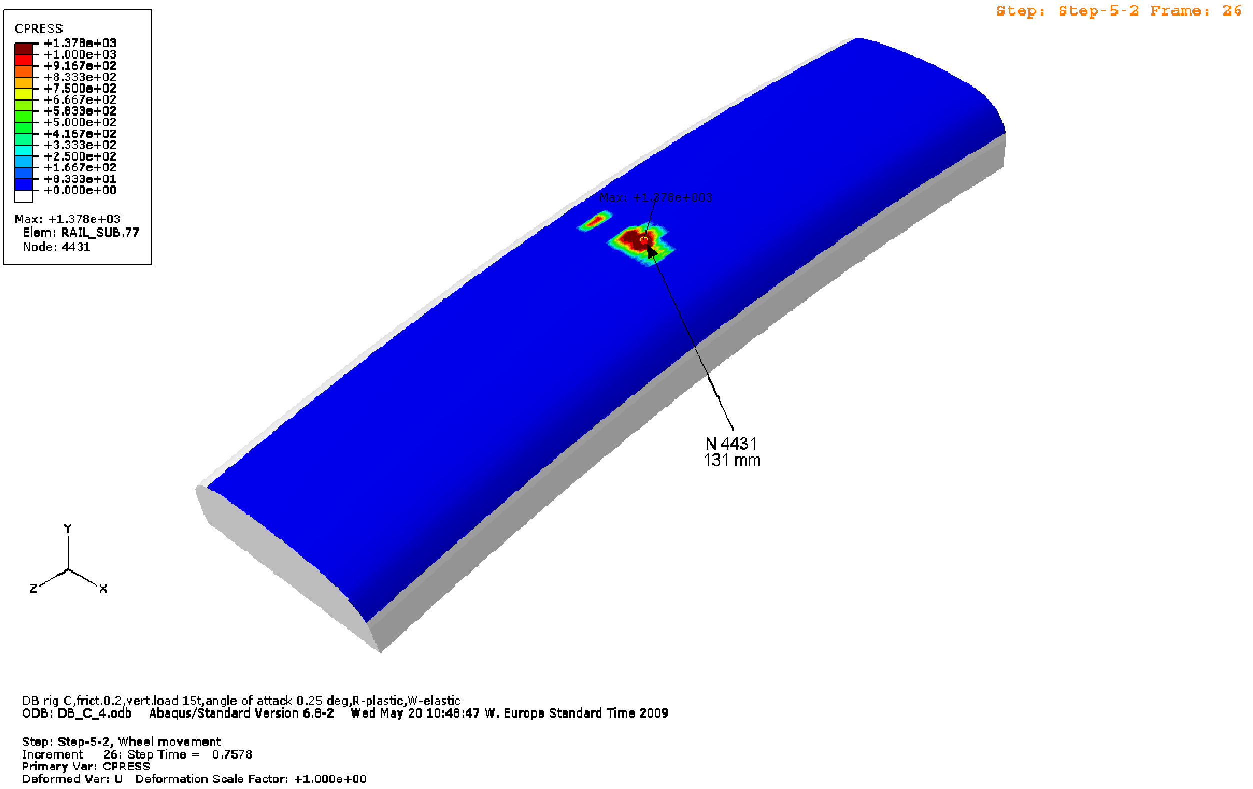
Step: Step-5-2 Frame: 26
CPRESS
+1.378e+03
+1.000e+03
+9.167e+02
+8.333e+02
+7.500e+02
+6.667e+02
+5.833e+02
+5.000e+02
+4.167e+02
+3.333e+02
+2.500e+02
+1.667e+02
+8.333e+01
+0.000e+00
Max: +1.378e+03
Elem: RAIL_SUB.77
Node: 4431
Max: +1.378e+03
N 4431
131 mm
Y
Z
X

DB rig C,frict.0.2,vert.load 15t,angle of attack 0.25 deg,R-plastic,W-elastic
ODB: DB_C_4.odb Abaqus/Standard Version 6.8-2 Wed May 20 10:48:47 W. Europe Standard Time 2009

Step: Step-5-2, Wheel movement
Increment 26: Step Time = 0.7578
Primary Var: CPRESS
Deformed Var: U Deformation Scale Factor: +1.000e+00

## 12.5 Evolution of equivalent plastic strain

In the following figures the distribution of the equivalent plastic strain (denoted PEEQ) is shown for the following load cases.

- C1 – S1 – I11
- C2 – S2 – I20
- C2 – S1 – I11
- C2 – S2 – I23
- C3 – S1 – I11
- C3 – S2 – I23
- C4 – S1 – I11
- C4 – S2 – I28
- C5 – S1 – I11
- C5 – S2 – I26

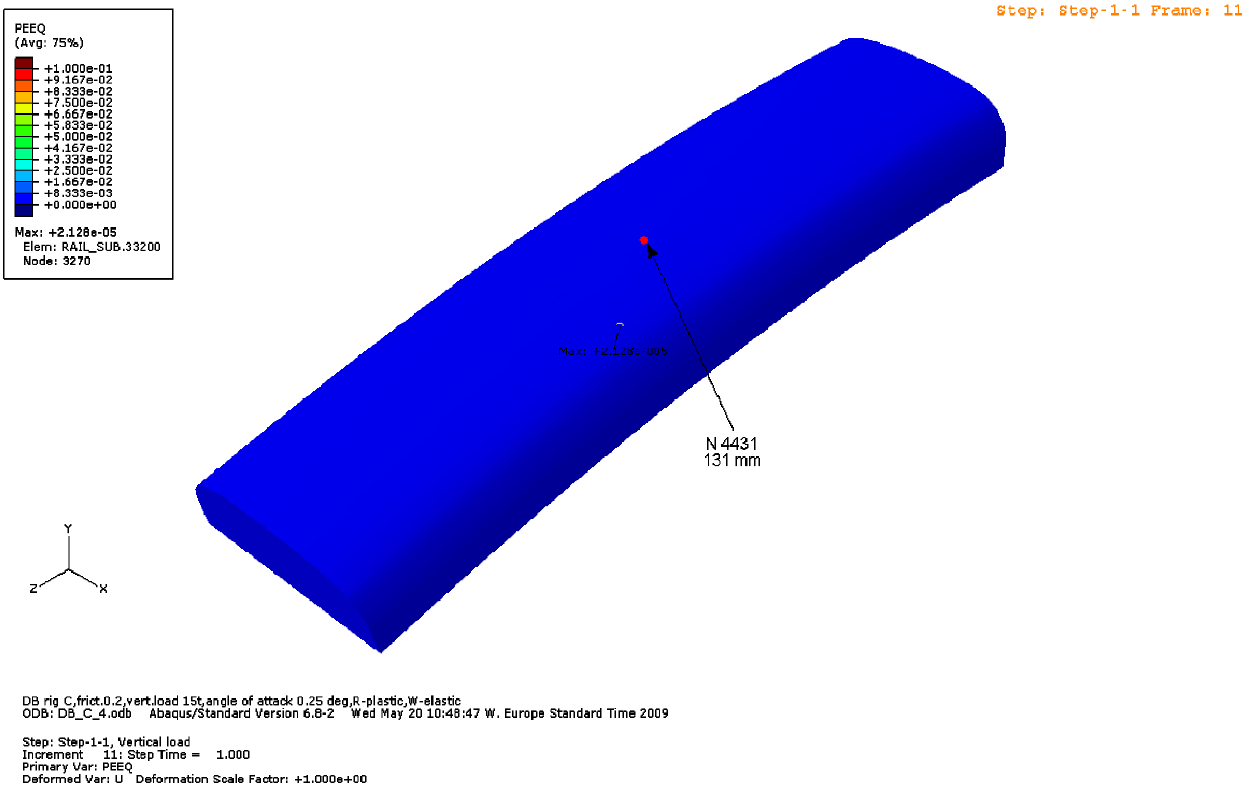
PEEQ
(Avg: 75%)
+1.000e-01
+9.167e-02
+8.333e-02
+7.500e-02
+6.667e-02
+5.833e-02
+5.000e-02
+4.167e-02
+3.333e-02
+2.500e-02
+1.667e-02
+8.333e-03
+0.000e+00
Max: +2.128e-05
Elem: RAIL_SUB.33200
Node: 3270
Step: Step-1-1 Frame: 11
Max: +2.128e-005
N 4431
131 mm
Y
Z
X

```
DB rig C,frict.0.2,vert.load 15t,angle of attack 0.25 deg,R-plastic,W-elastic
ODB: DB_C_4.odb    Abaqus/Standard Version 6.8-2    Wed May 20 10:48:47 W. Europe Standard Time 2009

Step: Step-1-1, Vertical load
Increment     11: Step Time =    1.000
Primary Var: PEEQ
Deformed Var: U   Deformation Scale Factor: +1.000e+00
```

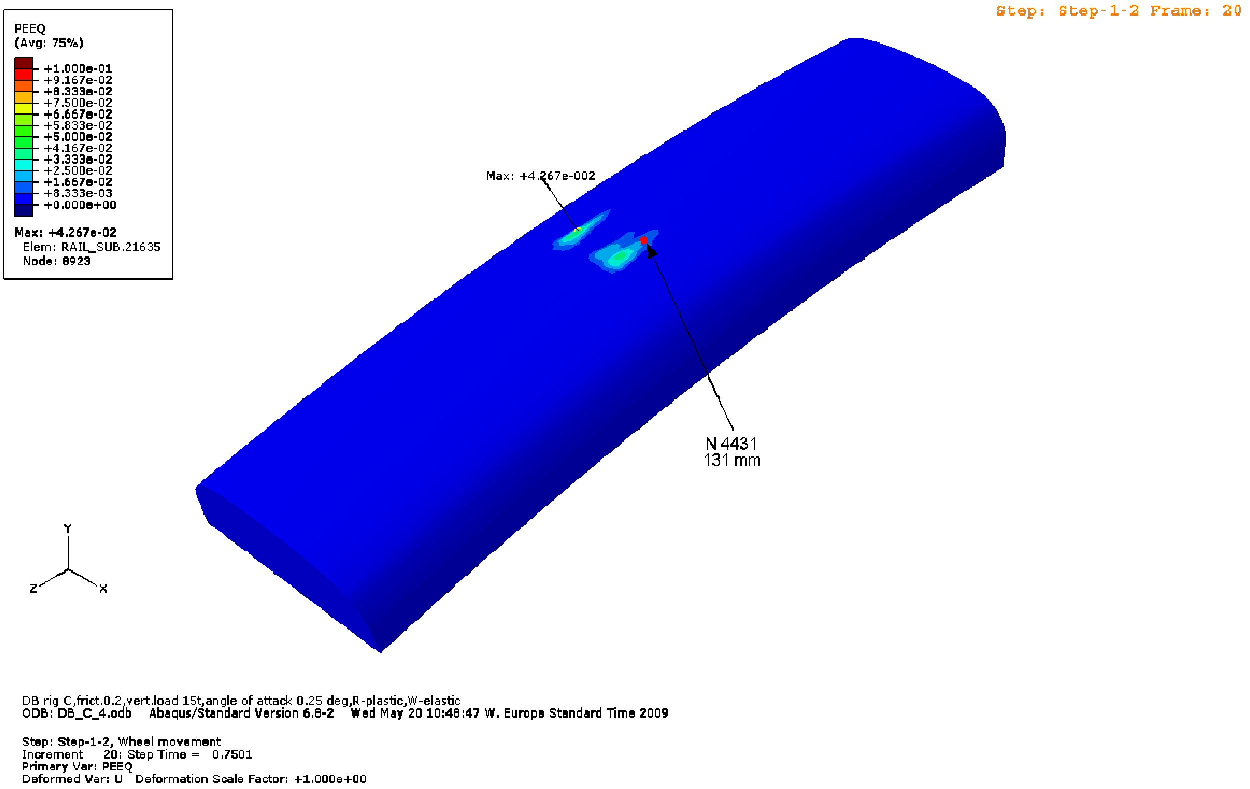
PEEQ
(Avg: 75%)
+1.000e-01
+9.167e-02
+8.333e-02
+7.500e-02
+6.667e-02
+5.833e-02
+5.000e-02
+4.167e-02
+3.333e-02
+2.500e-02
+1.667e-02
+8.333e-03
+0.000e+00
Max: +4.267e-02
Elem: RAIL_SUB.21635
Node: 8923
Step: Step-1-2 Frame: 20
Max: +4.267e-002
N 4431
131 mm
Y
Z
X

```
DB rig C,frict.0.2,vert.load 15t,angle of attack 0.25 deg,R-plastic,W-elastic
ODB: DB_C_4.odb    Abaqus/Standard Version 6.8-2    Wed May 20 10:48:47 W. Europe Standard Time 2009

Step: Step-1-2, Wheel movement
Increment     20: Step Time =    0.7501
Primary Var: PEEQ
Deformed Var: U   Deformation Scale Factor: +1.000e+00
```

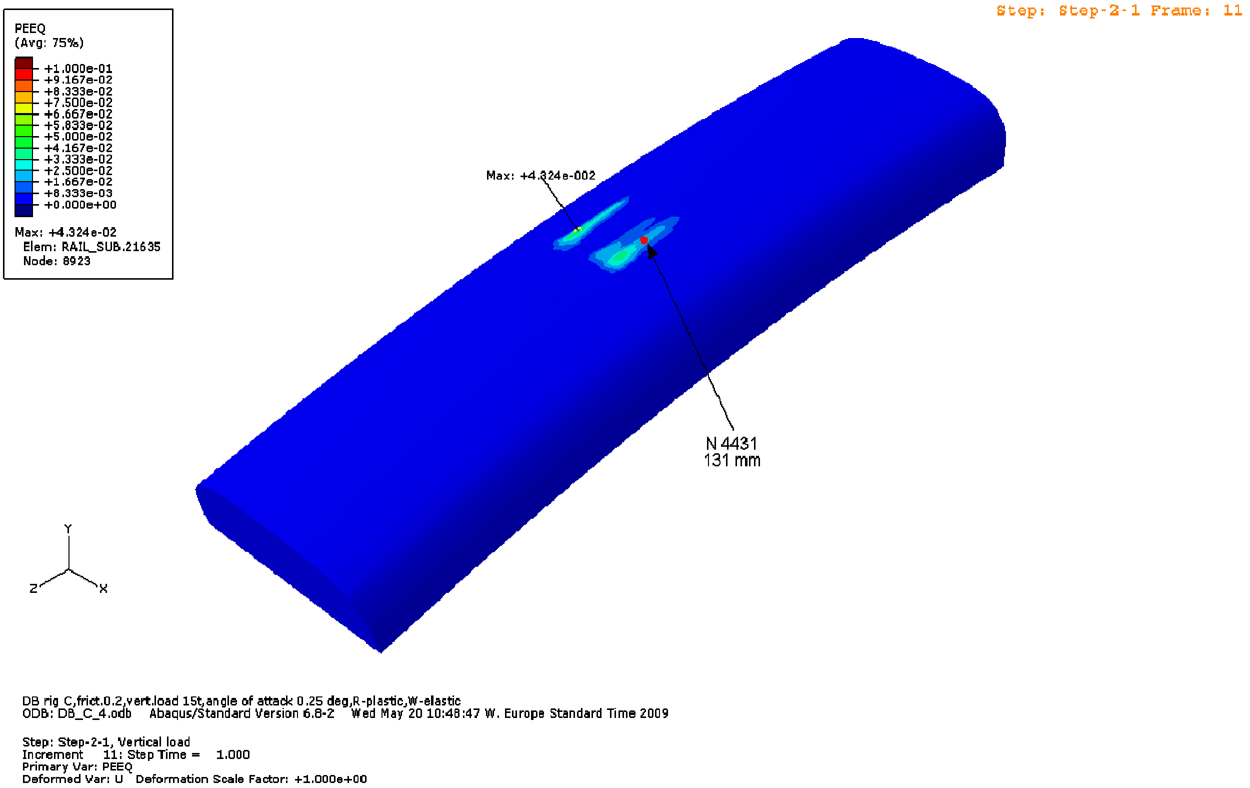
Step: Step-2-1 Frame: 11
PEEQ
(Avg: 75%)
+1.000e-01
+9.167e-02
+8.333e-02
+7.500e-02
+6.667e-02
+5.833e-02
+5.000e-02
+4.167e-02
+3.333e-02
+2.500e-02
+1.667e-02
+8.333e-03
+0.000e+00
Max: +4.324e-02
Elem: RAIL_SUB.21635
Node: 8923
Max: +4.324e-002
N 4431
131 mm
Y
Z
X

DB rig C,frict.0.2,vert.load 15t,angle of attack 0.25 deg,R-plastic,W-elastic
ODB: DB_C_4.odb Abaqus/Standard Version 6.8-2 Wed May 20 10:48:47 W. Europe Standard Time 2009

Step: Step-2-1, Vertical load
Increment 11: Step Time = 1.000
Primary Var: PEEQ
Deformed Var: U Deformation Scale Factor: +1.000e+00

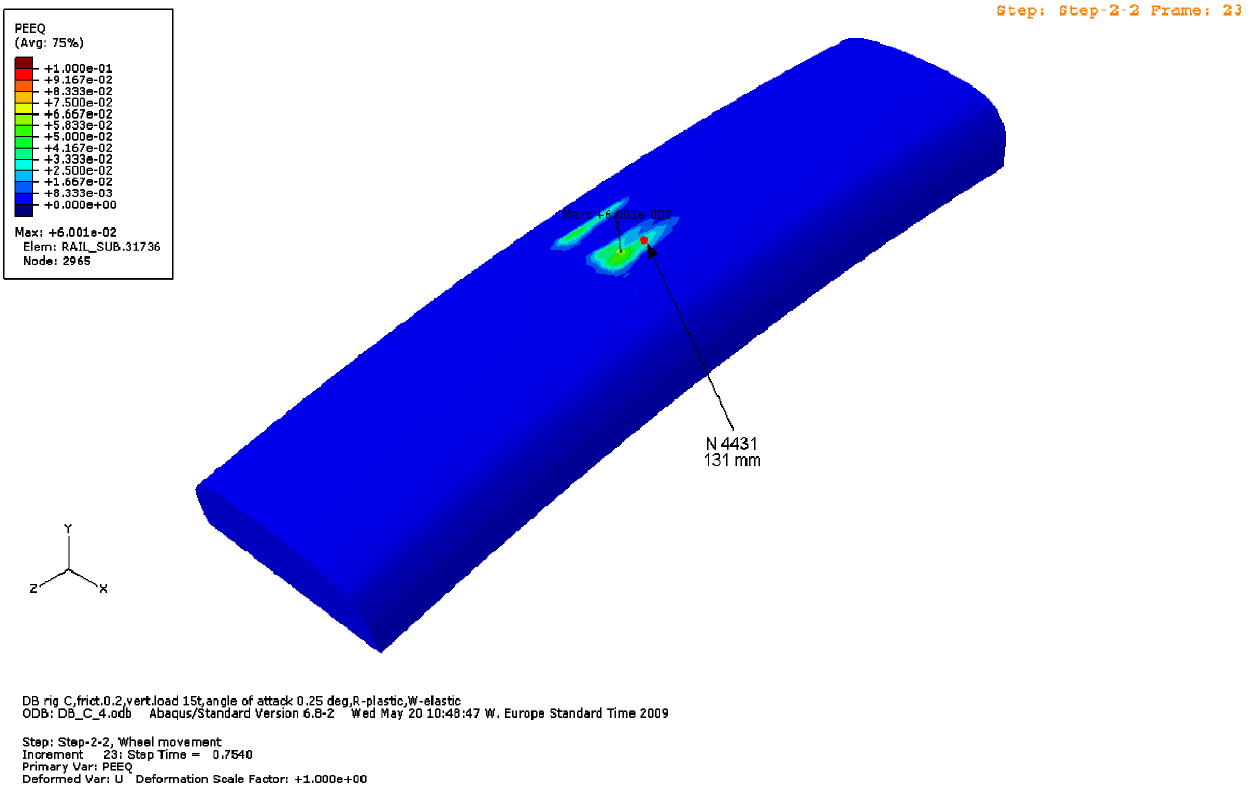
Step: Step-2-2 Frame: 23
PEEQ
(Avg: 75%)
+1.000e-01
+9.167e-02
+8.333e-02
+7.500e-02
+6.667e-02
+5.833e-02
+5.000e-02
+4.167e-02
+3.333e-02
+2.500e-02
+1.667e-02
+8.333e-03
+0.000e+00
Max: +6.001e-02
Elem: RAIL_SUB.31736
Node: 2965
Max: +6.001e-002
N 4431
131 mm
Y
Z
X

DB rig C,frict.0.2,vert.load 15t,angle of attack 0.25 deg,R-plastic,W-elastic
ODB: DB_C_4.odb Abaqus/Standard Version 6.8-2 Wed May 20 10:48:47 W. Europe Standard Time 2009

Step: Step-2-2, Wheel movement
Increment 23: Step Time = 0.7540
Primary Var: PEEQ
Deformed Var: U Deformation Scale Factor: +1.000e+00

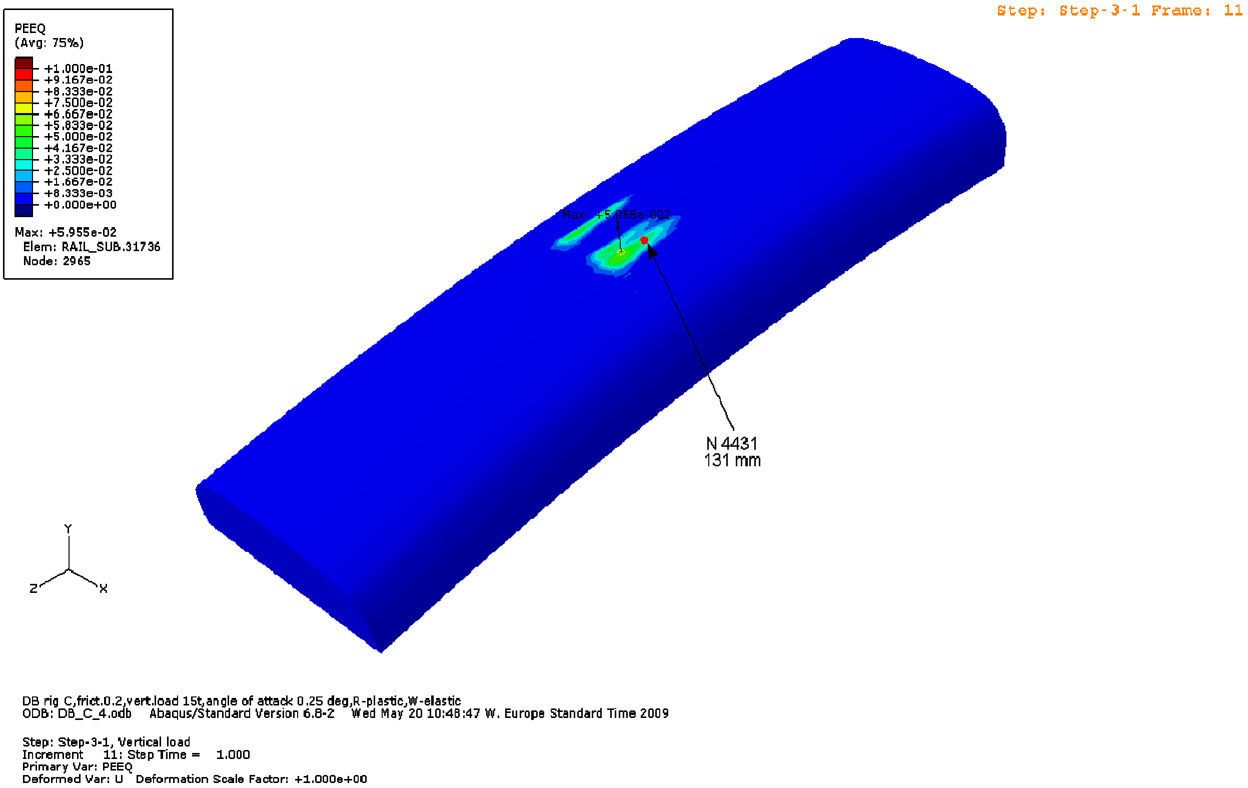
Step: Step-3-1 Frame: 11
PEEQ
(Avg: 75%)
+1.000e-01
+9.167e-02
+8.333e-02
+7.500e-02
+6.667e-02
+5.833e-02
+5.000e-02
+4.167e-02
+3.333e-02
+2.500e-02
+1.667e-02
+8.333e-03
+0.000e+00
Max: +5.955e-02
Elem: RAIL_SUB.31736
Node: 2965
Max: +5.955e-002
N 4431
131 mm
Y
Z
X
DB rig C,frict.0.2,vert.load 15t,angle of attack 0.25 deg,R-plastic,W-elastic
ODB: DB_C_4.odb Abaqus/Standard Version 6.8-2 Wed May 20 10:48:47 W. Europe Standard Time 2009
Step: Step-3-1, Vertical load
Increment 11: Step Time = 1.000
Primary Var: PEEQ
Deformed Var: U Deformation Scale Factor: +1.000e+00

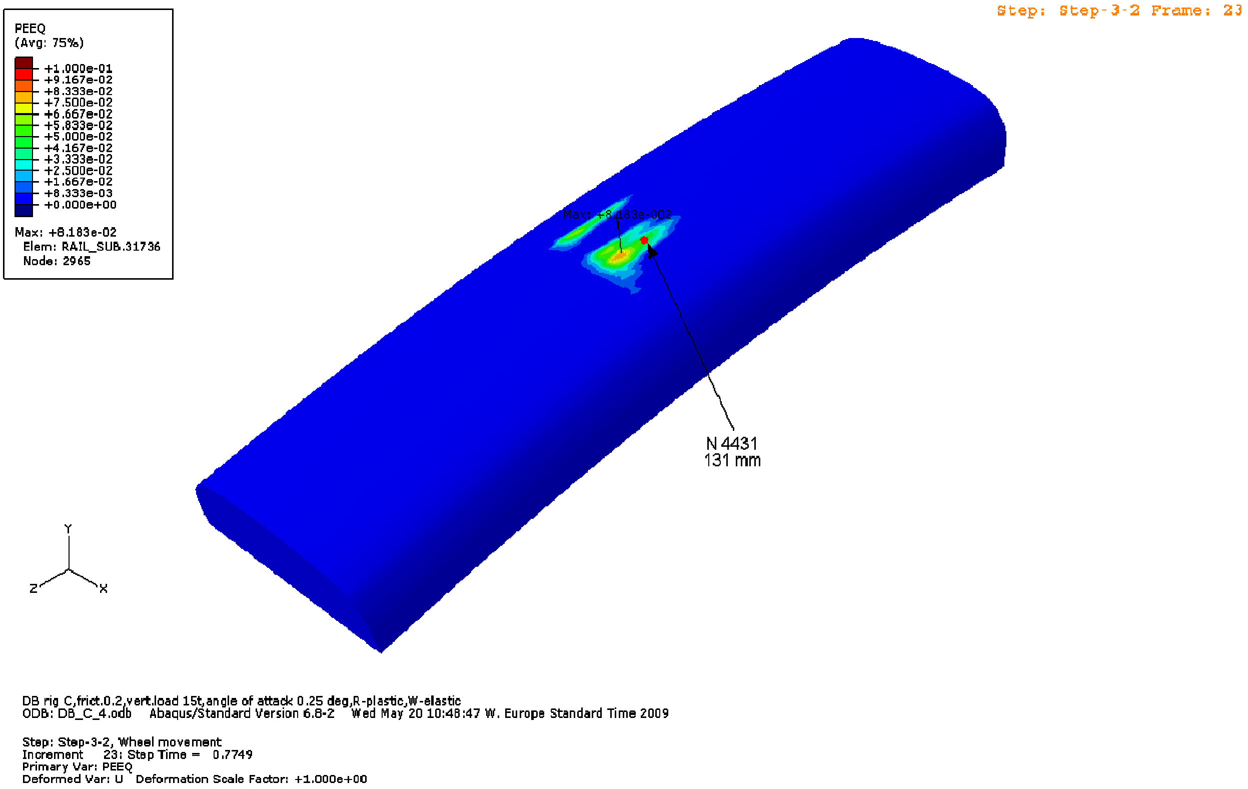
Step: Step-3-2 Frame: 23
PEEQ
(Avg: 75%)
+1.000e-01
+9.167e-02
+8.333e-02
+7.500e-02
+6.667e-02
+5.833e-02
+5.000e-02
+4.167e-02
+3.333e-02
+2.500e-02
+1.667e-02
+8.333e-03
+0.000e+00
Max: +8.183e-02
Elem: RAIL_SUB.31736
Node: 2965
Max: +8.183e-002
N 4431
131 mm
Y
Z
X
DB rig C,frict.0.2,vert.load 15t,angle of attack 0.25 deg,R-plastic,W-elastic
ODB: DB_C_4.odb Abaqus/Standard Version 6.8-2 Wed May 20 10:48:47 W. Europe Standard Time 2009
Step: Step-3-2, Wheel movement
Increment 23: Step Time = 0.7749
Primary Var: PEEQ
Deformed Var: U Deformation Scale Factor: +1.000e+00

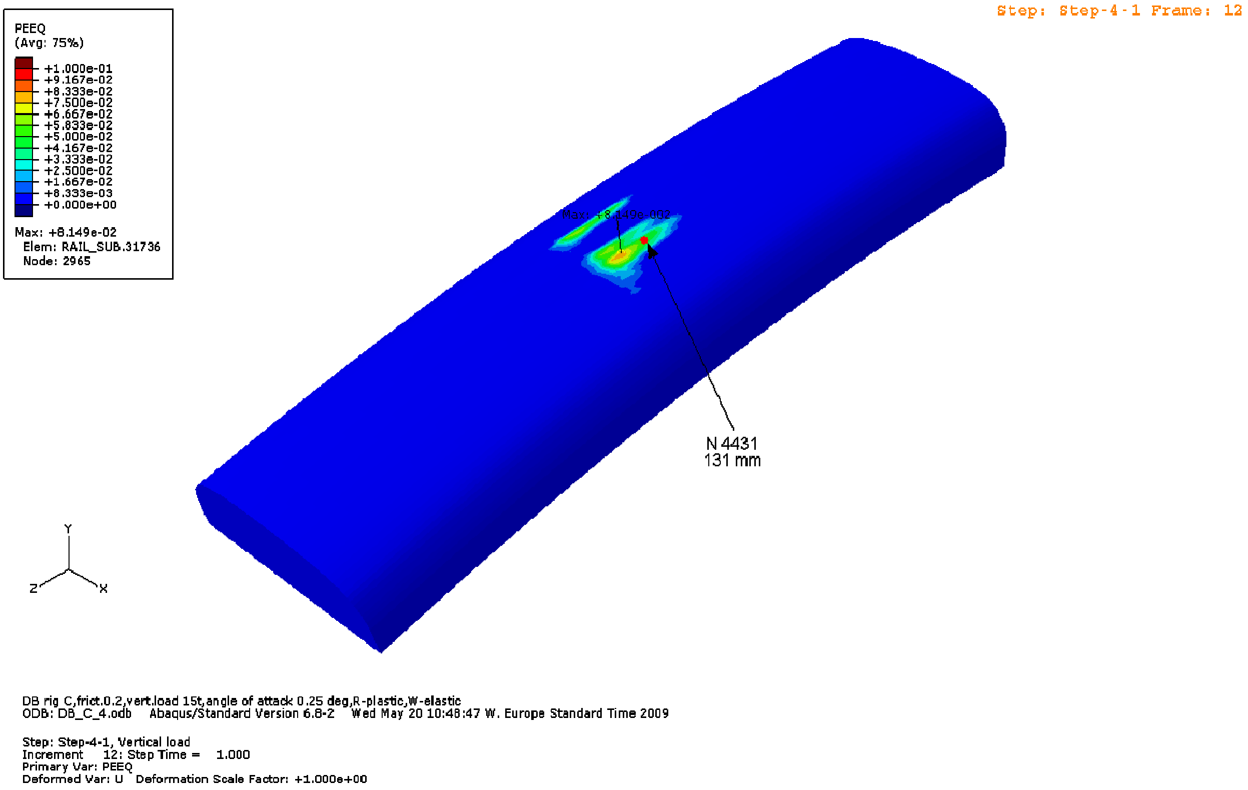
PEEQ
(Avg: 75%)
+1.000e-01
+9.167e-02
+8.333e-02
+7.500e-02
+6.667e-02
+5.833e-02
+5.000e-02
+4.167e-02
+3.333e-02
+2.500e-02
+1.667e-02
+8.333e-03
+0.000e+00
Max: +8.149e-02
Elem: RAIL_SUB.31736
Node: 2965
Step: Step-4-1 Frame: 12
Max: +8.149e-002
N 4431
131 mm
Y
Z
X
DB rig C,frict.0.2,vert.load 15t,angle of attack 0.25 deg,R-plastic,W-elastic
ODB: DB_C_4.odb Abaqus/Standard Version 6.8-2 Wed May 20 10:48:47 W. Europe Standard Time 2009
Step: Step-4-1, Vertical load
Increment 12: Step Time = 1.000
Primary Var: PEEQ
Deformed Var: U Deformation Scale Factor: +1.000e+00

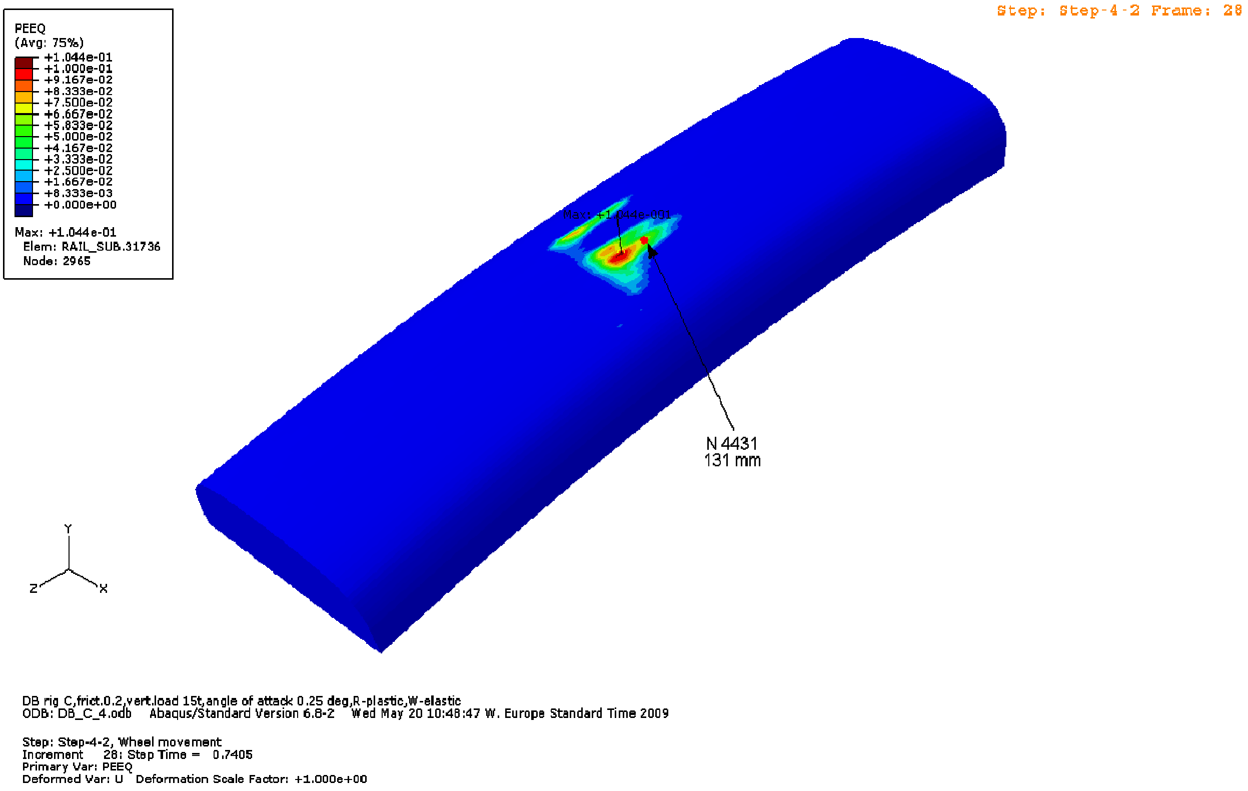
PEEQ
(Avg: 75%)
+1.044e-01
+1.000e-01
+9.167e-02
+8.333e-02
+7.500e-02
+6.667e-02
+5.833e-02
+5.000e-02
+4.167e-02
+3.333e-02
+2.500e-02
+1.667e-02
+8.333e-03
+0.000e+00
Max: +1.044e-01
Elem: RAIL_SUB.31736
Node: 2965
Step: Step-4-2 Frame: 28
Max: +1.044e-001
N 4431
131 mm
Y
Z
X
DB rig C,frict.0.2,vert.load 15t,angle of attack 0.25 deg,R-plastic,W-elastic
ODB: DB_C_4.odb Abaqus/Standard Version 6.8-2 Wed May 20 10:48:47 W. Europe Standard Time 2009
Step: Step-4-2, Wheel movement
Increment 28: Step Time = 0.7405
Primary Var: PEEQ
Deformed Var: U Deformation Scale Factor: +1.000e+00

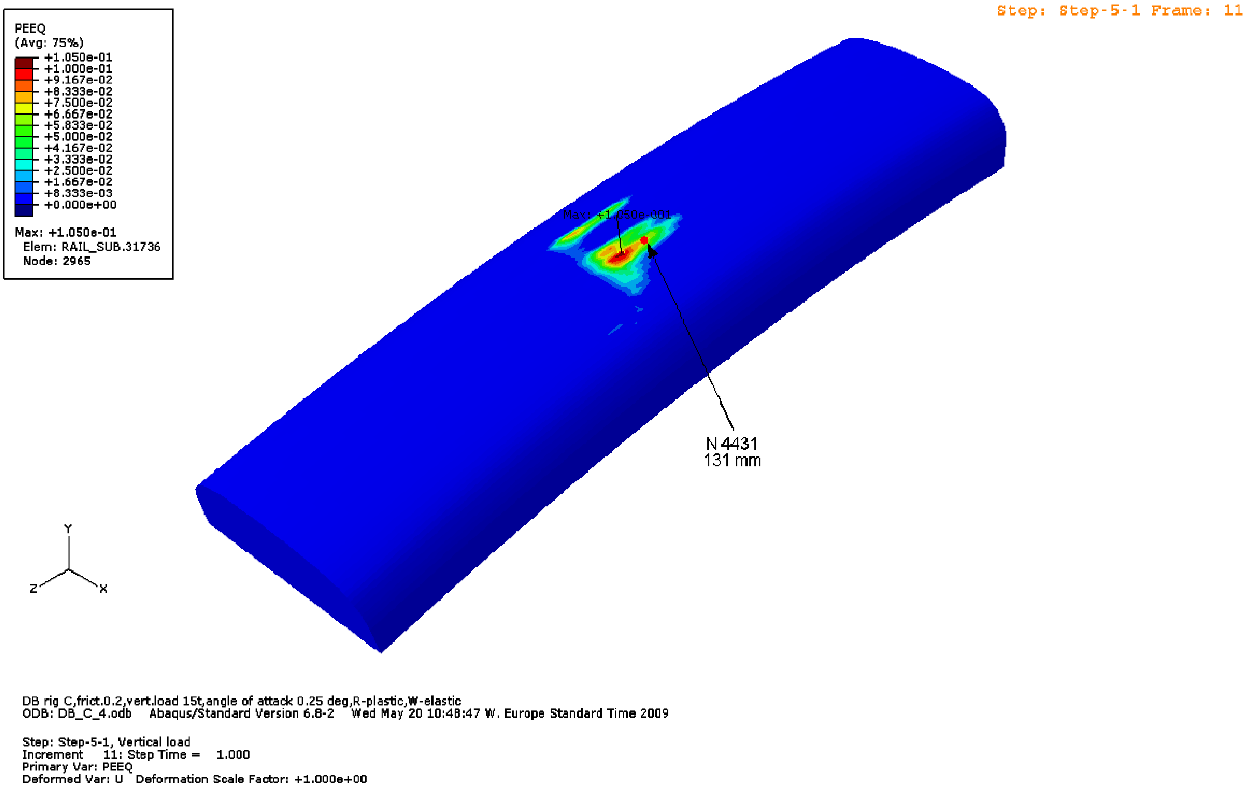
Step: Step-5-1 Frame: 11
PEEQ
(Avg: 75%)
+1.050e-01
+1.000e-01
+9.167e-02
+8.333e-02
+7.500e-02
+6.667e-02
+5.833e-02
+5.000e-02
+4.167e-02
+3.333e-02
+2.500e-02
+1.667e-02
+8.333e-03
+0.000e+00
Max: +1.050e-01
Elem: RAIL_SUB.31736
Node: 2965
Max: +1.050e-01
N 4431
131 mm
Y
Z
X

DB rig C,frict.0.2,vert.load 15t,angle of attack 0.25 deg,R-plastic,W-elastic
ODB: DB_C_4.odb    Abaqus/Standard Version 6.8-2    Wed May 20 10:48:47 W. Europe Standard Time 2009

Step: Step-5-1, Vertical load
Increment    11: Step Time =    1.000
Primary Var: PEEQ
Deformed Var: U   Deformation Scale Factor: +1.000e+00

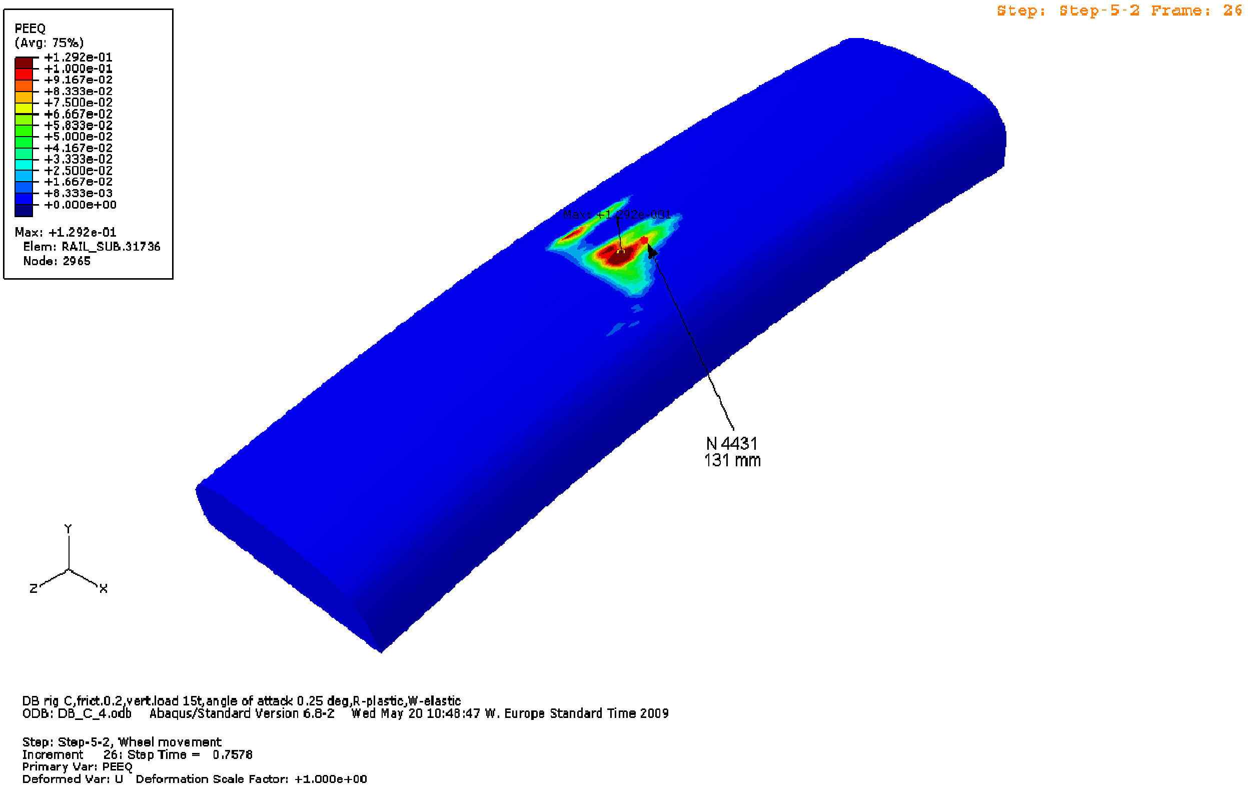
Step: Step-5-2 Frame: 26
PEEQ
(Avg: 75%)
+1.292e-01
+1.000e-01
+9.167e-02
+8.333e-02
+7.500e-02
+6.667e-02
+5.833e-02
+5.000e-02
+4.167e-02
+3.333e-02
+2.500e-02
+1.667e-02
+8.333e-03
+0.000e+00
Max: +1.292e-01
Elem: RAIL_SUB.31736
Node: 2965
Max: +1.292e-01
N 4431
131 mm
Y
Z
X

DB rig C,frict.0.2,vert.load 15t,angle of attack 0.25 deg,R-plastic,W-elastic
ODB: DB_C_4.odb    Abaqus/Standard Version 6.8-2    Wed May 20 10:48:47 W. Europe Standard Time 2009

Step: Step-5-2, Wheel movement
Increment    26: Step Time =    0.7576
Primary Var: PEEQ
Deformed Var: U   Deformation Scale Factor: +1.000e+00